

Stability of underground openings in stratified and jointed rock

Thesis submitted in partial fulfillment of the requirements for the degree of "DOCTOR OF PHILOSOPHY"

by

Michael Tsesarsky

Submitted to the Senate of Ben Gurion University of the Negev

September 05

Kislev, 5765

BEER-SHEVA

This work was carried out under the supervision of

Dr. Yossef Hodara Hatzor

in the Department of Geological and Environmental Sciences

Faculty of Natural Sciences

Stability of underground openings in stratified and jointed rock

By

Michael Tsesarsky

Department of Geological and Environmental Sciences

Ben Gurion University of the Negev

Abstract

The stability of underground openings excavated in stratified and jointed rock was studied using the Discontinuous Deformation Analysis method (Shi, 1988; 1993). The goals of this research were: 1) validation of DDA using analytical solutions, physical models and case study; 2) investigation of fractured beam kinematics; and 3) development of simplified design charts for assessment of rock overbrake above excavations as a function of joint spacing and shear resistance along joints.

Validation of DDA using a shaking table model of a block on an incline (Wartman et al., 2003) showed that DDA accurately predicts the displacement history of the block, provided that the numeric control parameters are optimized correctly. It was found that for slopes subjected to dynamic loading a certain amount of “kinetic” damping is necessary: a 2% reduction of the inter time-step transferred velocity yielded the best accuracy and the most realistic time behavior of the modeled system.

Comparison of DDA results with centrifuge model tests of a multi-jointed rock beam showed that DDA essentially captures the arching stresses developing in a deforming rock beam. Discrepancies between DDA and measured displacements are attributed to the difference between the joint model in DDA and the actual block interfaces used in the centrifuge model.

A study of an ancient roof failure in an underground opening excavated in a densely jointed rock mass, showed that DDA is more realistic than the classic Voussoir beam model (Beer and Meek, 1982), which was found to be un-conservative. This research further augmented the preliminary findings by Hatzor and Benary (1998).

Investigation of fractured beam kinematics shows that transition from shear along abutments to stable arching is a function of the available shear resistance along joints. Given sufficient shear resistance the peripheral blocks undergo effective rotation, thus inducing stable arching. Otherwise, shear along abutments precludes effective rotation, and the beam is found to sag under its own weight. Within a stack of fractured rock beams the transition from ongoing deformation to stable arching is marked by the homogenization of the vertical displacements profile. The transition from unstable conditions to stable arching is found to be a function of both transverse joint spacing and shear resistance along joints.

The general behavior of underground openings excavated in stratified and vertically jointed rock masses was studied using two different tunnel geometries: 1) excavation span $B = 10m$; and 2) excavation span $B = 15m$. The modeled tunnel height was $h_t = 10m$ for both configurations. Fifty individual simulations were performed for different values of transverse joint spacing and shear resistance along joints. It was found that the height of the loosening zone (or overbrake) above an underground excavation is determined by the ratio between joint spacing and the excavation span (S_j/B): 1) for $S_j/B \leq 0.2$ the height of the loosening zone is

found to be smaller than $0.5B$; 2) for $S_j/B \geq 0.3$ the rock mass above the excavation attains stable arching.

Terzaghi's (1946) rock load classification for a blocky rock mass predicts that the rock load above the excavation should range from $0.25B$ to $1.1(B+h_i)$, pending on the degree of jointing. However, the degree of jointing is not quantified, and guidelines for assessing the degree of jointing are not provided. When compared with the findings of this research Terzaghi's predictions are found to be rather conservative.

The contribution of this study lies in the explicit correlation between the geometrical features of the rock mass, which are routinely collected during exploration and excavation, and the extent of the instability zone above the excavation. This is expected to contribute to a more efficient and economic design, and to increase the safety of underground openings in stratified and jointed rocks.

This Work is Dedicated to My Beloved Wife Galia

Table of Contents

Table of Contents	i
List of Figures.....	iv
List of Tables.....	viii
Acknowledgments	ix
Nomenclature	xi
Chapter 1 - Introduction	1
1.1 Overview	1
1.2.Objectives	2
1.3. Thesis Organization.....	2
Chapter 2 - Stability Analysis of Underground Openings in a Stratified and Jointed Rock Mass	4
2.1. Introduction	4
2.2. Observational Methods.....	6
2.3. Semi-analytical Approach – the Voussoir Beam Analogy.....	10
2.4. Numerical Approach	13
2.4.1. <i>The Finite Element Method</i>	13
2.4.2. <i>The Discrete Element Method (DEM)</i>	14
2.5. Numerical Modeling of the Voussoir Beam Using FEM and DEM	15
2.6. Physical Modeling of the Voussoir Beam	16
2.7. Case Studies.....	18
2.8. Current Research Motivation	19
Chapter 3 – DDA Basics: Review of Fundamentals	20
3.1. Formulation of Simultaneous Equilibrium Equations	20
3.2. Energy Functionals and Contributions to Global Equilibrium Equations	23
3.3. Block System Kinematics and Contacts	27
3.3.1. <i>Distance between two blocks</i>	28
3.3.2. <i>Contacts and interpenetration</i>	29
3.3.3. <i>Energy functional of a stiff contact</i>	30

3.3.4. <i>Limitations of DDA stiff contact formulation</i>	33
3.4. Time Integration Scheme	34
3.5. DDA Numeric Implementation.....	37
Chapter 4 – Validation of DDA Using Analytical Solutions and Shaking Table Experiments	40
4.1. Introduction.....	40
4.2. Validation of DDA Using an Analytical Solution	41
4.3. Validation of DDA by Shaking Table Experiments	47
4.3.1 <i>Experimental setting</i>	47
4.4. DDA Prediction vs. Shaking Table Results	53
4.4.1. <i>Accuracy of DDA</i>	54
4.5. Conclusions.....	59
Chapter 5 – Validation of DDA Using a Centrifuge Model of a Jointed Rock Beam	60
5.1. Introduction.....	60
5.2. Experimental Setting.....	61
5.2.1. <i>Jointed beam model</i>	61
5.3. <i>DDA Model</i>	62
5.3.1 <i>A simple two-block system</i>	62
5.3.2. <i>A six block model</i>	66
5.3.3. <i>Selection of numerical control parameters</i>	66
5.3.4. <i>Results</i>	72
5.4. Discussion and Conclusions	76
Chapter 6 – The Tel Beer-Sheva Case Study	76
6.1. Introduction.....	76
6.2. Site Description.....	77
6.2.1. <i>Geology</i>	78
6.2.2. <i>Geometrical properties of discontinuities and failure zone morphology</i>	78
6.3. Mechanical Properties of Intact Rock.....	81
6.3.1. <i>Experimental procedure</i>	81
6.3.2. <i>Test results</i>	84
6.3.3. <i>Estimation of the in-situ stresses</i>	84
6.4. Mechanical Properties of Discontinuities	88

6.4.1. Direct Shear testing apparatus and sample preparation.....	88
6.4.2. Direct shear tests of natural joint	89
6.4.3. Shear rate effect – polished interface	89
6.4.4. Direct shear tests of a polished interface	90
6.5. Stability Analysis Using Classical Voussoir Model	97
6.6. Numerical Analysis Using DDA	101
6.6.1. Numerical problems associated with multi-block systems	101
6.6.2. DDA analysis of the Tel Beer-Sheva water reservoir – numerical setup.....	104
6.6.3. DDA analysis of the single layer configuration.....	107
6.6.4. DDA analysis of sequence of layers - laminated Voussoir beam	112
6.6.5. Limitations of DDA.....	113
6.6.6. Comparison between DDA and classic Voussoir solutions.....	119
Chapter 7 - Stability Analysis of Underground Openings in Horizontally Stratified and Vertically Jointed Rock	120
7.1. Introduction.....	120
7.1.1. Model geometry and mechanical properties	121
7.1.2. Selection of contact stiffness.....	125
7.1.3. Criteria for stable arching.....	127
7.2. Results.....	128
7.2.1. Roof span of 10m	128
7.2.2. Influence of joint randomness.....	130
7.2.3. Roof span of 15m	137
7.2.4. Rock mass response as a function of excavation span.....	142
7.3. Discussion.....	146
Chapter 8 – Conclusions	151
8.1. DDA Limitations	152
8.2. DDA Accuracy.....	153
8.3. DDA Validation	153
8.4. Stability of Underground Openings in Horizontally Stratified and Vertically Jointed Rock	156
8.5. Recommendations for Future Research.....	158
Appendix	160
References	164

List of Figures

Figure 2.1. a) Horizontally laminated rock mass and immediate roof deflection; b) Horizontally laminated rock mass with vertical joints (after Brown and Brady, 1993).....	5
Figure 2.2. Maximum expected over-brake for unsupported tunnels: a) horizontally stratified rock (top); b) vertically stratified rock (bottom). From Terzaghi (1946).....	8
Figure 2.3. Evans's Voussoir beam: a) conceptual model; b) compressive stress distribution in the beam.	12
Figure 3.1. Distance of two blocks (after Shi, 1993)	28
Figure 3.2. Types of blocks contact: a) angle to edge; b) angle to angle; c) edge to edge (after Shi, 1993).	29
Figure 3.3 Contact conditions: a) overlapping angle and edge; b) overlapping angles (modified after Shi, 1993).....	30
Figure 3.4. A wedge loaded by normal and tangential forces at the apex (after Timoshenko and Goodier, 1951)	33
Figure 3.5. Two block system.	36
Figure 3.6. DDA results for the two block system: for a time step size of $g_1 = 0.005$ sec a) vertical stress at the centroid of the upper block for different values of contact stiffness; b) relative numeric error for different values of contact stiffness.	38
Figure 3.7. DDA results for the two block system for contact stiffness of $g_0 = 50 \cdot 10^6$ N/m: a) vertical stress at the centroid of the upper block for different values of time step size (g_1) ; b) relative numeric error for different values of time step size (g_1).....	39
Figure 4.1. a) the loading function $a(t) = a_1 \sin(\omega_1 t) + a_2 \sin(\omega_2 t) + a_3 \sin(\omega_3 t)$; b) comparison between analytical and DDA solution for block displacement subjected to a loading function consisting of a sum of three sines.	44
45 Figure 4.2. Sensitivity analysis of the DDA numeric control parameters.	
Figure 4.3. Sinusoidal input motion for the shaking table experiment: 2.66 Hz frequency (Test 1 at Table 4.2).	49
Figure 4.4. a) general view of the inclined plane and the sliding block (top); b) sliding block experimental setup and instrumentation location (bottom), from Wartman (1999).	50
Figure 4.5. Back analyzed friction angles shown as a function of average sliding velocity for rigid block tests, from Wartman (2003).	51
Figure 4.6. The 2.66 Hz sinusoidal input motion test: a) displacement derived velocity; b) velocity content.	52

Figure 4.7. The 2.66 Hz input motion: comparison between measured displacement and DDA solutions for different values of inter time step velocity reduction ($k01$).	57
Figure 4.8. The 2.66 Hz input motion: relative numeric error of DDA ultimate displacement as a function of inter time step velocity reduction ($k01$).	57
Figure 4.9. Numeric difference of DDA ultimate displacement prediction as a function of input motion frequency.	58
Figure 4.10. The 2.66 Hz input motion: evolution over time of the DDA relative numeric error, for different values of the $k01$ parameter.	58
Figure 5.1 Centrifuge model geometry and instrumentation (courtesy of M. Talesnick).....	63
Figure 5.2 DDA model geometry.	63
Figure 5.3. DDA model of two block system with fixed base vertices: a) mid-span deflection (\square) as a function of time; b) number of time steps n required to attain equilibrium as a function of the dynamic control parameter ($k01$).	64
Figure 5.4. Contact stiffness sensitivity analysis for the DDA six block model: a) vertical displacements; b) horizontal stresses within the blocks.	69
Figure 5.4 b) Contact stiffness sensitivity analysis for the DDA six block model: c) time histories.	70
Figure 5.5. Iteration history for the DDA six block model for different values of contact stiffness.	71
Figure 5.6. DDA six block model loading function.	73
Figure 5.7. Comparison between centrifuge model results and DDA solution: a) vertical displacements; b) horizontal stresses.	74
Figure 5.8. DDA six block model: angle to principal stresses (θ) within the blocks	75
Figure 6.1. Schematic drawing of the Tel Beer-Sheva archeological site and the water reservoir. (Source: Hatzor and Benari, 1998).	79
Figure 6.2 General layout and failure zone mapping of the water reservoir, after Benary (1996).....	82
Figure 6.3. Cross-sections of the water reservoir.....	83
Figure 6.4 Complete stress-strain curves for the Gareb chalk at uniaxial compression parallel and normal to bedding	86
Figure 6.5. a) Calculated and measured stress ratio k at the Beer-Sheva syncline; b) horizontal and vertical stresses at the Beer-Sheva syncline.	87
Figure 6.6. Direct shear system at the Rock Mechanics Laboratory of the Negev: a) general view; b) assembled shear box and displacement detectors (LVDT's).....	92

Figure 6.7. Direct shear results of a natural joint in Gareb formation, sample TBS-1.	93
Figure 6.8. Direct shear results for polished surface in Gareb chalk, sample TBS – 2.....	94
Figure 6.9. Direct shear results for a polished surface, sample TBS-4.....	95
Figure 6.10. Sample TBS-4: normal displacement vs. shear displacement at different levels of normal stress.....	96
Figure 6.11. Classic Voussoir beam analysis of the Tel Beer-Sheva water reservoir.....	99
Figure 6.13. DDA multi block model: average number of iterations per time step as a function of penalty stiffness (g_0) for different values of time step size (g_1) and penetration control parameter (g_2).	103
Figure 6.14. Geometry of DDA model of the Tel Beer-Sheva water reservoir: a) single layer model; b) multi-layered model.	106
Figure 6.15. DDA prediction for mid-span deflection of the single layer model.....	109
Figure 6.16. Deformation profiles of the DDA single layer model, measured at the lowermost fiber of the beam/	110
Figure 6.17. DDA graphic output of single layer deformation for different values of joint friction angle.....	111
Figure 6.18. a) DDA prediction for mid-span deflection of the multi-layered model.	116
Figure 6.19. DDA graphic output of the multi-layer deformation for different values of joint friction angle.....	117
Figure 7.1. Geometry of the DDA model.....	124
Figure 7.2. Two types of rock masses.....	124
Figure 7.3. Contact stiffness sensitivity analysis for a DDA model of tunnel span $B = 10\text{m}$ and vertical joints spacing $S_j = 1.5$	126
Figure 7.4. DDA graphic output for tunnel span of $B = 10\text{m}$ and vertical joint spacing of $S_j = 1.5$: a) initial configuration (top); b) deformed configuration (bottom).	131
Figure 7.5. Vertical displacement (δ) profile above an underground opening of span $B = 10\text{m}$, for different values of joint spacing (S_j) and friction along joints (ϕ).	132
Figure 7.6. Vertical displacement difference ($\Delta\delta/\Delta y$) profile above an underground opening of span $B = 10\text{m}$, for different values of joint spacing (S_j) and friction along joints (ϕ).	133
Figure 7.7. Rock mass response above an underground opening of span $B = 10\text{m}$, and joint spacing of $S_j = 1.5\text{m}$	135
Figure 7.8. DDA graphic output for tunnel span of $B = 10\text{m}$, vertical joint spacing of S_j	

= 1.5m with random	136
Figure 7.9. Vertical displacement (δ) profile above an underground opening of span $B = 15\text{m}$, for different values of joint spacing (S_j) and friction along joints (ϕ).....	138
Figure 7.10. Vertical displacement difference ($\Delta\delta/\Delta y$) profile above an underground opening of span $B = 15\text{m}$, for different values of joint spacing (S_j) and friction along joints (ϕ).....	139
Figure 7.11. DDA graphic output for tunnel of span $B = 15\text{m}$, vertical joint spacing of $S_j = 2\text{m}$ and friction angle of $\phi = 20^\circ$	140
Figure 7.12. DDA graphic output for tunnel of span $B = 10\text{m}$, vertical joint spacing $S_j = 2$ and friction angle of $\phi = 20^\circ$ m.	141
Figure 7.13. Normalized displacement δ/B for normalized joint spacing of $S_j/B = 0.2$	143
Figure 7.14. Vertical displacement ratio $\delta_{B=15}/\delta_{B=10}$ for different values of normalized joint spacing S_j/B	144

List of Tables

Table 4.1. Frequency sets for a loading function consisting of a sum of three sines.....	43
Table 4.2. Shaking table model summary.....	49
Table 5.1. Material properties and numeric control parameters for the DDA six block model.....	73
Table 6.1. Principal joint sets in the Gareb chalk at Tel Beer-Sheva site, from Benary (1996).....	79
Table 6.2. Mechanical properties of the Gareb chalk at Tel Beer-Sheva.....	86
Table 6.3. Shear stiffness at different shear rate values for sample TBS – 2.....	94
Table 6.4. Representative material I properties of the Gareb Chalk.....	97
Table 6.5. Material properties and numeric control parameters for the DDA model of the Tel Beer-Sheva water reservoir.....	105
Table 7.1. DDA modeling matrix.....	122
Table 7.2 Locations of measurement points in DDA model. X, Y coordinates are with respect to the center of the geometrical domain.....	123
Table 7.3. Material properties and numeric control parameters for DDA model.....	123
Table 7.4. Normalized height of loosening zone ($h_r = h/h_t$) above an underground opening for a horseshoe tunnel of width $B = 10m$ and height $h_t = 10m$	130
Table 7.5. Normalized height of loosening zone ($h_r = h/h_t$) above an underground opening, for a horseshoe tunnel of width $B = 15m$ and height $h_t = 10m$	145
Table 7.6. Normalized height of the loosening zone ($h_r = h/h_t$) above an underground opening for different values of joint spacing and opening span (S_j/B).....	147

Acknowledgments

I was privileged to conduct this research under the guidance of Dr. Yossef Hodara Hatzor. His wisdom and philosophy greatly enhanced my professional and personal development. For all that and much more I am greatly indebted.

I would like to thank Dr. Gen-hua Shi the father of DDA, and many other wonderful ideas, for the privilege to work with DDA. His short visits to Israel were always enlightening and instructive.

Dr. Mark Talesnick from the Technion has devised and executed the centrifuge tests of the fractured rock beams. His engineering ingenuity, experimental creativity, and cooperation are greatly acknowledged.

I thank Prof. Nicholas Sitar from the University of California, Berkeley for his assistance during the initial stages of this research. Professor Joseph Wartman of Drexel University, and Professors Jonathan Bray and Raymond Seed from University of California, Berkeley are thanked for providing the test data for the shaking table model. Dr. David Doolin is thanked for his valuable suggestions and productive dialog on DDA essentials.

Dr. V. Palchick from the Rock Mechanics Laboratory of the Negev, BGU is thanked for his assistance with rock testing.

This work was partially supported by the Israel-USA Bi-National Science Foundation (BSF) through grant number 98-339. The BSF support is kindly acknowledged.

I would like to thank Prof. Yehuda Eyal from the Department of Geological and Environmental Sciences, BGU for his support and encouragement during all my years as graduate student.

Prof. S. Freedman from the Faculty of Civil Engineering, Technion and Prof. M. Perl from the Department of Mechanical Engineering, BGU served on my Ph.D. candidacy

committee. They are thanked for putting me on the right track. It wasn't easy, but definitely worthy.

It has been a great pleasure to study and work in the Department of Geological and Environmental Sciences, BGU. I have learned much from the faculty of the Department of Geological and Environmental Sciences and would like to thank in particular Prof. M. Eyal and Prof. H. J. Kisch.

I thank the administrative staff of our department, firmly headed by Mrs. Rivka Eini. She was always there to smoothen up bureaucracy, and to help with everything within (and beyond) her mandate. The technical staff of the department is thanked for all the support provided during the years. Special thanks are extended to Mr. D. Kozashvily.

I would like to thank my fellow graduate students for the years we spent together. Special thanks are extended to Shai Arnon, Shai Ezra, Sigal Abramovich, Efi Farber, Anat Bernstein, Zafrir Levy, Ilanit Tapiero, and Boaz Saltzman.

My friends: Erez and Galit Tzfadia, Sagee and Dorit Levy, Sami and Orly Ohana, Shai and Iris Ezra, Tal and Simon Tamir, who were there to support and encourage, your friendship is beyond words.

I would like to express my deepest gratitude to my parents who planted the seed of curiosity and inquisitiveness. I am also grateful to all other members of my family: my elder brother Ilia his wife and children.

Last but dearest my wife Galia. The last five years were hard. I could not make it trough without your love, friendship, care, endurance and patience. This work is dedicated to you.

Nomenclature

<i>Symbol</i>	<i>Description</i>	<i>Chapter</i>
W	weight of Voussoir beam	Appendix
S	span of Voussoir beam	
T	axial thrust	
Z	lever arm of the axial couple	
t	Voussoir beam thickness	
n	thickness of compressive arch	
γ	unit weight	
f_c	maximum compressive stress	
L	length of the reaction arch	
f_{av}	average stress along the compression arch	
UCS	uniaxial compressive strength	
ϕ	friction angle	
(u, v)	displacement of a point	3.1
(x, y)	coordinates of a point	
ε_x	x-direction strain	
ε_y	y-direction strain	
γ_{xy}	shear strain	
(x_0, y_0)	center of gravity	
(u_0, v_0)	block translation	
(r_0)	block rotation angle	
$[D_i]$	unknowns of block i	
$[T_i]$	displacement matrix of block i	
K_{ij}	submatrix of equilibrium equations	
$[K]$	global stiffness matrix	
F_i	loads on block i	
$\{F\}$	load vector	
Π	total potential energy	
Π_e	strain energy of block	
σ_x	x-direction stress	3.2
σ_y	y-direction stress	
τ_{xy}	shear stress	
E	Elasticity modulus	
S	area of block i	
Π_p	potential energy of point load	
f_x, f_y	x, y directions of point load	
Π_l	potential energy of line load	

<i>Symbol</i>	<i>Description</i>	<i>Chapter</i>
$F_x(t), F_y(t)$	parametric equations for x, y directions of line load	
l	length of segment	
Π_w	potential energy of volume load	
Π_i	potential energy of inertia force	
M	mass per unit area	
η_{ij}	distance between two blocks	3.3
Π_c	potential energy constraint spring	
p	stiffness of constraint spring	
u	displacement of a point	3.4
\dot{u}	velocity of a point	
\ddot{u}	acceleration of a point	
Δt	integration time step	
β, γ	integration collocation parameters	
e_n	relative numeric error	
a	acceleration	4
ω	frequency	
g	Earth gravitational acceleration	
ρ	material density	5
h	depth	
N	scaling factor	
i	total number of iterations	6
i_{av}	average number of iteration per time step	
k	horizontal to vertical stress ratio	
δ	mid span deflection	
S_j	average joint spacing	
L_j	average joint length	7
B_j	average joint bridge	
D_r	degree of randomness	
B	tunnel span	
h_t	tunnel height	
h_r	loosening zone height	

Chapter 1 - Introduction

1.1. Overview

Most rock masses are discontinuous over a wide range of scales, from macroscopic to microscopic. In sedimentary rocks the two major sources of discontinuities are: 1) bedding planes, and 2) joints. Bedding planes are formed due to sedimentary processes, while joints are formed by lithification processes or by tectonic forces. The intersection of bedding planes and joints forms the so-called “blocky” rock mass.

Before the excavation of an underground opening the blocky rock mass is assumed to be in a state of static equilibrium and in optimum packing arrangement. Excavation of an opening disturbs the initial equilibrium, and the stresses in the rock mass tend to readjust until new equilibrium is attained. During the readjustment of the internal stresses, and hence the rearrangement of load resisting forces, some displacements of the rock blocks occurs. Failure occurs when the stresses can no longer readjust to form a stable, load resisting structure. This may occur either when the material strength is exceeded at some locations or when movements of the rock blocks preclude stable geometric configuration, without strength failure.

Joints and beddings are sources of weakness in an otherwise competent rock mass, therefore large displacements and rotations are only possible across these discontinuities. The displacements and rotations of the rock block along and across the joints is the source of the volume change. The interaction forces between blocks result in: 1) an increase in formation

stresses, due to volume expansion in restricted volume, tending to create stable conditions; and 2) application of forces that can cause an increased displacement, tending to induce rock mass failure. The interaction between the stabilizing and destabilizing factors shape the overall behavior of the blocky rock mass.

1.2. Objectives

The research presented in this dissertation focuses on the kinematical behavior of underground openings in layered and jointed rock masses. The primary objectives of this research are: 1) validation of the numeric Discontinuous Deformation Analysis (DDA) model using physical models and case studies; 2) investigation of fractured beam kinematics; 3) development of simplified design charts and tables for assessment of rock loads in underground openings as a function of joint spacing and joint friction angle.

1.3. Thesis Organization

Chapter 2 is a brief overview of the techniques commonly used in engineering practice for estimating the stability of underground openings in blocky rock masses. The different approaches are described and discussed, and the limitations are addressed.

Chapters 3 describes the theoretical background of the Discontinuous Deformation Analysis (DDA) method and previous validation effort. Following is the validation of DDA using a shaking table physical model (Wartman et al, 2003) presented in Chapter 4. The results of the validation study are discussed and recommendations of numeric improvements are presented. Chapter 5 describes DDA validation using centrifuge model tests of a jointed beam, which were performed by M. Talesnick at the Technion.

Chapter 6 describes DDA validation using the case study of the ancient water reservoir at the Tel Beer-Sheva archeological site, which was studied initially by Hatzor and Benary (1998). The system was excavated in highly layered and jointed rock mass. The re-visited case study is here described in detail, including physical testing of intact rock and the discontinuities. The results are discussed, and general conclusions regarding behavior of blocky rock masses are presented.

Chapter 7 presents an investigation of the general behavior of layered and jointed roofs. Simplified design charts based on geometrical properties of the discontinuities are presented and discussed. Finally, Chapter 8 summarizes the key findings of this research and makes suggestions regarding future research.

Chapter 2 - Stability Analysis of Underground Openings in a Stratified and Jointed Rock Mass

2.1. Introduction

A stratified host rock mass is a common feature in mining and civil engineering where excavation in sedimentary rock is attempted. Stratified rock (Fig. 2.1a) is defined as composed of a succession of parallel layers whose thickness is small compared with the span of the opening (Obert and Duvall, 1976). There are two principal mechanical properties of bedding planes that are significant in the context of underground projects : 1) low to zero tensile strength; 2) low shear strength. If an opening is excavated in this type of rock the roof of the excavation will part from the rock mass due to low tensile strength of bedding planes, thus forming the immediate roof. Investigation of immediate roof stability commenced more than a century ago when Fayol (1885) conducted experiments on a stack of wood beams spanning a simple support, simulating the bedded sequence of roof span. By noting the deflection of the lowest beam as successive beams were loaded onto the stack, Fayol demonstrated that at a certain stage none of the added load of an upper beam was carried by the lowest member. The load of the upper beams was transmitted laterally to the supports, rather than vertically as transverse loads to the lower members. For such a configuration beam theory can be employed to assess deflection, shear stresses, and maximum stresses in the immediate roof as a function of elastic parameters, rock density, and beam geometry (Obert

and Duvall, 1976). Goodman (1989) incorporated inter-bedding friction into the beam analysis, thus extending the capabilities of this method. These analyses however are limited to continuous, clamped beams only.

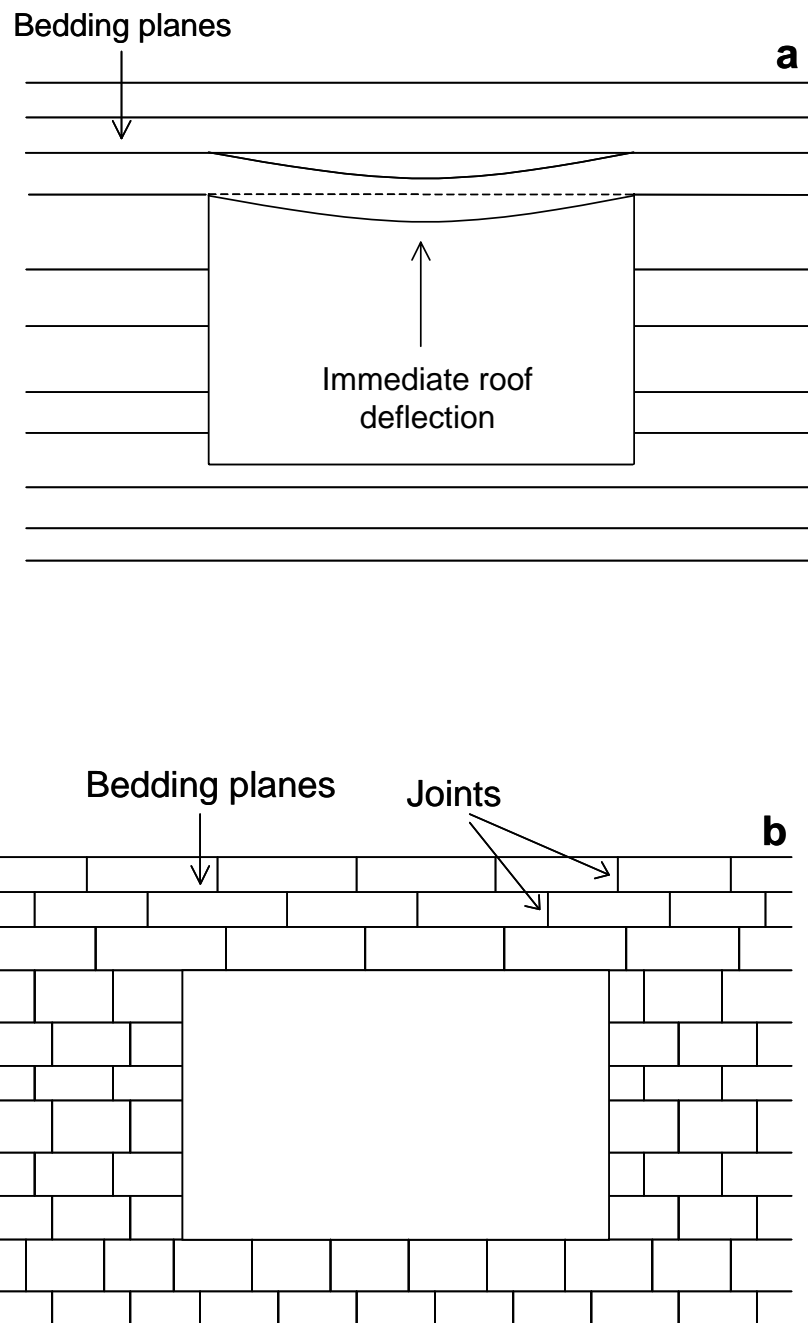


Figure 2.1. a) Horizontally laminated rock mass and immediate roof deflection; b) Horizontally laminated rock mass with vertical joints (after Brown and Brady, 1993)

In practice, stratified rock masses are in most cases transected by numerous joints forming a matrix of individual rock blocks. Horizontal stratification with vertical jointing one common case (Fig. 2.1b). The analysis of a stratified and jointed roof is complicated by the fact that there is no closed-form analytical solution for the interaction of these blocks. In absence of a closed-form solution, the practicing engineer/geologist should rely on other methods for assessing the stability of the roof. Three different methods are currently in practice: 1) observational methods; 2) semi-analytical methods; 3) numerical methods. These methods are widely used today, either stand alone or in an integrated manner, in all areas of geological and civil engineering.

2.2. Observational Methods

Standard engineering design both in continuous and structurally discontinuous rock is largely based on observational methods known as rock mass classification methods, mostly assessing the expected stand-up time and the required support loads.

Terzaghi (1946) formulated the first rational method of classification by evaluating the rock loads appropriate to the design of steel sets, based on rock mass description. Terzaghi's descriptions are:

- Intact rock contains neither joints nor hair cracks. Hence, if it breaks, it breaks across sound rock. On account of the injury to the rock due to blasting, spalls may drop off the roof several hours or days after blasting. Hard, intact rock may also be encountered in the popping condition involving the spontaneous and violent detachment of rock slabs from the sides or roof.
- Stratified rock consists of individual strata with little or no resistance against separation along the boundaries between the strata. The strata may or may not

be weakened by transverse joints. In such rock the spalling condition is quite common.

- Moderately jointed rock contains joints and hair cracks, but the blocks between joints are locally grown together or so intimately interlocked that vertical walls do not require lateral support. In rocks of this type, both spalling and popping conditions may be encountered.
- Blocky and seamy rock consists of chemically intact or almost intact rock fragments, which are entirely separated from each other and imperfectly interlocked. In such rock, vertical walls may require lateral support.
- Crushed but chemically intact rock has the character of crusher run. If most or all of the fragments are as small as fine sand grains and no recementation has taken place, crushed rock below the water table exhibits the properties of a water-bearing sand.
- Squeezing rock slowly advances into the tunnel without perceptible volume increase.
- Swelling rock advances into the tunnel chiefly on account of expansion.

According to Terzaghi's classification for tunnels excavated in stratified rock the maximum expected overbreak, if no support is installed, is ranging from $0.25B$ to $0.5B$, where B is the tunnel span. The lower estimate is assigned to vertically stratified rock (Fig. 2.2b) while the higher is assigned to horizontally stratified rock (Fig 2.2a). For tunnels excavated in moderately massive jointed rock the maximum expected over break is $0.25B$. For tunnels excavated in blocky rock mass the expected over break ranges from $0.25B$ to $1.1(B+H_t)$, where H_t is the height of tunnel, pending on the degree of jointing. This estimate is valid for tunnels at depth of up to $1.5(B+H_t)$, for deeper tunnels the expected over break is constant at $1.15(B+H_t)$.

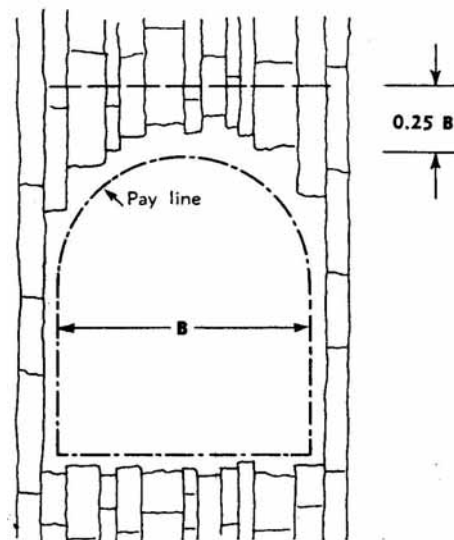
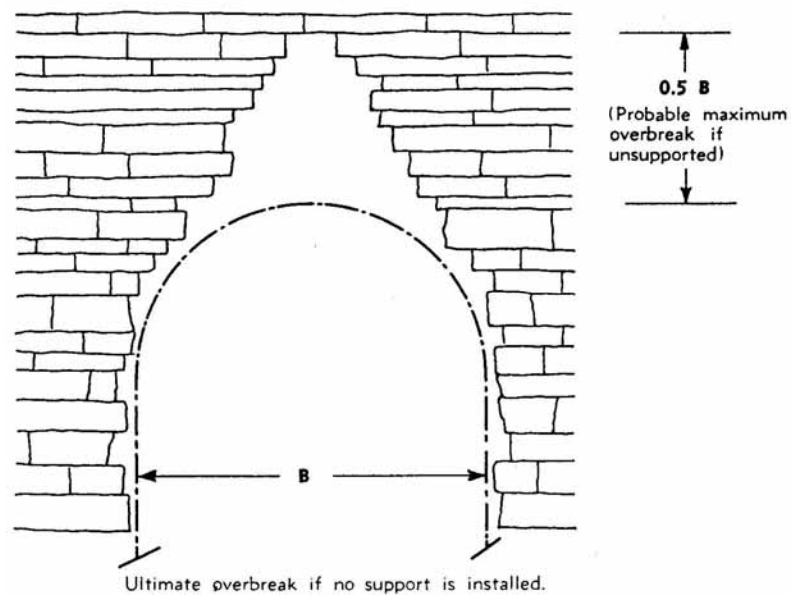


Figure 2.2. Maximum expected overbrake for unsupported tunnels: a) horizontally stratified rock (top); b) vertically stratified rock (bottom). From Terzaghi (1946).

The definitions of the different rock classes in Terzaghi's method are ambiguous, and no particular reference to the mechanical and geometrical properties of the discontinuities is given.

Lauffer (1958) introduced the concept of *Stand-Up Time*, which estimates the time to failure for any active unsupported span as a function of rock structure. Lauffer's original classification has since been modified by a number of authors, notably Pacher et al (1974), and now forms part of the general tunneling approach known as the New Austrian Tunneling Method (NATM).

Development of new support techniques, i.e. the use of rock bolts and shotcrete, gave rise to new *Rock Mass Classification Methods* encompassing all aspects of support design: from stand-up time to support requirements. Two of the most prominent methods are the *Geomechanics Classification* (a.k.a. Rock Mass Rating -RMR) of Bieniawski (1973) and the *Rock Quality* system of Barton et al., (1974) both based on extensive database of case studies. In each method the critical parameters of the rock mass are described and rated, and simple equations yield the overall rock mass rating. Based on the rock mass rating a support design is suggested, as well as the unsupported stand-up time. These observational methods are widely used today by practitioners world wide, mostly as checkup on their design.

Two major drawbacks of the rock mass classification methods are to be noted: 1) rock mass classifications are a very general and a rather coarse approach in that it caters for all possible rock masses and type of excavation; 2) absence of mechanistic basis. Recent studies in Israel (Polishook and Flexer, 1998; Tsesarsky and Hatzor, 2000) show that these methods are in some cases over conservative, even when a simple rock mass is encountered (homogenous massive rock with widely spaced joints). Riedmuller and Schubert (1999), based on extensive tunneling practice in the Austrian Alps, show that rock mass classification is inadequate for support design and stability evaluation in complex geological conditions.

The absence of true understanding of deformation mechanisms and the over conservative nature of the empirical methods will eventually lead to over conservative support design and unnecessary inflated project costs (Riedmuller and Schubert, 1999).

2.3. Semi-analytical Approach – the Voussoir Beam Analogy

As noted by Fayol (1885) underground strata tend to separate upon deflection such that each laminated beam transfers its own weight to the abutments rather than loading the beam beneath. Stability of the excavation in this situation can be determined by analyzing the stability of a single beam deflecting under its own weight. Bucky (1931) and Bucky and Taborelli (1938) studied physical models for the creation and extension of wide roof spans. They used initially intact beams of rock like materials, and found that at a particular span, a vertical tension fracture was induced at the mid-span of the lower beam. These observations, and the fact that roof strata are crossed by joints, lead to the conclusion that the roof at incipient failure cannot be treated as a simple beam.

Evans (1941) in his fundamental work established the relationship between vertical deflection, lateral thrust and stability of natural or artificially jointed roof. This work coined the term “Voussoir Beam” spanning an excavation, using the analogy of the masonry Voussoir arch (Heyman, 1982). The basic Voussoir concept accepts that the beam may not carry longitudinal tensile stresses and it is confined between the abutments, i.e. lateral constrains are applied. The geometry and the forces acting in the Voussoir beam are shown in Figure 2.3a. The overturning gravitational-reaction couple is equilibrated by the lateral thrust couple formed by beam deflection, where W is the weight of the beam, S is the beam span, T is the axial thrust and Z is the lever arm.

The structure presented in Figure 2.3a is statically indeterminate since the lever arm Z is not known. In order to treat the posed problem analytically Evans assumed that a parabolic

compressive arch structure of constant thickness is formed within the beam (Fig 2.3b). He also assumed an identical thickness of the arch at the abutments and at mid-span equal to half of the beam thickness. Three modes of failure are considered: 1) crushing of the rock at the abutments or at mid-span; 2) buckling (snap through) failure of the beam; 3) sliding between the blocks and the abutments.

Beer and Meek (1982) reformulated and extended Evans's approach, introduced a coherent system of static equations, and evaluated the thickness of the compressive arch at the abutments and mid-span. Brady and Brown (1985) summarized the above-mentioned work and introduced an iterative algorithm for the evaluation of Voussoir beam stability. The iterative approach assumes initial load distribution and line of action, i.e. assuming initial n and Z . The analysis provides the compressive zone thickness, and the maximum axial thrust. The factor of safety against the previously mentioned failure modes can be calculated provided that the compressive strength of the rock, and the shear strength of the discontinuities are known. Sofianos (1996) statistically evaluated compressive arch thickness values, from the numerical data for different beam geometries provided by Wright (1974), thus eliminating static indeterminacy. Diederichs and Kaiser (1999) further improved the classic iterative approach by introducing improved assumptions for lateral stress distribution and arch compression, and by providing a numerical buckling limit.

The major advantages of the Voussoir beam technique are the ability to assess previously ignored failure by shear along the abutments, and providing static (although undetermined) formulation of the discussed problem. Two main disadvantages of this method regarding the actual geometry of the problem should be mentioned.

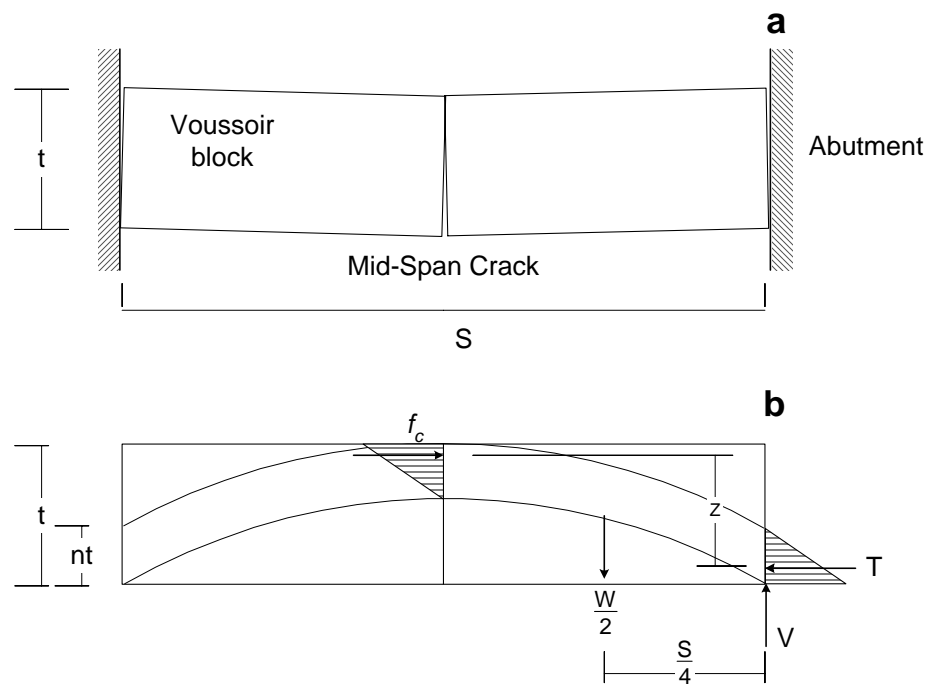


Figure 2.3. Evans' Voussoir beam: a) conceptual model; b) compressive stress distribution in the beam.

First, the Voussoir beam analogue overlooks the geometrical and mechanical properties of the transverse joints, i.e. joint friction and joint spacing. Second, only a single layer of the roof is considered in this analogue. It is not unreasonable to assume that the mutual interaction of individual blocks and layers in laminated and stratified rock masses will differ from those described by Fayol. Diederichs and Kaiser (1999) on their reply to Sofianos (1999) state *“It does seem intuitive that a numerical simulation (and the real case) with discrete joints through the beam should behave differently than the three hinged model. The main impact appears to be on the assumption or calculation of the effective arch thickness, n . Increased rotational freedom of the joints in the ubiquitous case should result in larger thickness at equilibrium while the three hinge model should exhibit n approaching zero for a stiff beam”*, where the ubiquitous model refers to a single, multi fractured beam. In absence of analytical solution, the stability of underground openings in laminated and jointed rock masses should be sought by means of numerical and physical modeling.

2.4. Numerical Approach

In rock mechanics, numerical methods are widely used to analyze the behavior of rock masses. For discontinuous rock masses the Finite Element Method (FEM), Finite Difference Method (FDM) and the Distinct Element Method (DEM¹) are the most popular.

2.4.1. The Finite Element Method

The FEM is probably the most popular method in civil and rock engineering, because it was the first numerical method with enough flexibility for the treatment of material heterogeneity, non-linear deformability (mainly plasticity), complex boundary conditions, in-situ stresses and gravity. Implementation of discontinuities into FEM has been motivated by

¹ DEM was later used for “Discrete Element Method”, and is often confused in practice.

rock mechanics need since the late 1960s. With the introduction of the joint element, first by Goodman et al., (1968), discontinuous rock mass can be analyzed by FEM. However the FEM joint element is based on continuum assumptions, therefore large-scale opening, sliding, and complete detachment of elements are not permitted. The zero thickness of the “Goodman joint element” causes numerical ill conditioning due to large aspect ratios (the ratio of length to thickness) of joint elements, and was improved by joint elements developed later on (e.g. Zeinkewitz et al., 1970; Ghaboussi et al., 1973; Desai et al., 1984).

Despite these efforts, the treatment of discontinuities remains the most important limiting factor in the application of the FEM for rock mechanics problems. The FEM suffers from the fact that the global stiffness matrix tends to be ill conditioned when many joint elements are incorporated. Block rotations, complete detachment and large-scale fracture opening cannot be treated because the general continuum assumption in FEM formulations requires that fracture elements cannot be torn apart.

2.4.2. *The Discrete Element Method (DEM)*

The key feature of DEM is that the domain of interest is treated as an assembly of rigid or deformable blocks or particles. The contacts between the blocks are recognized and updated during the entire motion/deformation process, and represented by appropriate constitutive models. Thus DEM allows finite displacements and rotations of discrete bodies, including complete detachment. The foundation of the method is the formulation and solution of equations of motion of rigid and/or deformable bodies using implicit (based on FEM discretization) or explicit (using FDM discretization) formulation. The basic difference between the discontinuous and the continuum-based models is that the contact patterns between components of the system is continuously changing with the deformation process for the former, but are fixed for the latter.

The explicit DEM, originally developed by Cundall (1971), is a force method that employs an explicit time marching scheme to solve directly the Newtonian motion equations, unbalanced forces drive the solution process, and numerical damping is used to dissipate energy. This method has been developed extensively since its introduction. The comprehensive DEM program UDEC (Universal Distinct Element Code) has powerful capabilities, which allow the modeling of variable rock deformability, non-linear joint behavior, fracture of intact rock, fluid flow and fluid pressure generation in joints and voids, and more (Lemos et al., 1985).

The implicit DEM is represented mainly by the Discontinuous Deformation Analysis (DDA), originated by Shi (1988). DDA is a displacement method, where the unknowns of the equilibrium equations are displacements. The formulation is based on minimization of the potential energy and contacts are treated using the “penalty” method. DDA has two major advantages over the explicit DEM: 1) relatively large time steps; and 2) closed form integrations for the stiffness matrices of the elements.

2.5. Numerical Modeling of the Voussoir Beam Using FEM and DEM

Wright (1972) conducted linear analysis of the Voussoir beam by FEM, and supported the failure modes as proposed by Evans. Two models of Voussoir beams were compared, one with a single mid-span joint and the other with 19 joints and concluded that the Voussoir with a single mid-span joint is the worst case. Chugh (1977) studied the stability of a jointed beam by using the stiffness matrix for beam elements. Pender (1985) demonstrated the effect of joint dilation in the stability analysis of Voussoir beam using a simplified model. Sepehr and Stimpson (1988) numerically studied the jointed roof in horizontally bedded strata with emphasis on developing the relationship between the roof deflection and joint spacing rather than analyzing failure modes. Passaris et al., (1993) have shown that crushing in high stress

areas and shear sliding are the most common failure modes encountered in mining environment, and showed that Wright's conclusion is erroneous, i.e. the multi jointed beam being the worst case. In their study however, the crushing failure was studied under the pre-condition that there was no shear sliding along the joints. Ran et al., (1994) studied the behavior of the jointed beam using non-linear FEM, and showed that the no shear pre-conditioning may result in over conservative estimate of roof strength. Both Passaris et al., (1993) and Ran et al., (1994) extended the analysis to multiple joints of variable spacing, however friction along joints was not modeled. FEM have limited applicability to the analysis of jointed rock masses since only small displacements/rotations are allowed, discontinuities are modeled as artificial-numerical interfaces, and new contacts are not automatically detected.

Sofianos and Kapenis (1998) studied the stability of the classic mid-span jointed Voussoir beam using UDEC. The mid-span joint model considers friction and cohesion along joints, although prescribing values rarely encountered in rocks: zero friction at the mid span and $\phi = 89^\circ$, $c = 10\text{GPa}$ at the abutment. Thus, elastic displacement at mid-span is prevented, and only separation without shear is allowed at the abutments, i.e. crushing will occur before slip commences. Nomikos et al., (2002) investigated the influence of joint frequency and compliance under similar boundary condition, thus precluding shear along abutments and off-center joints. Kaiser and Diederichs (1999) used UDEC to model a multi-jointed beam, their conclusions are discussed in the previous section.

2.6. Physical Modeling of the Voussoir Beam

Physical modeling of laminated rock masses began with Fayol's experiment in 1885. His observations and conclusions regarding the behavior of laminated beams have been described previously. Bucky (1931) studied the integrity of mine roof structures in rock, using

a centrifuge (the first mention of anyone actually undertaking centrifuge modeling). Small preformed rock structures were subjected to increasing accelerations until they ruptured. There was little or no instrumentation on the models and their significance is largely historical. This work was pioneering, but saw little continuation or development.

Evans (1941) studied the amount of deflection of brick beams, as an analog of the Voussoir beam. The deflection of the brick beams was analyzed as a function of lateral thrust (amount and eccentricity) and beam geometry. Evans summarized the experiments in the following “*...the tests on brick beams have served to show that, provided the end reactions are adequate, a Voussoir beam can be quite stable under its own weight even when traversed by numerous breaks and incapable of taking tensile forces.*”

Sterling (1980) performed a series of experiments on single and multi-layered rock beams simulating the behavior of continuous rock beams from initial structural integrity to incipient cracking and up to Voussoir beam geometry. The experiment design provided data on the applied transverse load, induced beam deflection, induced lateral thrust and eccentricity of the lateral thrust. Sterling drew the following conclusions: 1) roof beds cannot be simulated by continuous, elastic beams or plates, since their behavior is dominated by the blocks generated by natural joints or induced transverse cracks; 2) roof bed behavior is determined by the lateral thrust generated by deflection under gravity loading of the Voussoir beam against the confinement of the abutting rock; 3) a Voussoir beam behaves elastically over a satisfactory range. In addition, failure mode has been ascribed to various span to depth ratios and beam strength. Although pioneering, Sterling’s experiments overlooked physical and geometrical properties of rock joints, and again concentrated on crushing strength and buckling limits of the three-hinged Voussoir beam.

Passaris et al., (1993) and Ran et al., (1994) performed physical modeling of the Voussoir beam using blocks of lightweight (and low strength) concrete, complemented with

numerical (FEM) modeling. This research addressed the mechanical properties of joints, i.e. shear stiffness, and to a lesser extent geometrical properties. It has been shown, both numerically and experimentally, that the strength and stability of the Voussoir beam is decreased with increasing number of blocks. This conclusion is opposed to the fundamental statement of Wright, describing the Voussoir beam with a single mid joint as the “worst case”.

2.7. Case Studies

In contrast to extensive numerical, and to a lesser extent physical modeling, case studies documenting and analyzing the behavior and the failure modes of laminated and jointed roofs are sparse. Economopoulos et al., (1994) included in the design charts of Beer and Meek (1982) data collected from failures in bedded limestone roofs in Greek underground mining excavations. Hatzor and Benari (1998) have used DDA in back analysis of historic roof collapse in an underground water storage system excavated in densely laminated and jointed rock mass. However their geometrical dimensioning of the problem was conservative. Nevertheless, their research showed that: 1) the Voussoir beam analogy is unconservative; and 2) the stability of a laminated Voussoir beam is dictated by the interplay of friction angle along joints and joint frequency.

Sofianos et al., (1998) explored the deflections of roof in an underground marble quarry. In that research both numerical evaluation (FEM, DEM), deformation monitoring and Voussoir formulation were employed. Diederichs and Kaiser (1999) describe evidence of Voussoir arch action from monitored roof deflection in Mt. Isa, Australia, and in Winston Lake Mine, Canada.

2.8. Current Research Motivation

From the background material described above it is clear that the classical notation and solution of the Voussoir beam (the three hinged beam) is inadequate if a stability analysis of underground opening roof in laminated and jointed rock mass is attempted. The application of numerical methods is therefore inevitable. In order to closely simulate the deformation characteristic of a laminated Voussoir beam the numerical method should allow rigid body displacement and deformation to occur simultaneously. Convergence at every time step should be achieved after relatively large block displacements and rotation, without block penetration or tension. The vertical load must be evaluated and updated implicitly every time step, since it varies with the progress of block deformation. The model must incorporate the influence of joint friction on block displacement, stress transfer, and arching mechanism that develop with ongoing beam deformation. The Discontinuous Deformation Analysis (DDA) was developed specifically to meet such requirements. The scope of this thesis is to investigate the deformation characteristics of the laminated Voussoir beam using DDA.

Chapter 3 – DDA Basics: Review of Fundamentals

The description of DDA formulation presented bellow is brief. Thorough description of the DDA formulation is found in Shi (1988, 1993). Additional reading regarding extensions and improvements of DDA can be found in: Ke and Bray (1995); Amadei et al., (1996); Koo and Chern (1996); Kim et al., (1999); Jing et al., (2001).

3.1. Formulation of Simultaneous Equilibrium Equations

DDA models a discontinuous material as a system of individually deformable blocks that move independently without interpenetration. In the DDA method the formulation of the blocks is very similar to the definition of a finite element mesh. A finite element type of problem is solved in which all elements are physically isolated blocks bounded by pre-existing discontinuities. The discontinuities can in general be located anywhere with any direction, and length. Therefore, elements of any shape are expected. Both FEM and DDA require integration of polynomial functions over a general polygon area. In FEM, integrations are preformed using the Gaussian quadrature, which is only suitable for integration in triangular and rectangular elements. In DDA integrations are performed using the analytical Simplex solution (Shi, 1984), thus the elements can assume any given topology.

The displacements (u, v) at any point (x, y) in a block, can be related in two dimensions to six displacement variables

$$[D_i] = (u_0 \quad v_0 \quad r_0 \quad \varepsilon_x \quad \varepsilon_y \quad \gamma_{xy})^T \quad (3.1)$$

where (u_0, v_0) are the rigid body translations of a specific point (x_0, y_0) within a block, (r_0) is the rotation angle of the block with a rotation center at (x_0, y_0) , and ε_x , ε_y and γ_{xy} are the normal and shear strains of the block. For a two-dimensional formulation of DDA, the center of rotation (x_0, y_0) coincides with block centroid (x_c, y_c) . Shi (1988) showed that the complete first order approximation of block displacement takes the following form

$$\begin{pmatrix} u \\ v \end{pmatrix} = [T_i][D_i] = \begin{bmatrix} 1 & 0 & -(y-y_0) & (x-x_0) & 0 & (y-y_0)/2 \\ 0 & 1 & (x-x_0) & 0 & (y-y_0) & (x-x_0)/2 \end{bmatrix} [D_i] \quad (3.2)$$

This equation enables the calculation of displacements at any point (x, y) of the block when the displacements are given at the center of rotation and when the strains are known. By adopting first order displacement approximation, each block is a constant strain/stress element.

The local equations of equilibrium are derived using FEM style potential energy minimization. In DDA individual blocks form a system of blocks through contacts between blocks and displacement constraints which are imposed on a single block. For a block system defined by n blocks the simultaneous equilibrium equations are

$$\begin{pmatrix} K_{11} & K_{12} & K_{13} & \cdots & K_{1n} \\ K_{21} & K_{22} & K_{23} & \cdots & K_{2n} \\ K_{31} & K_{32} & K_{33} & \cdots & K_{3n} \\ \vdots & \vdots & \vdots & \ddots & \vdots \\ K_{n1} & K_{n2} & K_{n3} & \cdots & K_{nn} \end{pmatrix} \begin{Bmatrix} D_1 \\ D_2 \\ D_3 \\ \vdots \\ D_n \end{Bmatrix} = \begin{Bmatrix} F_1 \\ F_2 \\ F_3 \\ \vdots \\ F_n \end{Bmatrix} \text{ or } [K]\{D\} = \{F\} \quad (3.3)$$

where K_{ij} are 6×6 sub-matrices defined by the interactions of blocks i and j , D_i is a 6×1 displacement variables sub-matrix, and F_i is a 6×1 loading sub-matrix. In total the number of displacement unknowns is the sum of the degrees of freedom of all the blocks. The diagonal sub-matrices K_{ij} ($i = j$) represent the sum of contributing sub-matrices for the i -th block, namely block inertia and elastic strain energy. The off diagonal sub-matrices K_{ij} ($i \neq j$) represent the sum of contributing sub-matrices of contacts between blocks i and j and other inter-element actions like bolting. Concise derivation of single block energy functionals and

contributions to the global equations are given in section 3.2.2. Inter block contacts and their contributions to the global equations are given in section 3.2.3.

The i -th row of (3) consists of six linear equations

$$\frac{\partial \Pi}{\partial d_{ri}} = 0, r = 1, \dots, 6 \quad (3.4)$$

where d_{ri} are the deformation variables of block i .

The solution to the system of equations (3.3) is constrained by inequalities associated with block kinematics, as well as the no penetration and no tension condition between blocks. The kinematic constraints on the system are imposed using the penalty method. Contact detection is performed in order to determine possible contacts between blocks. Numerical penalties analogous to stiff springs are applied at the contacts to prevent penetration. Tension or penetration at the contacts results in expansion or contraction of the “springs”, a process that adds energy to the block system. Thus the minimum energy solution is one with no tension or penetration. When the system converges to an equilibrium state the energy of the contact forces is balanced by the penetration energy, resulting in inevitable very small penetrations. The energy of the penetrations is used to calculate the contact forces, which are in turn used to calculate the frictional forces along the interfaces between blocks. Shear displacement along the interfaces is modeled using Coulomb - Mohr failure criterion. Fixed boundary conditions are enforced in a manner consistent with the penalty method formulation. Stiff springs are applied at fixed points. Displacement of the fixed points adds considerable energy to the block system. Thus, a minimum energy solution satisfies the no displacement condition of the fixed points. The solution of the system of equations is iterative. First, the solution is checked to see how well the constraints are satisfied. If tension or penetration are found at contacts the constraints are adjusted by selecting new position for the contact springs and modified versions of $[K]$ and $\{F\}$ are formed for which a new solution

is attained. The process is repeated until each of the contacts converges to a constant state. The positions of the blocks are then updated according to the prescribed displacement variables. The large displacements and deformations are the accumulation of small displacements and deformations at each time step.

3.2. Energy Functionals and Contributions to Global Equilibrium Equations

According to the laws of thermodynamics a mechanical system under loading must move or deform in a direction that produces the minimum total energy of the system. The minimization of the system energy will produce an equation of motion for the system. In this section the energy functionals of: 1) elastic stresses; 2) initial stresses; 3) point loading; 4) line loading; 5) body forces; 6) inertia forces; and 7) kinematical constraints of the individual blocks, and their contributions to the global equilibrium equations are briefly described, following Shi (1993):

1) The elastic strain energy Π_e of block i is

$$\Pi_e = \iint \frac{1}{2} \begin{pmatrix} \varepsilon_x & \varepsilon_y & \gamma_{xy} \end{pmatrix} \begin{pmatrix} \sigma_x \\ \sigma_y \\ \tau_{xy} \end{pmatrix} dx dy \quad (3.5)$$

$$\Pi_e = \iint \frac{1}{2} \begin{pmatrix} \varepsilon_x & \varepsilon_y & \gamma_{xy} \end{pmatrix} \mathbf{E}_i \begin{pmatrix} \varepsilon_x \\ \varepsilon_y \\ \gamma_{xy} \end{pmatrix} dx dy$$

$$\Pi_e = \frac{1}{2} \iint \mathbf{D}_i^T \mathbf{E}_i \mathbf{D}_i dx dy$$

$$\Pi_e = \frac{S}{2} \mathbf{D}_i^T \mathbf{E}_i \mathbf{D}_i$$

where \mathbf{E}_i is the elasticity matrix, and S is the area of the i -th block.

The derivatives are

$$k_{rs} = \frac{\partial^2 \Pi_e}{\partial d_{ri} \partial d_{si}} = \frac{S}{2} \frac{\partial^2}{\partial d_{ri} \partial d_{si}} \mathbf{D}_i^T \mathbf{E}_i \mathbf{D}_i, \quad r, s = 1, \dots, 6 \quad (3.5.1)$$

$$k_{rs} = S \mathbf{E}_i$$

k_{rs} forms a 6×6 submatrix which is added to the sub-matrix K_{ii} in the global equation

2) The potential energy of the initial stresses Π_σ of block i is

$$\Pi_\sigma = - \iint (\varepsilon_x \quad \varepsilon_y \quad \gamma_{xy}) \begin{pmatrix} \sigma_x^o \\ \sigma_y^o \\ \tau_{xy}^o \end{pmatrix} dx dy \quad (3.6)$$

$$\Pi_\sigma = -S \mathbf{D}_i^T \{\sigma_0\}$$

The derivatives are

$$f_r = \frac{\partial \Pi_\sigma}{\partial d_{ri}} = S \frac{\partial \mathbf{D}_i^T \{\sigma_0\}}{\partial d_{ri}}, \quad r = 1, \dots, 6 \quad (3.6.1)$$

$$f_r = S \{\sigma_0\}$$

f_r forms a 6×1 submatrix which is added to $\{F_i\}$ in the global equation.

3) The potential energy of the point loading $\{\mathbf{F}\} = \begin{Bmatrix} f_x \\ f_y \end{Bmatrix}$ is

$$\Pi_p = -(u \quad v) \begin{Bmatrix} f_x \\ f_y \end{Bmatrix} = -\mathbf{D}_i^T \mathbf{T}_i^T \{\mathbf{F}\} \quad (3.7)$$

The derivatives are

$$f_r = -\frac{\partial \Pi_p}{\partial d_{ri}} = \frac{\partial \mathbf{D}_i^T \mathbf{T}_i^T \{\mathbf{F}\}}{\partial d_{ri}} = f_x t_{1r} + f_y t_{2r} \quad r = 1, \dots, 6 \quad (3.7.1)$$

f_r forms a 6×1 submatrix which is added to $\{F_i\}$ in the global equation.

4) The potential energy of load distributed on a straight line from point (x_1, y_1) to point (x_2, y_2) is

$$\Pi_l = -\int_0^1 (u \quad v) \begin{Bmatrix} F_x(t) \\ F_y(t) \end{Bmatrix} l dt = \mathbf{D}_i^T \int_0^1 \mathbf{T}_i^T \{\mathbf{F}(t)\} l dt \quad (3.8.)$$

where t is the parametric coefficient of the line equation, and l is the length of the line segment between the end points.

The derivatives are

$$f_r = -\frac{\partial \Pi_l}{\partial d_r} = \frac{\partial}{\partial d_r} \left(\mathbf{D}_i^T \int_0^1 \mathbf{T}_i^T \{\mathbf{F}(t)\} l dt \right) \quad r = 1, \dots, 6 \quad (3.8.1)$$

$$f_r = \int_0^1 \mathbf{T}_i^T \{\mathbf{F}(t)\} l dt$$

f_r forms a 6×1 submatrix which is added to $\{F_i\}$ in the global equation.

5) The potential energy of the of a constant body force $(f_x \quad f_y)$ acting on the volume of the i -th block is

$$\Pi_w = -\iint (u \quad v) \begin{Bmatrix} f_x \\ f_y \end{Bmatrix} dx dy = -\mathbf{D}_i^T \iint \mathbf{T}_i^T dx dy \begin{Bmatrix} f_x \\ f_y \end{Bmatrix} \quad (3.9)$$

$$\text{given } \iint \mathbf{T}_i^T dx dy = \begin{pmatrix} S & 0 \\ 0 & S \\ 0 & 0 \\ 0 & 0 \\ 0 & 0 \\ 0 & 0 \end{pmatrix} = \mathbf{S} \text{ then } \Pi_w = -\mathbf{D}_i^T \begin{pmatrix} f_x S \\ f_x S \\ 0 \\ 0 \\ 0 \\ 0 \end{pmatrix}$$

The derivatives are

$$f_r = -\frac{\partial \Pi_w}{\partial d_{ri}} = \frac{\partial}{\partial d_{ri}} \left(\mathbf{D}_i^T \begin{pmatrix} f_x S \\ f_x S \\ 0 \\ 0 \\ 0 \\ 0 \end{pmatrix} \right) = \begin{pmatrix} f_x S \\ f_x S \\ 0 \\ 0 \\ 0 \\ 0 \end{pmatrix} \quad r = 1, \dots, 6 \quad (3.9.1)$$

f_r forms a 6×1 submatrix which is added to $\{F_i\}$ in the global equation.

6) The potential energy of the inertia force Π_i of block i is

$$\Pi_i = -\iint (u \quad v) \begin{Bmatrix} f_x \\ f_y \end{Bmatrix} dx dy \quad (3.10)$$

The inertia force is $\begin{Bmatrix} f_x \\ f_y \end{Bmatrix} = -M \begin{Bmatrix} \frac{\partial^2 u(t)}{\partial t^2} \\ \frac{\partial^2 v(t)}{\partial t^2} \end{Bmatrix}$, where M is the mass per unit area and

$(u(t) \quad v(t))$ are time dependent displacements. Thus equation (3.10) transforms into

$$\Pi_i = \iint M (u \quad v) \begin{Bmatrix} \frac{\partial^2 u(t)}{\partial t^2} \\ \frac{\partial^2 v(t)}{\partial t^2} \end{Bmatrix} dx dy$$

$$\Pi_i = \iint M \mathbf{D}_i^T \mathbf{T}_i^T \mathbf{T}_i \frac{\partial^2 \mathbf{D}(t)}{\partial t^2} dx dy$$

Introducing time integration scheme (refer to section 3.4.) transforms equation (10) into

$$\Pi_i = \mathbf{D}_i^T \iint \mathbf{T}_i^T \mathbf{T}_i dx dy \left(\frac{2M}{\Delta t^2} \mathbf{D}(t_{j+1}) - \frac{2M}{\Delta t} \dot{\mathbf{D}}(t_j) \right) \quad (3.10.1)$$

where Δt is the time step size, and j is time step index.

The derivatives are

$$f_r = -\frac{\partial \Pi_w}{\partial d_{ri}} = -\frac{\partial}{\partial d_{ri}} \mathbf{D}_i^T \iint \mathbf{T}_i^T \mathbf{T}_i dx dy \left(\frac{2M}{\Delta t^2} \mathbf{D}(t_{j+1}) - \frac{2M}{\Delta t} \dot{\mathbf{D}}(t_j) \right) \quad r = 1, \dots, 6$$

$$f_r = \iint \mathbf{T}_i^T \mathbf{T}_i dx dy \left(\frac{2M}{\Delta t^2} \mathbf{D}(t_{j+1}) - \frac{2M}{\Delta t} \dot{\mathbf{D}}(t_j) \right) \quad (3.10.2)$$

which is added to $\{F_i\}$ in the global equation. Since there is unknown \mathbf{D}_i in equation

(3.10.2), this equation transforms to two parts

$$\frac{2M}{\Delta t^2} \iint \mathbf{T}_i^T \mathbf{T}_i dx dy \quad (3.10.3)$$

a 6×6 submatrix which is added to K_{ii} in the global stiffness matrix, and

$$\frac{2M}{\Delta t} \iint \mathbf{T}_i^T \mathbf{T}_i \, dx dy \dot{\mathbf{D}}(t_j) \quad (3.10.4)$$

a 6×1 submatrix which is added to $\{F_i\}$ in the global equation.

7) Displacement constraint at a point.

For a fixed point in a block the displacements are $\begin{Bmatrix} u(x, y) \\ v(x, y) \end{Bmatrix} = \{0\}$. Two stiff springs are

assigned in the x and y direction respectively. The stiffness of the springs is p and the spring

forces are $\begin{Bmatrix} f_x \\ f_y \end{Bmatrix} = -p \begin{Bmatrix} u \\ v \end{Bmatrix}$.

The potential energy of the spring Π_m is

$$\Pi_m = \frac{p}{2} (u \quad v) \begin{Bmatrix} u \\ v \end{Bmatrix} = \frac{p}{2} \mathbf{D}_i^T \mathbf{T}_i^T \mathbf{T}_i \mathbf{D}_i \quad (3.11)$$

The derivatives are

$$k_{rs} = \frac{\partial^2 \Pi_m}{\partial d_{ri} \partial d_{si}} = \frac{p}{2} \frac{\partial^2}{\partial d_{ri} \partial d_{si}} \mathbf{D}_i^T \mathbf{T}_i^T \mathbf{T}_i \mathbf{D}_i \quad r, s = 1, \dots, 6$$

$$k_{rs} = p \mathbf{T}_i^T \mathbf{T}_i \quad (3.11.1)$$

k_{rs} forms a 6×6 submatrix which is added to K_i in the global stiffness matrix.

3.3. Block System Kinematics and Contacts

Block system kinematics in DDA is constrained by the no tension no penetration condition between the blocks, mathematically described by a system of inequalities. As pointed out by Shi (1993) the minimization of total potential energy with inequality constraints is a non linear programming problem of high difficulty. However, when the block

system moves or deforms the blocks are in contact only along boundaries and the non penetration inequalities can be transformed into equations when the blocks are in contact.

The equations can be imposed on the global equation by adding numeric penalties to lock the movement in one or two directions. If two blocks have a tensile contact force between them, they will separate when the locks are removed. The global equations have to be solved repeatedly while selecting the lock position. Using this method the block system with tension and penetration can be corrected, by selection of lock position, until the fundamental constraints are satisfied.

3.3.1. Distance between two blocks

Two blocks meet at the next time step only if they are near at during the current time step. The distance between blocks i and j is defined as the minimum distance η_{ij} of any point pair $P_1(x_1, y_1)$ of block i and $P_2(x_2, y_2)$ of block j (Figure 3.1):

$$\eta_{ij} = \min \left\{ \sqrt{(x_2 - x_1)^2 + (y_2 - y_1)^2} \quad \forall (x_1, y_1) \in B_i, \forall (x_2, y_2) \in B_j \right\} \quad (3.12)$$

where \forall denotes “for all”.

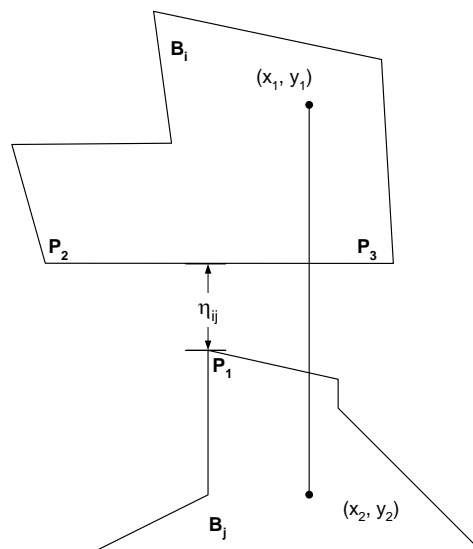


Figure 3.1. Distance of two blocks (after Shi, 1993)

If the distance η is greater than two times the maximum displacement ρ of all points of the blocks:

$$\eta_{ij} > 2\rho$$

$$\rho = \max \left\{ \sqrt{u(x,y)^2 + v(x,y)^2} \quad \forall (x,y) \in B_r, \quad r = 1 \dots n \right\} \quad (3.13)$$

then it is impossible for blocks i and j to meet during the next time step.

3.3.2. Contacts and interpenetration

In DDA there are three different types of block contacts: 1) angle to edge; 2) angle to angle; and 3) edge to edge (Figure 3.2). Edge to edge contacts can be transformed into two angle to edge contacts. For example, in Figure 3.2c the contact edges P_1P_2 and P_3P_4 can be transformed into two angle to edge contacts: 1) angle P_4 and edge P_1P_2 ; 2) angle P_1 and edge P_3P_4 . The angle to edge and the angle to angle contacts can be transformed into point-line crossing inequalities.

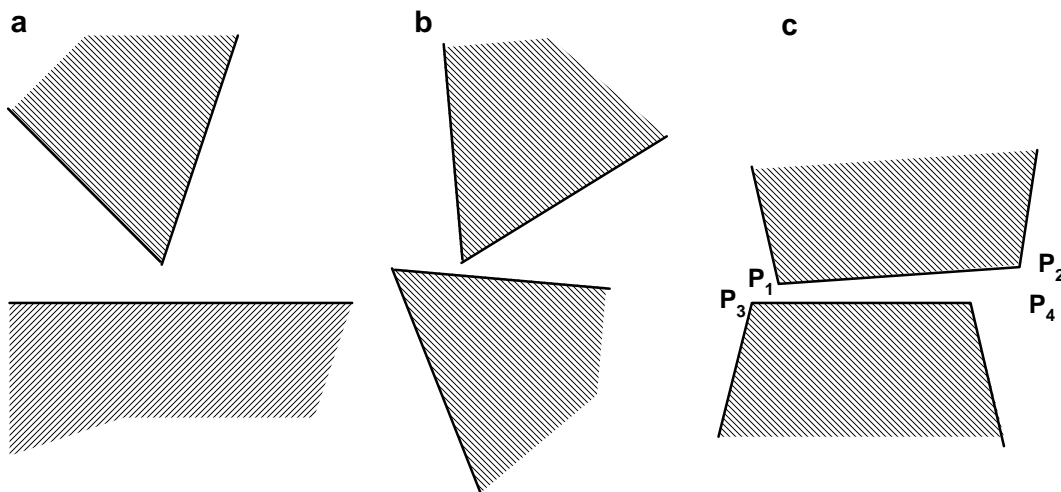


Figure 3.2. Types of blocks contact: a) angle to edge; b) angle to angle; c) edge to edge (after Shi, 1993).

An edge and an angle are defined to be in contact if the distance from angle to edge is less than ρ and if there is no overlapping when angle vertex translates to the edge without rotation. In Figure 3.3a there is overlapping when non rotational translation is made, and therefore the angle and the edge are not in contact.

Two angles are defined to be in contact if the distance between the vertices is less than ρ and if there is no overlapping when angle vertex translates to the edge without rotation until the vertices coincide. In Figure 3.3b there is overlapping and therefore the two angles are not in contact. The concept of contact is extremely important: if there is no penetration at the contacts there is no penetration in the whole block system.

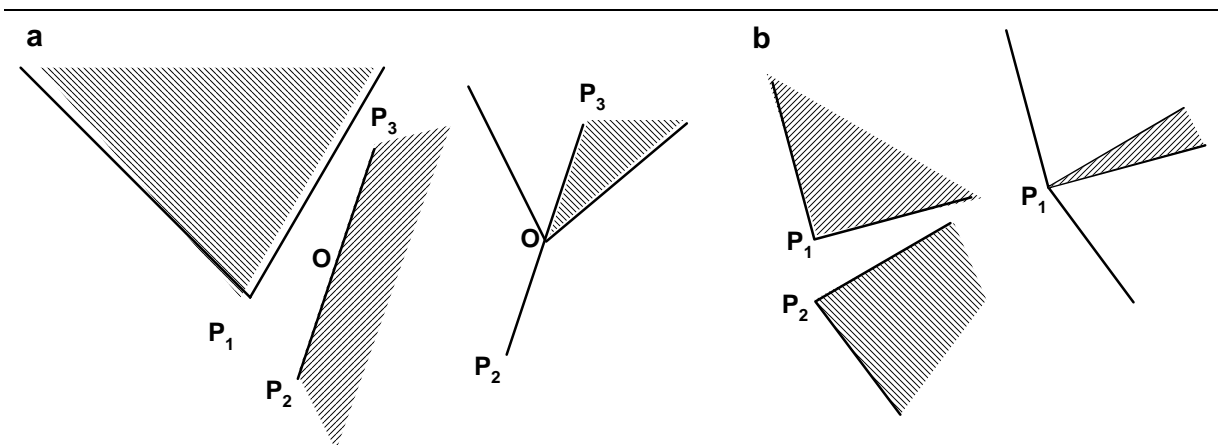


Figure 3.3 Contact conditions: a) overlapping angle and edge; b) overlapping angles (modified after Shi,1993)

3.3.3. Energy functional of a stiff contact

If a vertex of block i with coordinates (x_1, y_1) is penetrating an edge of block j with vertices (x_2, y_2) and (x_3, y_3) , the penetration distance d can be denoted as

$$d = \frac{\Delta}{l} \left| \begin{array}{ccc} 1 & x_1 + u_1 & y_1 + v_1 \\ 1 & x_2 + u_2 & y_2 + v_2 \\ 1 & x_3 + u_3 & y_3 + v_3 \end{array} \right| = \frac{1}{l} \left(S_0 + \left| \begin{array}{ccc} 1 & u_1 & y_1 \\ 1 & u_2 & y_2 \\ 1 & u_3 & y_3 \end{array} \right| + \left| \begin{array}{ccc} 1 & x_1 & v_1 \\ 1 & x_2 & v_2 \\ 1 & x_3 & v_3 \end{array} \right| \right) \quad (3.14)$$

where l is the edge length, $S_0 = \begin{vmatrix} 1 & x_1 & y_1 \\ 1 & x_2 & y_2 \\ 1 & x_3 & y_3 \end{vmatrix}$ and $\begin{vmatrix} 1 & u_1 & v_1 \\ 1 & u_2 & v_2 \\ 1 & u_3 & v_3 \end{vmatrix}$ is a second order

infinitesimal which can be neglected.

Δ can be represented as

$$\Delta = S_0 + (y_2 - y_3 \quad x_3 - x_2) \begin{Bmatrix} u_1 \\ v_1 \end{Bmatrix} + (y_3 - y_1 \quad x_1 - x_3) \begin{Bmatrix} u_2 \\ v_2 \end{Bmatrix} + (y_1 - y_2 \quad x_2 - x_1) \begin{Bmatrix} u_3 \\ v_3 \end{Bmatrix}$$

$$\Delta = S_0 + (y_2 - y_3 \quad x_3 - x_2) \mathbf{T}_i(x_1, y_1) \mathbf{D}_i$$

or

$$+ (y_3 - y_1 \quad x_1 - x_3) \mathbf{T}_j(x_2, y_2) \mathbf{D}_j \quad (3.14.1)$$

$$+ (y_1 - y_2 \quad x_2 - x_1) \mathbf{T}_j(x_3, y_3) \mathbf{D}_j$$

Introducing equation (3.12.1) in to equation (3.12) yields

$$d = \frac{S_0}{l} + \mathbf{e} \mathbf{D}_i + \mathbf{g} \mathbf{D}_j \quad (3.14.2)$$

or

$$d = \frac{S_0}{l} + \sum_{r=1}^6 e_r d_{ri} + \sum_{r=1}^6 g_r d_{rj}$$

where \mathbf{e} and \mathbf{g} are 1×6 coefficients matrices:

$$e_r = [(y_2 - y_3) t_{1r}(x_1, y_1) + (x_3 - x_2) t_{2r}(x_1, y_1)] / l$$

$$g_r = [(y_3 - y_1) t_{1r}(x_2, y_2) + (x_1 - x_3) t_{2r}(x_2, y_2)] / l$$

$$+ [(y_1 - y_2) t_{1r}(x_3, y_3) + (x_2 - x_1) t_{2r}(x_3, y_3)] / l$$

The strain energy of the contact spring is

$$\Pi_c = \frac{p}{2} d^2 = \frac{p}{2} \left(\frac{S_0}{l} + \sum_{r=1}^6 e_r d_{ri} + \sum_{r=1}^6 g_r d_{rj} \right)^2 \quad (3.15)$$

where p is the spring stiffness.

Minimizing Π_c by taking derivatives, four 6×6 submatrices and two 6×1 submatrices are obtained and added to K_{ii} , K_{ij} , K_{ji} , K_{jj} , F_i and F_j respectively.

$$k_{rs} = \frac{\partial^2 \Pi_k}{\partial d_{ri} \partial d_{si}} = \frac{p}{2} \frac{\partial^2}{\partial d_{ri} \partial d_{si}} \left(\sum_{r=1}^6 e_r d_{ri} \right)^2 \quad (3.16)$$

$$k_{rs} = p e_r e_s \quad r, s = 1, \dots, 6$$

k_{rs} is a 6×6 submatrix which is added to K_{ii} in the global equation.

$$k_{rs} = \frac{\partial^2 \Pi_k}{\partial d_{ri} \partial d_{sj}} = \frac{p}{2} \frac{\partial^2}{\partial d_{ri} \partial d_{sj}} \sum_{r=1}^6 (e_r d_{ri}) \sum_{r=1}^6 (g_r d_{rj}) \quad (3.17)$$

$$k_{rs} = p e_r g_s \quad r, s = 1, \dots, 6$$

k_{rs} is a 6×6 submatrix which is added to K_{ij} in the global equation.

$$k_{rs} = \frac{\partial^2 \Pi_k}{\partial d_{rj} \partial d_{si}} = \frac{p}{2} \frac{\partial^2}{\partial d_{rj} \partial d_{si}} \sum_{r=1}^6 (e_r d_{ri}) \sum_{r=1}^6 (g_r d_{rj}) \quad (3.18)$$

$$k_{rs} = p g_r e_s \quad r, s = 1, \dots, 6$$

k_{rs} is a 6×6 submatrix which is added to K_{ji} in the global equation.

$$k_{rs} = \frac{\partial^2 \Pi_k}{\partial d_{rj} \partial d_{sj}} = \frac{p}{2} \frac{\partial^2}{\partial d_{rj} \partial d_{sj}} \left(\sum_{r=1}^6 g_r d_{rj} \right)^2 \quad (3.19)$$

$$k_{rs} = p g_r g_s \quad r, s = 1, \dots, 6$$

k_{rs} is a 6×6 submatrix which is added to K_{jj} in the global equation.

$$f_r = -\frac{\partial \Pi_k}{\partial d_{ri}} = -\frac{p S_0}{l} \frac{\partial}{\partial d_{ri}} \sum_{r=1}^6 (e_r d_{ri}) \quad (3.20)$$

$$f_r = -\frac{p S_0 e_r}{l} \quad r = 1, \dots, 6$$

f_r is a 6×1 submatrix which is added to F_i in the global equation.

$$f_r = -\frac{\partial \Pi_k}{\partial d_{ij}} = -\frac{p S_0}{l} \frac{\partial}{\partial d_{ri}} \sum_{r=1}^6 (g_r d_{rj}) \quad (3.21)$$

$$f_r = -\frac{p S_0 g_r}{l} \quad r = 1, \dots, 6$$

f_r is a 6×1 submatrix which is added to F_j in the global equation.

3.3.4. Limitations of DDA stiff contact formulation

In DDA the contact stiffness is determined at the beginning of the computation and is kept constant throughout the entire calculation. In deforming rock masses some deformation is taking place at the contacts. Deformation of the contacts and subsequent changes of contact areas and angles are not accounted by DDA. This deformation consumes energy, which is not accounted by as well.

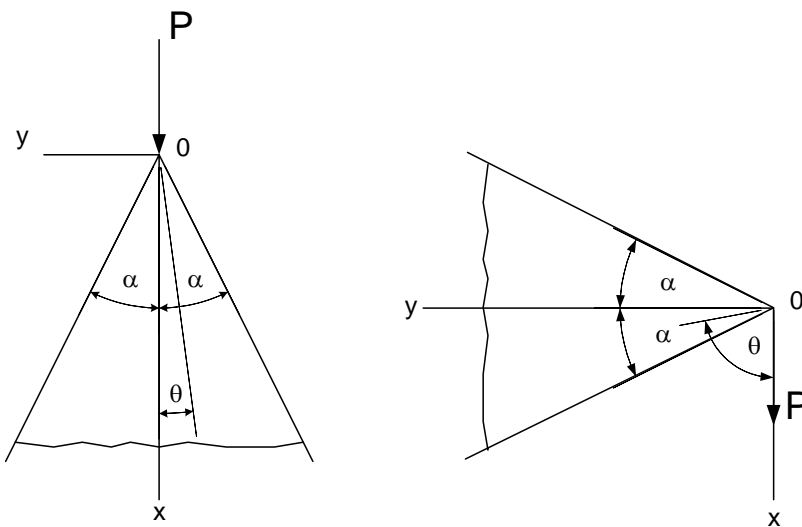


Figure 3.4. A wedge loaded by normal and tangential forces at the apex (after Timoshenko and Goodier, 1951)

Timoshenko and Goodier (1951) describe the stress concentration at wedge (similar to a DDA edge) loaded by a normal and tangential forces at the apex (Figure 3.4). The radial stress concentration due to normal loading within the wedge is given by:

$$\sigma_r = -\frac{P \cos \alpha}{r(\alpha + \frac{1}{2} \sin 2\alpha)} \quad (3.22a)$$

The tangential stress concentration due to normal loading within the wedge is given by:

$$\sigma_r = -\frac{P \cos \alpha}{r(\alpha - \frac{1}{2} \sin 2\alpha)} \quad (3.22b)$$

Clearly the stress concentration is a function of the geometrical factor $k = \frac{1}{(\alpha \pm \frac{1}{2} \sin 2\alpha)}$,

which is related to the vertex angle 2α . During deformation this angle is expected to change, and so does the factor k . This factor bears similarity to contact stiffness, relates stress to force, and can be transformed into a formal stiffness, which relates force to displacement, by the application of Hooke's law. Therefore, it can be assumed that contact stiffness is expected to change during deformation as well.

DDA version used in this research assumes first order displacement function, resulting in homogeneously deformable elements. In order to accommodate a realistic contact formulation, as described above, high order displacement functions should be used. High order displacement functions were implemented into DDA by various investigators (refer to Hsiung, S-M, 2001), however the contact stiffness was modeled using constant stiffness springs. Amadei et al., (1996) reformulated the contact scheme by substituting the stiff contacts by Lagrangian multipliers, which are constantly updated through the computational cycles. However, this technique is essentially numerical with vague physical meaning.

Future development of the DDA should account for this deficiency, if more accurate description of deformation is desired.

3.4. Time Integration Scheme

DDA time integration scheme adopts the Newmark (1959) approach, which for a single degree of freedom can be written in the following manner:

$$\begin{aligned} u_{i+1} &= u_i + \Delta t \dot{u}_i + \left(\frac{1}{2} - \beta\right) \Delta t^2 \ddot{u}_i + \beta \Delta t^2 \ddot{u}_{i+1} \\ \dot{u}_{i+1} &= \dot{u}_i + (1 - \gamma) \Delta t \ddot{u}_i + \gamma \Delta t \ddot{u}_{i+1} \end{aligned} \quad (3.23)$$

where \ddot{u} , \dot{u} , and u are acceleration, velocity, and displacement respectively, Δt is the time step, β and γ are the collocation parameters defining the variation of acceleration over the time step. Unconditional stability of the scheme is assured for $2\beta \geq \gamma \geq 0.5$. DDA integration scheme uses $\beta = 0.5$ and $\gamma = 1$, thus setting the acceleration at the end of the time step to be constant over the time step. This approach is implicit and unconditionally stable.

Along with unconditional stability this set of collocation parameters assures a high algorithmic damping (Wang et al., 1996). This phenomenon is commonly observed when numerical methods are used to analyze the dynamic behavior of elastic systems.

Consider a two block system, as depicted in Figure 3.1. The equilibrium solution of the vertical stress at the centroid of the upper block is $\sigma_y = 0.01226 \text{ MPa}$. The effect of algorithmic damping can be seen in Figure 3.2a, which is a plot of the vertical stress at the centroid of the upper block versus time. DDA solution equilibrates with time, as is clearly seen for the case of contact spring stiffness $g_0 = 50 \cdot 10^6 \text{ MN/m}$. For higher contact stiffness the solution further stabilizes.

The effect of increased contact stiffness is seen in Figure 3.2b, which is a plot of the relative numeric error versus time. The relative numeric error is defined as:

$$e_n(\%) = \frac{\sigma_y - \sigma_y^*}{\sigma_y} \cdot 100 \quad (3.21)$$

where σ_y is equilibrium solution vertical stress and σ_y^* is the numerically calculated vertical stress; both are taken at the upper block centroid. It is clearly seen that algorithmic damping is active for the lower contact stiffness, where the numeric error is reduced from initial value of 3% to 0.3% over 20 time steps. As contact stiffness approaches infinity the numeric error declines, as low as 0.01% for contact stiffness of $100 \cdot 10^9 \text{ MN/m}$. Thus, it can be concluded that DDA solution approaches equilibrium solution faster with increased contact stiffness.

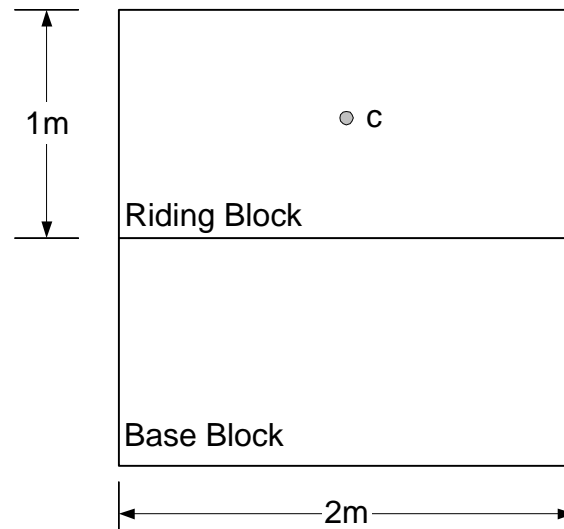


Figure 3.5. Two block system.

The origin of the initial error is the contact force perturbation at the initial time step of the computation, at gravity turn-on. As shown by Doolin and Sitar (2002) initial contact force perturbation is inversely proportional to the time step size. This effect can be seen in Figure 3.3, which shows the DDA solution (Fig. 3.3a) and the numeric error (Fig. 3.3b) of the previously described problem. For a time step of $\Delta t = 0.05\text{sec}$ the initial perturbation is of approximately 4%. Reducing the time step size, up to magnitude order scale, results in higher initial error. However, the convergence of DDA solution is markedly enhanced by time step size reduction, down to a numeric error of 0.005%.

From the above discussion, it is clear that the accuracy of DDA solution is governed by two parameters: 1) time step size; 2) contact stiffness. The most accurate solution is attained for smaller time step size and higher values of contact stiffness. This effect will be discussed further in the following chapters.

3.5. DDA Numeric Implementation

Computer implementation of DDA allows control over the analysis procedure through a set of user specified control parameters:

1. Dynamic control parameter ($k01$) – defines the type of analysis required, from quasi-static to fully dynamic. For quasi-static analysis the velocity of each block at the beginning of each time step is set to zero, $k01 = 0$. In case of dynamic analysis the velocity of each block at the end of a time step is fully transferred to the next time step, $k01 = 1$. Different values from 0 to 1 correspond to different degrees of inter step velocity transfer, comparable to damping or energy dissipation. For example, for an input value of $k01 = 0.95$ the velocity in the beginning of each time step is 5% lower than the terminal velocity at the previous time step.
2. Penalty value ($g0$) – is the stiffness of the contact springs used to enforce contact constraints between blocks.
3. Upper limit of time step size ($g1$) – the maximum time interval that can be used in a time step, should be chosen so that the assumption of infinitesimal displacement within the time step is satisfied.
4. Assumed maximum displacement ratio ($g2$) – the calculated maximum displacement within a time step is limited to an assumed maximum displacement in order to ensure infinitesimal displacements within a time step. The assumed maximum displacement is defined as $U_{max} = (g2) \cdot (y/2)$, where y is the length of the analysis domain in the y -direction. This parameter is also used to detect possible contacts between blocks: if the distance between separated vertices or edges of neighboring blocks is less than $2.5(g2) \cdot (y/2)$ then the blocks are in contact. If $g2$ is too large there are too many unnecessary contacts, if $g2$ is too small unrealistic inter-block penetration can occur.

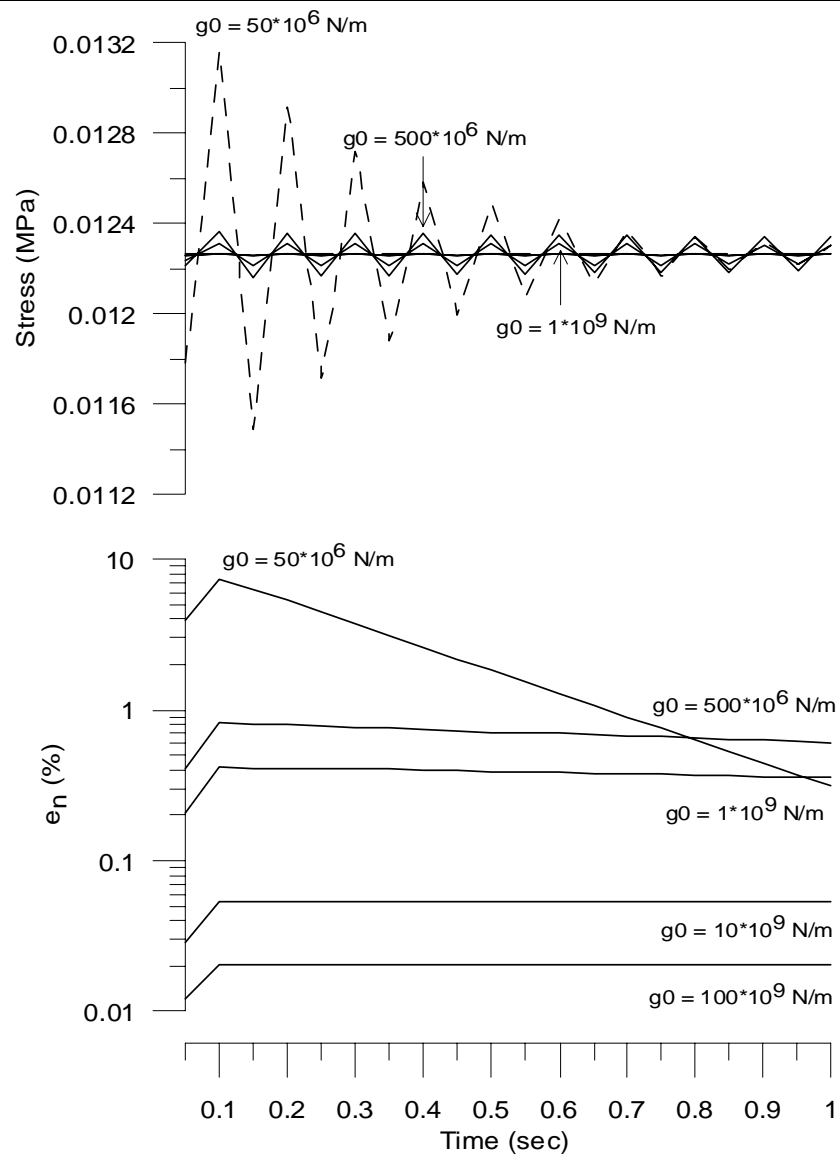


Figure 3.6. DDA results for the two block system: for a time step size of $g_1 = 0.005$ sec a) vertical stress at the centroid of the upper block for different values of contact stiffness; b) relative numeric error for different values of contact stiffness.

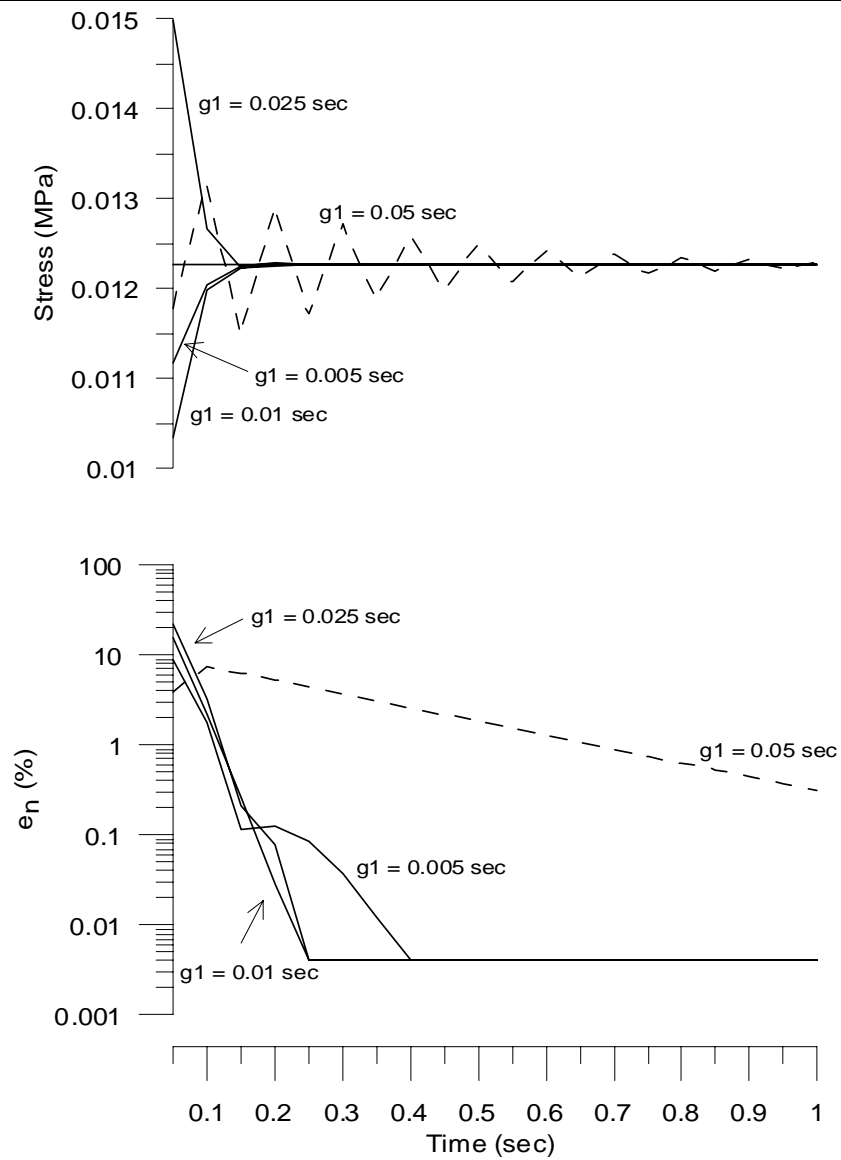


Figure 3.7. DDA results for the two block system for contact stiffness of $g_0 = 50 \cdot 10^6 \text{ N/m}$: a) vertical stress at the centroid of the upper block for different values of time step size (g_1) ; b) relative numeric error for different values of time step size (g_1).

Chapter 4 – Validation of DDA Using Analytical Solutions and Shaking Table Experiments

4.1. Introduction

Realistic simulation of a large number of individually deformable particles/blocks requires the application of DEM, such as the Distinct Element Method (Cundall, 1971) or the Discontinuous Deformation Analysis (Shi, 1988). Ever-growing popularity of numerical schemes, in hand with availability of computing power eases the application of computer-based methods. However, successful application of numerical methods to large-scale engineering problems requires rigorous validation of these methods using analytical solutions, laboratory scale models, and case studies.

Yeung (1991) and MacLaughlin (1997) tested the accuracy of DDA for applications ranging from tunneling to slope stability, using problems for which analytical or semi-analytical solutions exist. Doolin and Sitar (2002) explored the kinematics of a block on an incline for sliding distances of up to 250 meters. Hatzor and Feintuch (2001) validated DDA using direct dynamic input. Analytical integration of sinusoidal functions of increasing complexity was compared to displacements prescribed by DDA for a single block on an incline subjected to the same acceleration functions as integrated analytically.

The necessity for DDA validation using analytical solutions is evident if the method is to be adopted by the engineering profession. However, analytical solutions are only valid for the inherent underlying simplifying assumptions. This limitation can be overcome by

comparison between DDA prediction and experimental results of carefully planned physical models. Up to date, such attempts have been limited, or practically non-existent for the dynamic problem.

O’Sullivan and Bray (2001) simulated the behavior of hexagonally packed glass rods subjected to bi-axial compression, showing the advantages of DDA in the study of soil dynamics. McBride and Scheele (2001) validated DDA using a multi-block array on an incline subjected to gravitational loading, and a bearing capacity model.

Validation of DDA using analytical solutions showed that DDA accurately predicts single block displacements, up to tens of meters. However, validation using physical models proved less successful. In particular, it was found that kinetic damping is required for reliable prediction of displacement (McBride and Scheele, 2001).

The aim of this chapter is to validate DDA using fully dynamic shaking table model. The accuracy of DDA is explored, and the influence of the numeric control parameters is studied in detail.

4.2. Validation of DDA Using an Analytical Solution

A Fourier series composed of sine components represents the simplest form of harmonic oscillations, in general notation

$$a(t) = \sum_{i=1}^n a_i \sin(\omega_i t) \quad (4.1)$$

where a_i and ω_i are the amplitude (acceleration in this case) and frequency respectively.

The displacement of a mass subjected to dynamic loading is attained by double integration of the acceleration record (Eq. 4.1) from θ to t :

$$d(t) = \sum_{i=1}^n \frac{a_i}{\omega_i^2} [-\sin \omega_i t + \sin \omega_i \theta + \omega_i (t - \theta) \cos \omega_i \theta_i] \quad (4.2)$$

where θ is the time at which yield acceleration a_y is attained.

Goodman and Seed (1965) showed that for frictional sliding of a single block on a plane inclined by α degrees, where cohesion along the sliding plane is zero, the down slope horizontal yield acceleration (a_y) is

$$a_y = \tan(\phi_d - \alpha)g \quad (4.3)$$

Up slope horizontal yield acceleration is

$$a_y = \tan(\phi_d + \alpha)g \quad (4.4)$$

where ϕ_d is the displacement dependent friction angle. It is apparent that up slope motion requires significantly higher accelerations, which in most cases preclude up slope displacement.

Hatzor and Feintuch (2001) showed that for an acceleration function consisting of sum of three sines DDA prediction is accurate within 15% of the analytic solution without application of damping, provided that the numeric control parameters $g1$, $g2$ are carefully optimized. Moreover, they argued that the influence of higher order terms in a series of sine function is negligible. Hatzor and Feintuch demonstrated their validation for arbitrary selected constants, $a_1 = \omega_1 = 1$, $a_2 = \omega_2 = 2$, $a_3 = \omega_3 = 3$. The prescribed values produce a low frequency dynamic input assuring a nearly constant block velocity, which was attained at the beginning of the analysis (*ca.* 20% of elapsed time).

In order to attain a better understanding of the frequency effect upon the numerical solution we have extended the analysis to higher frequencies, constraining the peak horizontal acceleration to $0.15g$. A typical input motion of sum of three sines is presented in Figure 4.1a. The analysis was performed for a single block resting on a plane inclined $\alpha = 15^\circ$ to the horizontal. The block material properties were: density = 2700 kg/m^3 , $E = 5000 \text{ MPa}$, and $\nu = 0.25$. The friction angle of the sliding plane was set to $\phi = 15^\circ$, thus the yield acceleration (a_y

$= 0$) was attained immediately at the beginning of analysis ($\theta = 0 \text{ sec}$). Three different sets of frequencies were modeled (Tab. 4.1). Constant values of numeric spring stiffness $g0 = 1000 \text{ MN/m}$, assumed maximum displacement ratio $g2 = 0.0075$, and dynamic control parameter $k01 = 1$ were used.

Set	$\omega_1 (\pi) \mathbf{a}_1 (\mathbf{g})$	$\omega_2 (\pi) \mathbf{a}_2 (\mathbf{g})$	$\omega_3 (\pi) \mathbf{a}_3 (\mathbf{g})$
1	8, 0.1	4, 0.05	2, 0.025
2	10, 0.1	5, 0.05	2.5, 0.025
3	15, 0.1	7.5, 0.05	3.75, 0.025

Table 4.1. Frequency sets for a loading function consisting of a sum of three sines.

Each set was modeled twice, first the time step was set to $g1 = 0.005 \text{ sec}$, then the time step was halved to $g1 = 0.0025 \text{ sec}$. Comparison between the analytical solution and the numerical solution of the total displacement are presented in Fig. 4.1b, where excellent agreement between the analytical and DDA solutions are shown, regardless of frequency.

The relative numeric error is defined as:

$$e_n(\%) = \frac{\|d - d_N\|}{\|d\|} \cdot 100 \quad (4.5)$$

and the relative numeric difference is defined as:

$$e'(\%) = \frac{\|d\| - \|d_N\|}{\|d\|} \cdot 100 \quad (4.6)$$

where d and d_N are the analytical and the numeric displacement vectors respectively.

$\|\cdot\|$ is the norm operator.

The relative numeric error for $g1 = 0.005 \text{ sec}$ simulations is within 4.5%. Halving the time step reduces the relative numeric error to 1.5%.

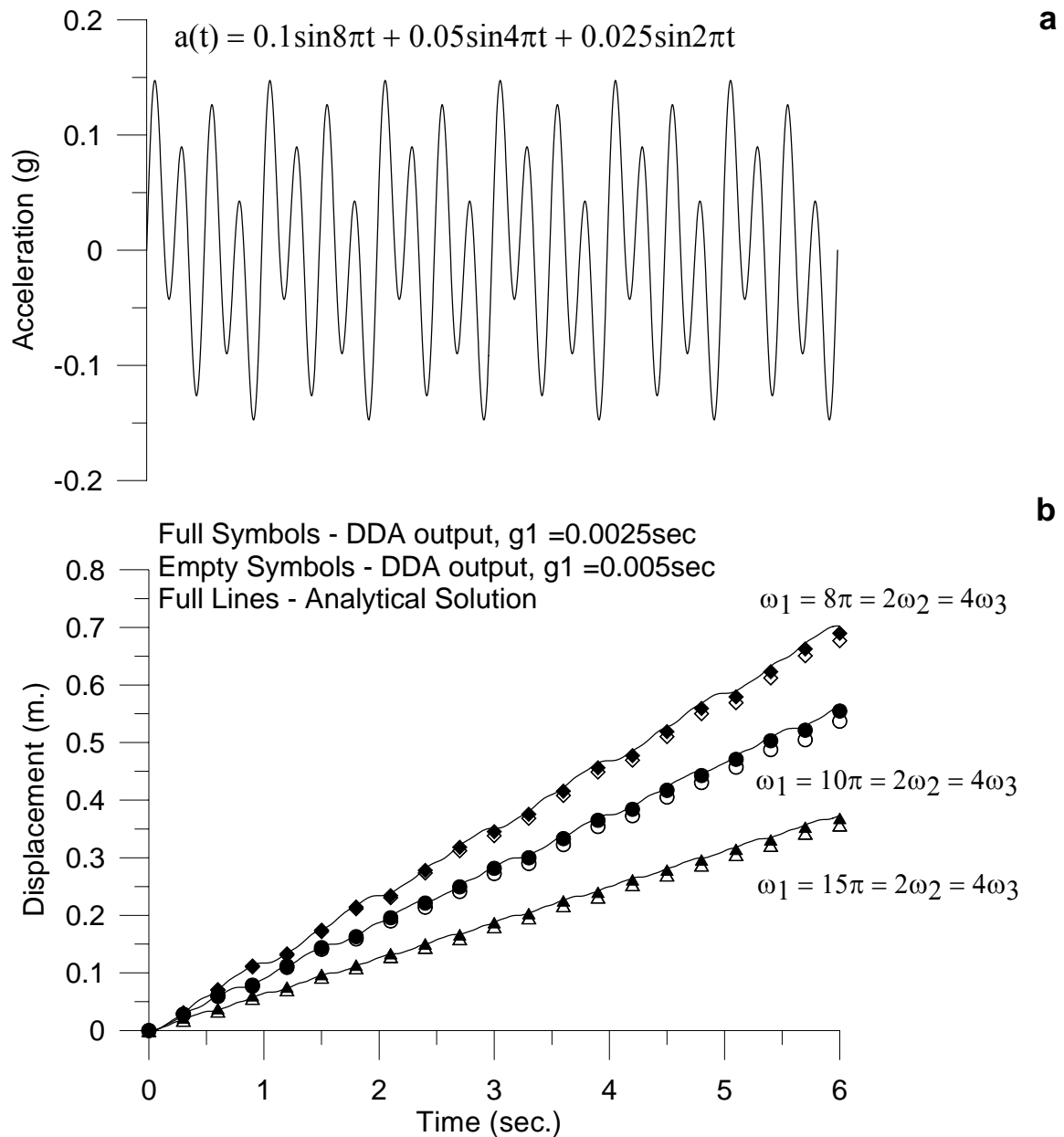


Figure 4.1. a) the loading function $a(t) = a_1\sin(\omega_1 t) + a_2\sin(\omega_2 t) + a_3\sin(\omega_3 t)$; b) comparison between analytical and DDA solution for block displacement subjected to a loading function consisting of a sum of three sines. All DDA simulations for: $g_0 = 1 \cdot 10^9 \text{ N/m}$; $g_2 = 0.0075$; block elastic modulus $E = 5000 \cdot 10^6 \text{ N/m}$. All input motions are for $\omega_1 = 2\omega_2 = 4\omega_3$.

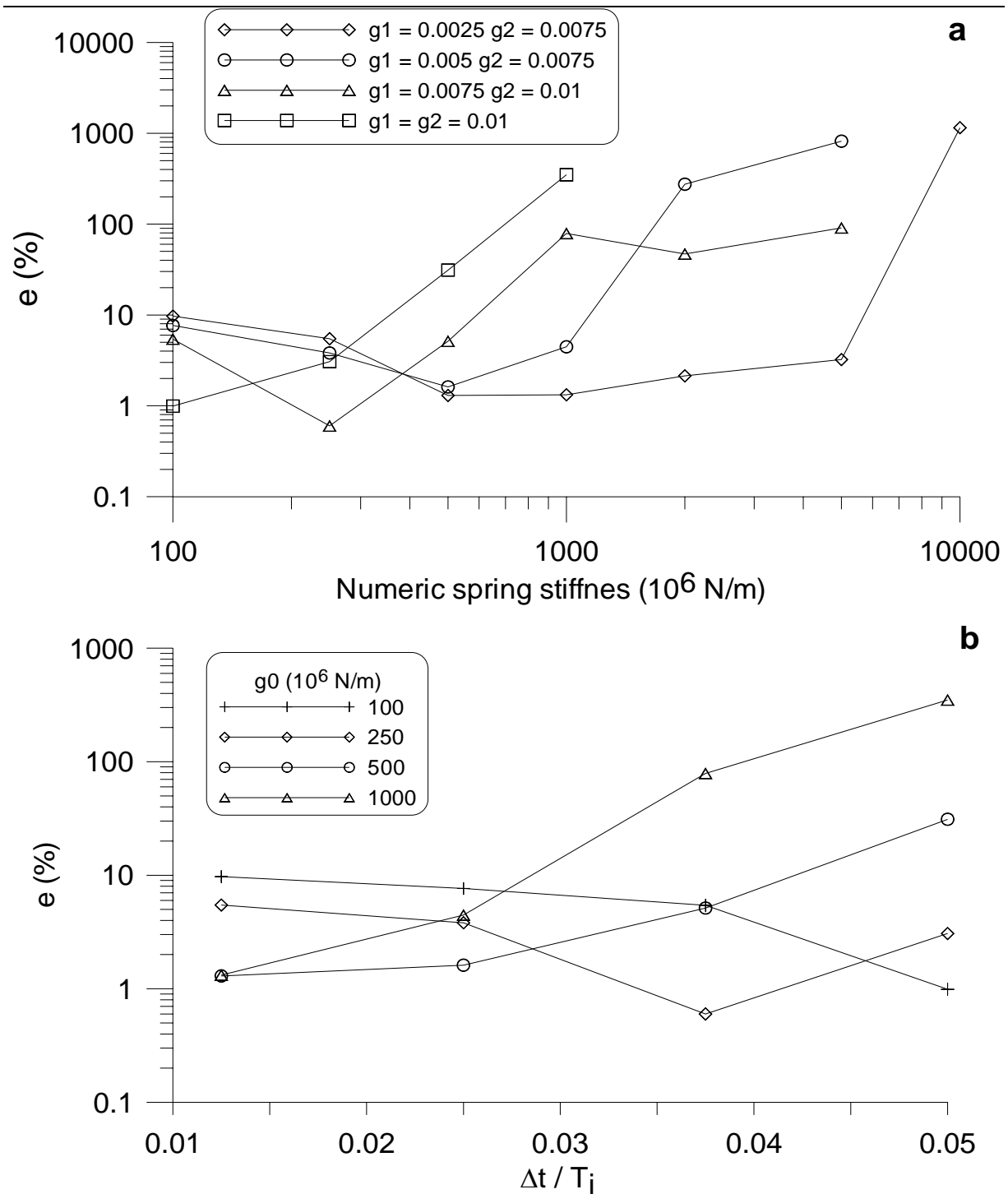


Figure 4.2. Sensitivity analysis of the DDA numeric control parameters. Relative numeric error of ultimate displacement prediction as a function of: a) contact spring stiffness; b) time step size (Δt) normalized to input motion frequency (T_i).

The interrelationship of the numeric control parameters was further investigated using the input function of set 2 (Table 4.1). Figure 4.2 shows the dependence of the numeric error on the choice of the numeric control parameters $g1$, $g2$ and the numeric spring stiffness $g0$ (the penalty value). It is found that for an optimized set of $g1$ and $g2$ ($g1 = 0.0025 \text{ sec}$ and $g2 = 0.0075$) the DDA solution is not sensitive to the penalty value, which can be changed over a range of two orders of magnitude, from $100 \times 10^6 \text{ N/m}$ to $5000 \times 10^6 \text{ N/m}$. Within this range the numeric error never exceeds 10% and in most cases approaches the value of 1%. For values lower than $50 \times 10^6 \text{ N/m}$ block penetration occurs. Stiffer contact springs reduce the magnitude of displacement until a certain minimum is reached. Further increase in the spring stiffness results in an introduction of a large numeric error into the DDA solution.

Departing from the optimal $g1$, $g2$ combination results in increased sensitivity of the DDA solution to the penalty value. The departure from the analytical solution occurs at lower penalty values with increasing time step size.

Examining the optimal time step size (Fig. 4.2b) shows that time step optimization is not a simple procedure. It is clear that highest accuracy is attained for a small time step – high stiffness combination. However, enlargement of the time step size produces a different response of the mechanical system: for higher stiffness values the numeric error tends to grow, while for the lower ones it tends to decrease. Thus, an optimal combination is not easily defined: the lowest numeric error ($e = 0.6\%$) is attained for the following combination $\Delta t/T_i = 0.0375$ and $g0 = 250 \times 10^6 \text{ N/m}$. For the same time step size the errors for $g0 = 500 \times 10^6 \text{ N/m}$ and $g0 = 1000 \times 10^6 \text{ N/m}$ are of an order of magnitude larger. However, the numerical stability of DDA is assured regardless of the contact stiffness when time step size is taken sufficiently low.

4.3. Validation of DDA by Shaking Table Experiments

It has been shown that there is a very good agreement between the DDA and analytic solutions for the block on an incline problem. However, the analytical solution is only an approximation to the physical problem with various simplifying assumptions including: perfectly rigid block, constant friction, and complete energy conservation. Comparison between DDA results and physical modeling can help us probe into the significance of these assumptions. In the following section validation of DDA using a physical model of a block on an incline subjected to dynamic loading is described.

4.3.1. *Experimental setting*

The physical modeling used in this research was performed by Wartman et al., (2003) at the Earthquake Simulation Laboratory of the University of California at Berkeley. The tests were performed on a large hydraulic driven shaking table, producing accurate, well controlled, and repeatable motions to frequencies up to 14 Hz. The table was driven by a 222.4 kN (50 kip) force, 15.24 cm (6 in.) stroke range hydraulic actuator manufactured by MTS. The system was closed loop servo controlled. A Hewlett Packard 33120A arbitrary function generator produced the table command signal.

In this study sinusoidal input motion tests were used for validation. A typical sinusoidal input motion is shown in Figure 4.3. The motion was ramped up linearly for 1.5 seconds to insure shaking table stability, followed by full amplitude for duration of 2 seconds, and finally ramped down for 1.5 seconds. Eight different tests were used for validation, the input parameters of the dynamic loading functions are given in Table 4.2.

An inclined steel plane was fitted to the shaking table. The plane inclination was set to 11.37° during the rigid block tests. The steel rigid block was 2.54 cm (1 in.) thick, with area of 25.8 cm^2 (4 in.²), and weight of 1.6 kg (3.5 lbs). Linear accelerometers were fitted on top of

the sliding block and the inclined plane. Displacement transducers measured the relative displacement of the sliding block, and of the shaking table (Fig. 4.4).

A geotextile and a geomembrane were fitted to the face of the sliding block and the inclined plane respectively. The static friction angle (ϕ) of the interface was determined using tilt tests and a value of $\phi = 12.7^{\circ} \pm 0.7^{\circ}$ was reported. Kim et al., (1999) found that the friction angle of the geotextile – geomembrane interface exhibited pronounced strain rate effects, and reported an increase by 20% over one log-cycle of strain rate.

Wartman (2003) showed that the friction angle of the interface was controlled by two factors: 1) amount of displacement; and 2) sliding velocity. The back-calculated friction angle for the range of velocities and displacements measured was between $\phi = 14^{\circ} - 19^{\circ}$ (refer to Fig. 4.5).

The DDA version used in this research accepts a constant value of friction angle. Therefore a single friction angle (ϕ_{av}) value must be chosen for validation. The value of ϕ_{av} was determined as follows. First, the measured displacement of the block was differentiated with respect to time and hence the velocity record was attained. Next, the velocity content for the duration of the test was computed. For example, the test of 2.66 Hz input motion frequency showed that the upper bound velocity was below 10 cm/sec, refer to Figure 4.6a. This value was attained only for short periods of time during the test. The velocity content chart (Fig. 4.6b) shows that 80% of the velocities fall under the value of 3 cm/sec. Taking the value of 3 cm/sec as upper bound, the corresponding friction angle is $\phi_{av} < 17^{\circ}$. The 50% value corresponds to friction angle of $\phi_{av} = 16^{\circ}$. This value was chosen for DDA analysis.

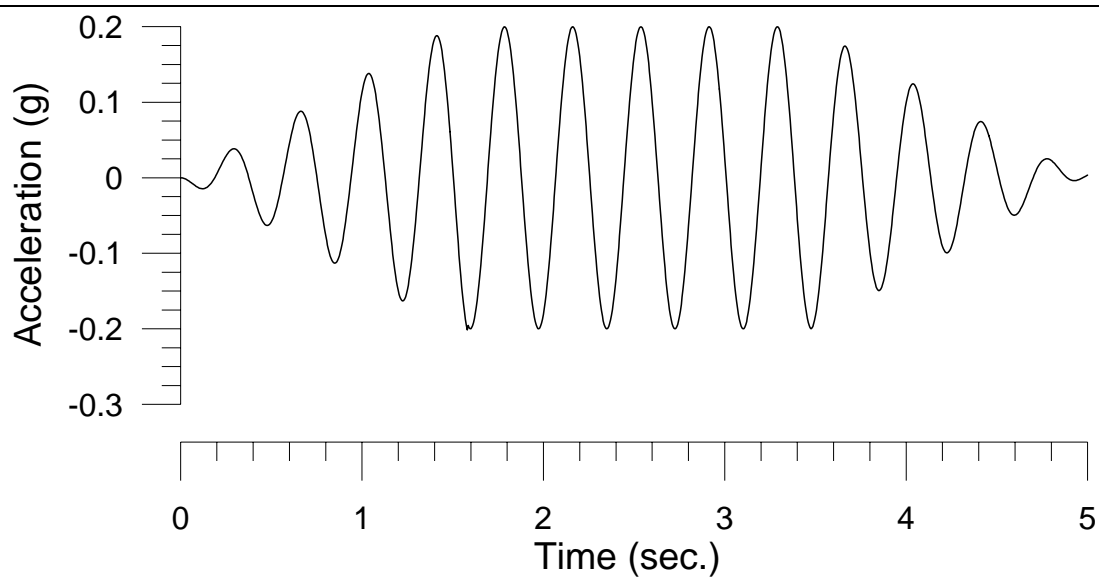
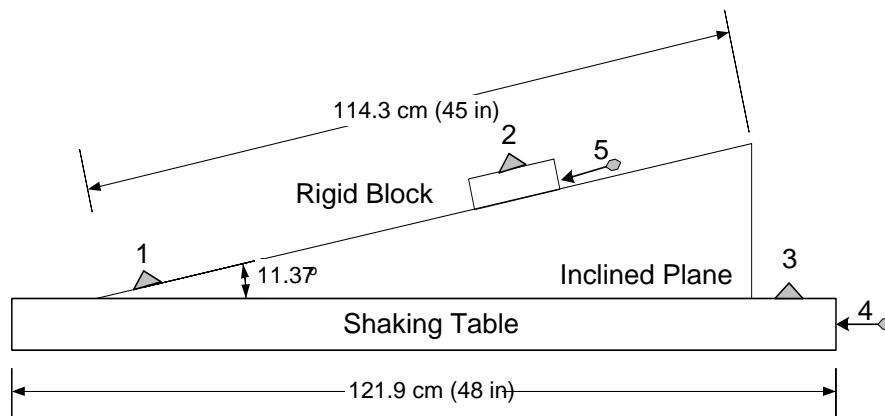
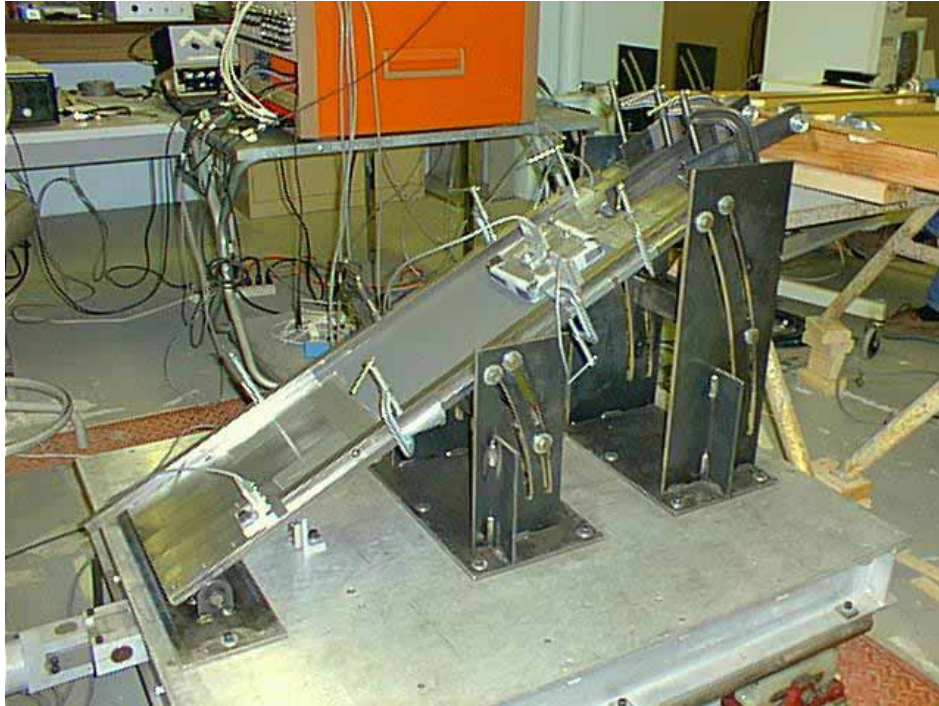


Figure 4.3. Sinusoidal input motion for the shaking table experiment: 2.66 Hz frequency (Test 1 at Table 4.2).

Test	ω (Hz)	d_T (cm)	d_B (cm)	a_h (g)
1	2.66	0.889	5.367	0.28
2	4	0.559	6.604	0.25
3	5.33	0.305	3.341	0.19
4	6	0.254	3.647	0.19
5	6.67	0.254	3.410	0.22
6	7.3	0.228	3.353	0.22
7	8	0.228	3.937	0.23
8	8.66	0.019	2.882	0.21

Table 4.2. Shaking table model summary: ω is the input motion frequency, d_T is the shaking table displacement, d_B is relative block displacement, and a_h is maximum horizontal table acceleration.



No.	Instrument	Direction of Measurement
1	accelerometer	parallel to plane
2	accelerometer	parallel to plane
3	accelerometer	horizontal
4	displacement transducer	horizontal
5	displacement transducer	parallel to plane

Figure 4.4. a) general view of the inclined plane and the sliding block (top); b) sliding block experimental setup and instrumentation location (bottom), from Wartman (1999).

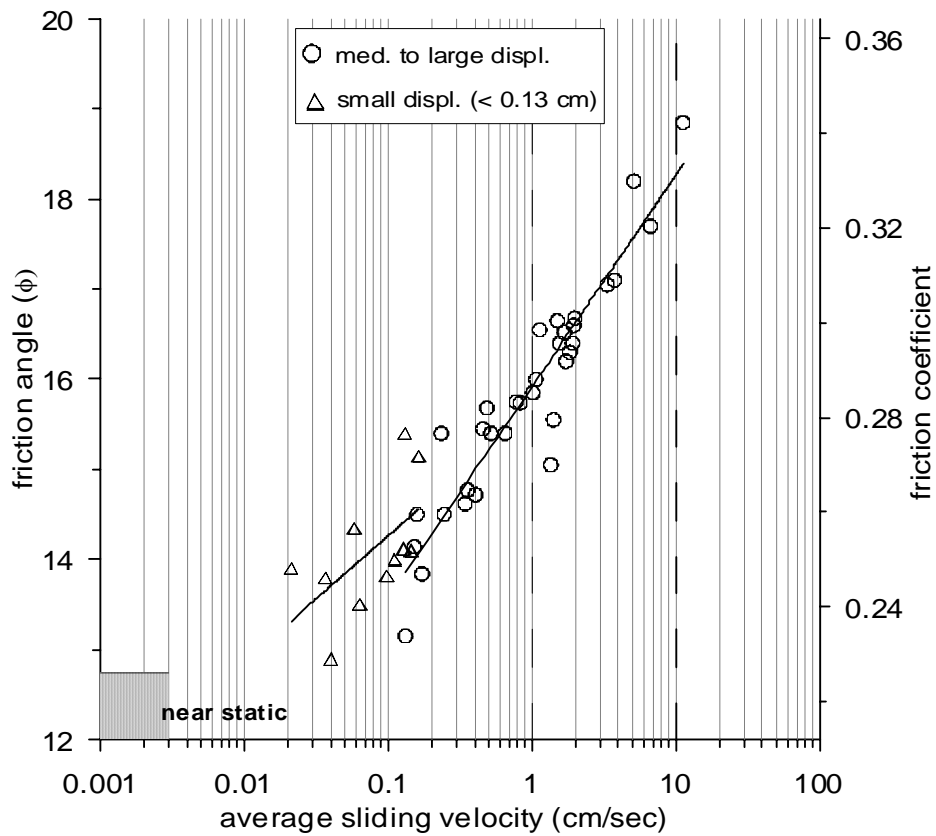


Figure 4.5. Back analyzed friction angles shown as a function of average sliding velocity for rigid block tests, from Wartman (2003).

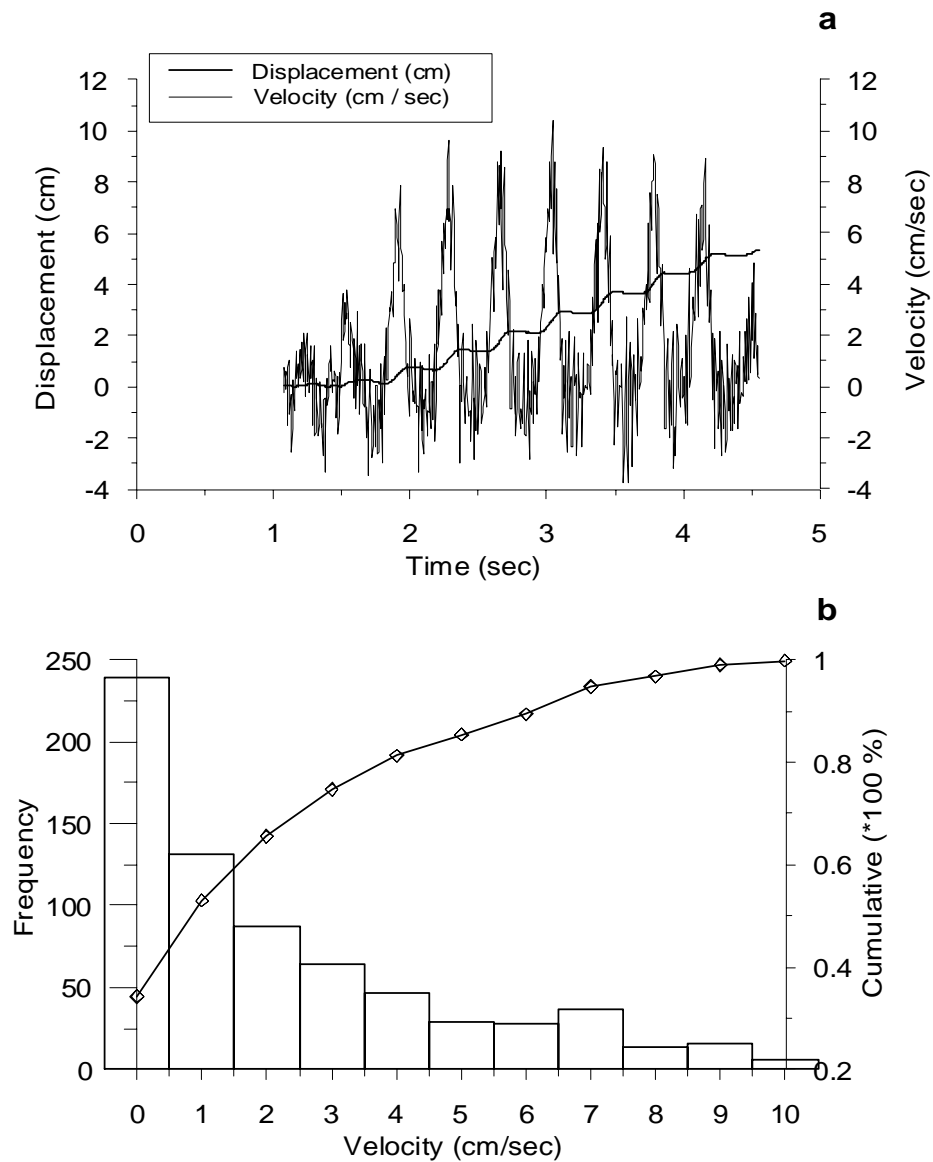


Figure 4.6. The 2.66 Hz sinusoidal input motion test: a) displacement derived velocity; b) velocity content.

4.4. DDA Prediction vs. Shaking Table Results

The numeric control parameters of DDA for this validation study were chosen according to the guide-lines described in previous sections: penalty value $g0 = 5 \cdot 10^9 \text{ N/m}$, time step size $g1 = 0.0025 \text{ sec}$, assumed maximum displacement $g2 = 0.005$.

The 2.66 Hz motion is discussed here in detail and the results are shown in Figure 4.7. Other seven tests yielded similar results, the final displacement errors for this tests are summarized in Figure 4.9. For $\phi_{av} = 16^\circ$ and $k01 = 1$ the numeric error is approximately 80% (Fig. 4.8), but the ultimate displacement values are close, 0.055m measured displacement compared to 0.093m of calculated solution, within the same order of magnitude. Introducing some kinetic damping by reducing $k01$ below 1 improves the agreement between the numerical estimate and physical test data.

Setting $k01 = 0.98$, corresponding to 2% velocity reduction, reduces the error to below 4%, and improves the tracking of the displacement history by DDA. Setting the $k01 = 0.95$ over damps the solution, resulting in a highly un-conservative displacement.

Plotting the numeric difference $e'(\%)$ against input motion frequency (Fig. 4.9) shows that in general DDA accuracy increases with higher frequencies, with an exception at 6 Hz. For $\phi_{av} = 16^\circ$ and $k01 = 1$ the numeric error is always conservative, with the exception of 6 Hz. Reducing $k01$ to 0.98 shows a similar effect for all frequencies, reducing the numeric error below 10%. However, it should be mentioned that setting a constant friction angle for all the analyzed tests introduces an un-conservative error. For input motions with essentially similar peak acceleration, higher frequencies will result in lower block velocity. Given the strain rate dependence of the sliding interface friction, lower velocities correspond to lower friction angles. Thus, the accuracy of DDA could be improved with implementation of rate

dependent friction. This modification is beyond the scope of this study. Using the shaking table results it may be concluded that a kinetic damping value of 2% should be proper for realistic prediction of dynamic displacements.

4.4.1. Accuracy of DDA

The implicit formulation of DDA guaranties numerical stability regardless of time step size. However, it does not guarantee accuracy. Where the time step is too large relative to the numeric spring stiffness, loss of diagonal dominance and/or ill conditioning error may result, interfering with convergence to an accurate solution.

The numeric implementation of DDA utilizes the SOR Gauss – Seidel equation solver. The convergence of the SOR equation solver is guaranteed for diagonally dominant matrices:

$$|K_{ii}| > \left| \sum_j^n K_{ij} \right| \quad i \neq j \quad (4.7)$$

Larger inertia terms on the diagonal of the global stiffness matrix increase the stability of the computation. A small time step size is needed to increase the inertia terms, which are inversely proportional to the square of time step. For small time steps (0.0025 sec) the numeric error does not exceed 10% for increasing penalty values up to $5 \cdot 10^{10}$ N/m; higher penalty values, however, result in significant error as the off diagonal sub-matrices become exceedingly large. Enlarging the time step results in reduction of inertia terms in the diagonal sub-matrices. Therefore, for a given time step size the loss of diagonal dominance will occur at lower penalty values.

Most of the error is accumulated at the beginning of the analysis and it declines with time, a phenomenon known as algorithmic damping (refer to Wang et al., 1996 for elaborate discussion of this phenomenon): typical to the Newmark implicit time integration scheme (Figure 4.10). This behavior is observed here for all selected values of kOI . In this study we

have limited the duration of the analysis to 5 seconds, in conjunction with the duration of the shaking table experiment. Doolin and Sitar (2002) show that for a block on an incline problem the relative error continues to decrease up to displacement of 250 m during 16 seconds of sliding. Therefore, for computations involving larger time spans the error is expected to decline as calculation proceeds, further improving solution accuracy.

When compared with analytical solutions for frictional sliding DDA is found to be accurate. Therefore, it can be assumed that the contact formulation in DDA is equivalent to the mathematical model for frictional sliding. The comparison with shaking table experiments however implies that the contact formulation in DDA is not sufficiently accurate for modeling physical friction. Consider for example the phenomenon of block “wobbling” during shaking table experiments. In the numerical model the acceleration is applied as a concentrated body force at the centroid of each block, whereas in the physical model block displacement is induced by the motion of the shaking table. This motion causes block “wobbling” during which physical contacts may open and close repeatedly. This process reduces the total energy of the system and consequently the total down-slope displacement. Furthermore, the dynamic formulation of DDA is essentially un-damped, friction being the main source of energy consumption. In the physical model however mechanisms such as structural vibrations, material damage along interface (ploughing), drag, heat etc. does take place during block sliding. These processes are not modeled numerically and can be a second source of discrepancy between the results of the numerical and physical models.

The only method available at present to simulate energy dissipation in DDA is by reducing transferred velocity between time steps. In this study it is found that a reduction of transferred velocity by 2% ($k_{OI} = 0.98$) yields realistic prediction of block displacements, further reduction of the dynamic control parameter yields un-conservatively small displacements.

The numeric analyses show good agreement with the shaking table results, once kinetic damping is applied. The reduction of the transferred velocity between time-steps is a numeric adaptation not linked directly to a physical damping mechanism. Since DDA formulation is essentially un-damped, viscous damping is not accounted for. Implementation of a dashpot model in parallel with a contact spring (Voigt model) in order to simulate viscous damping in DDA would be more appropriate. However, it is impossible to assign a correct damping coefficient for the given problem a-priori. For problems of rock falls analyzed using DDA with viscous damping (Chen et al, 1996; Shingi et al, 1997) the selection of the damping coefficient was performed using trial and error procedure. We perform similar best “fitting” by reducing the transferred velocity between time steps.

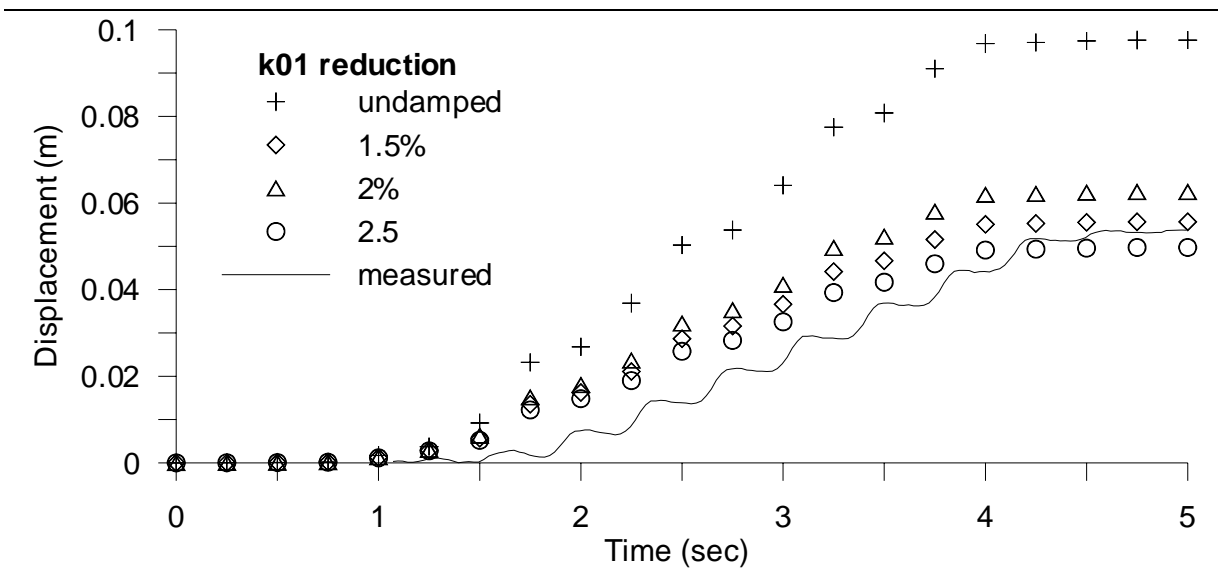


Figure 4.7. The 2.66 Hz input motion: comparison between measured displacement and DDA solutions for different values of inter time step velocity reduction (k_{01}).

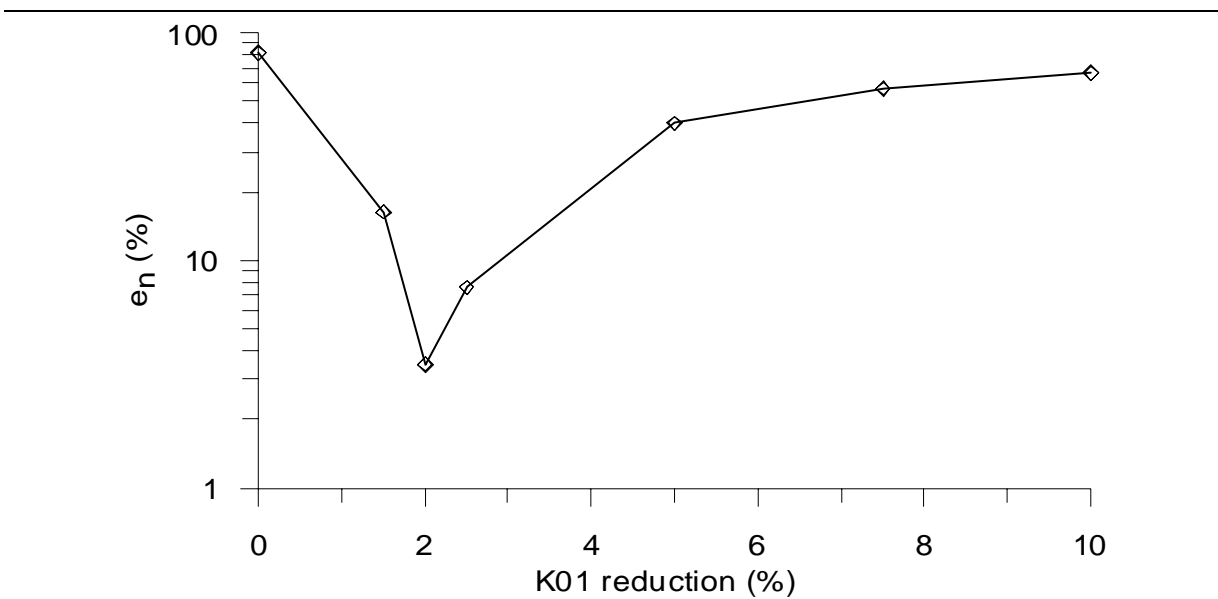


Figure 4.8. The 2.66 Hz input motion: relative numeric error of DDA ultimate displacement as a function of inter time step velocity reduction (k_{01}).

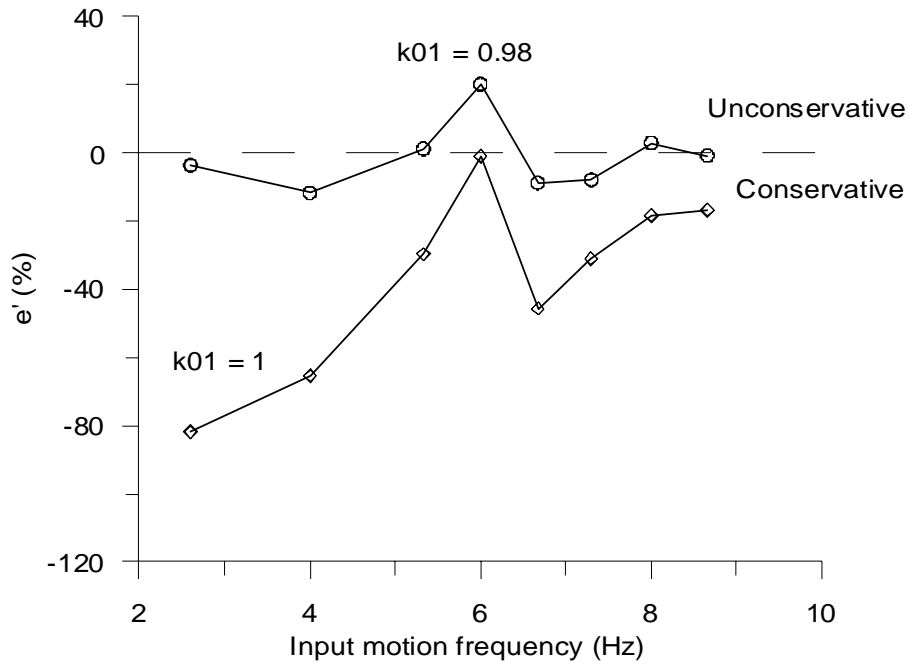


Figure 4.9. Numeric difference of DDA ultimate displacement prediction as a function of input motion frequency.

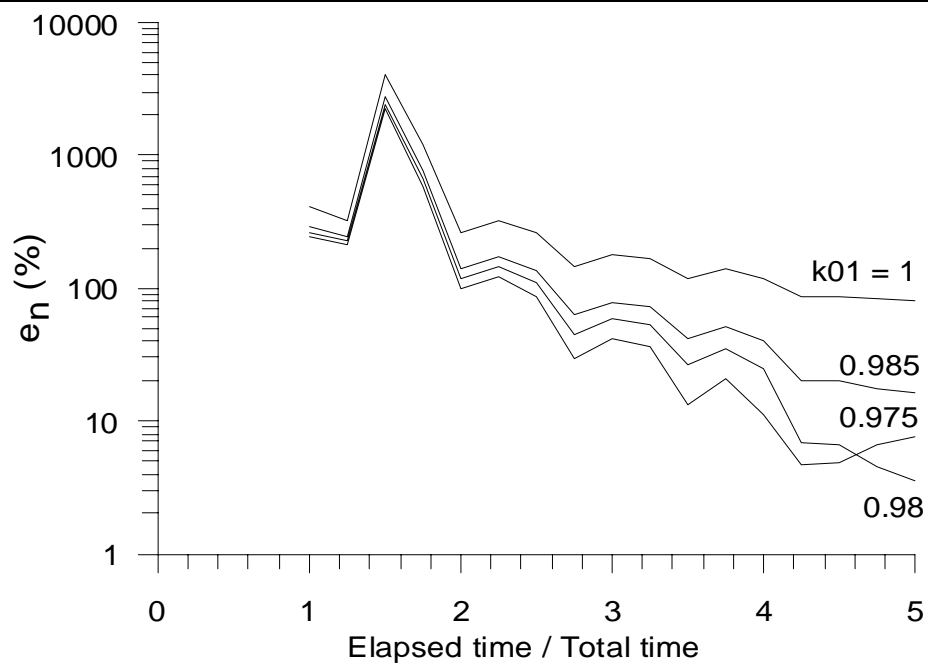


Figure 4.10. The 2.66 Hz input motion: evolution over time of the DDA relative numeric error, for different values of the k_{01} parameter.

4.5. Conclusions

The results of the validation study show that DDA solution of an idealized system for which an analytical solution exists, is accurate. The block contact algorithm in DDA is therefore an accurate replication of the analytical model for frictional sliding.

The accuracy of DDA is governed by the conditioning of the stiffness matrix. The DDA solution is accurate as long the chosen time step is small enough to assure diagonal dominance of the global stiffness matrix.

Comparison between shaking table experiments and DDA calculation shows that the DDA solution is generally conservative, over predicting block displacement. The main sources of discrepancy between DDA and the physical model are the difference between the numerical and actual behavior at contact points, and lack of a complex energy dissipation algorithm in DDA.

For accurate displacement prediction a reduction of the dynamic control parameter (kOI) by 2% is recommended, for the block on a incline problem.

Implementation of viscous damping and strain/displacement dependent friction into DDA can further improve the accuracy of the method.

Chapter 5 – Validation of DDA Using a Centrifuge Model of a Jointed Rock Beam

5.1. Introduction

In the previous chapter, the accuracy of DDA was studied using a shaking table model of a single block on an incline. It was shown that the accuracy of DDA is controlled by the time step size, the contact spring stiffness, and the amount of kinetic damping. During sliding the contacts between blocks, and consequently the stresses within the sliding block remained unchanged. While this behavior is expected in sliding, it is certainly not expected during deformation of a beam consisting of discontinuities. During the deformation of the jointed beam some of the original contacts are expected to be destroyed while new contacts are expected to form; consequently, block stresses are expected to change during ongoing deformation. If DDA is to be applied to such problems, it should be validated using physical model(s) where contacts and stresses are changing during deformation. In this chapter, DDA is validated using centrifuge modeling of a multi-jointed beam.

Centrifuge modeling is based on the assumption of stress similarity. If acceleration of N times earth gravity (g) is applied to a material of density ρ , the vertical stress (σ_v) at depth h_m of the model is given by:

$$\sigma_{v,m} = \rho N g h_m \quad (5.1)$$

In the prototype the vertical stress at depth h_p is:

$$\sigma_{v,p} = \rho g h_p \quad (5.2)$$

Thus for $\sigma_{vm} = \sigma_{vp}$, $Nh_m = h_p$ and the scale factor is N . Since the centrifuge model linearly scales the prototype, the displacements are also at scale factor of N . Strains, however, have a scale factor of 1, and therefore the stress-strain curves in the model and the prototype should be identical. This phenomenon is observed in centrifuge models up to peak strength values. It is not usually possible to create residual shear planes with the same residual strength as the prototype (Taylor, 1995). Talesnick and Hatzor (in prep.) showed that the concept of dimensional scaling in the centrifuge, for situation including rock block interfaces, is not warranted. Therefore, when a centrifuge model is comprised of discontinuous material stress and displacement similarities with the prototype are not guaranteed.

In this research centrifuge modeling was not performed in order to model a specific engineering prototype, but rather to study the essential features of jointed beam deformation, at various g levels.

5.2. Experimental Setting

Centrifuge modeling was performed by Dr. Mark Talesnick of the Department of Geotechnical Engineering, Israel Institute of Technology (Technion). The tests were performed using a beam type centrifuge with beam radius of 1.6 m, maximum payload capacity of 5000kg, and maximum acceleration of 100g at the sample center.

5.2.1. Jointed beam model

The geometry of the model was of a beam made up of six blocks (Figure 5.1). The blocks represent intersection of bedding planes with vertical joints, such as often found in sedimentary rocks. Cubic blocks with edge length of $L = 0.048m$ were cast from gypsum, and the total beam span was $S = 0.288m$. The average block density was $\rho = 998.1 \text{ kg/m}^3$. The

elastic modulus of the blocks, found from uniaxial compression tests, was $E = 3.2 \text{ GPa}$. The friction between blocks was modeled using a 360 grit sand paper, glued to the contact faces of individual blocks. The friction angle of the interface, determined at BGU using tilt test, was $\phi = 35^\circ$.

In order to ensure proper alignment of the blocks with respect to the sidewalls a mechanical system depicted in Figure 5.1 was used. The system included a linear bearing that resisted movements in directions other than the intended. A load cell was integrated into the system in order to allow a specific thrust to be applied during the emplacement of the model. The vertical movements of the block during the tests were recorded using six LVDT's of 0.01mm resolution.

First a pre-stressing of the beam was performed to ensure beam stability at $0g$ level (with reference to centrifuge axis). Then the acceleration was increased in-flight up to the level of $12g$. The beam deformed until stable configuration was attained, at all g levels tested.

5.3. DDA Model

5.3.1. A simple two-block system

Prior to comparison of centrifuge model and DDA results a study of a simple two-block system subjected to gravitational loading was performed. Similar analysis, under somewhat different boundary conditions was performed by Yeung (1991), showing good agreement between the analytical and numerical solutions. In order to simplify the analysis and to preclude vertical (shear) displacements at the abutments the two blocks were constrained by assigning fixed points at base vertices, (Figure 5.3). The aim of this analysis was not to reproduce analytical or semi-analytical solutions, but rather to study the behavior of the DDA solution over time.

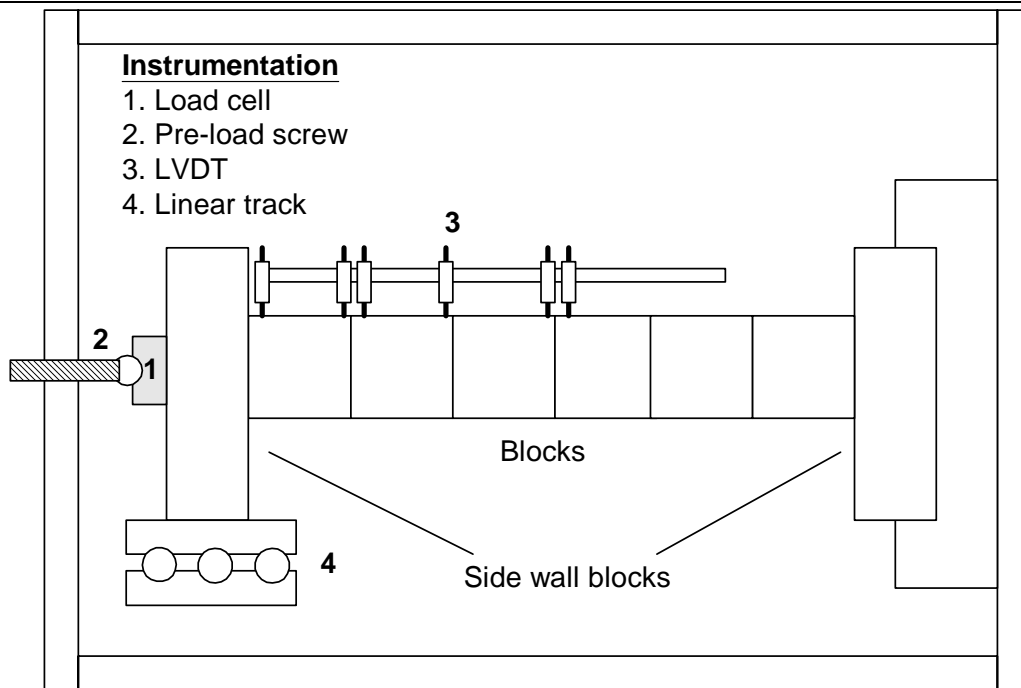


Figure 5.1 Centrifuge model geometry and instrumentation (courtesy of M. Talesnick).

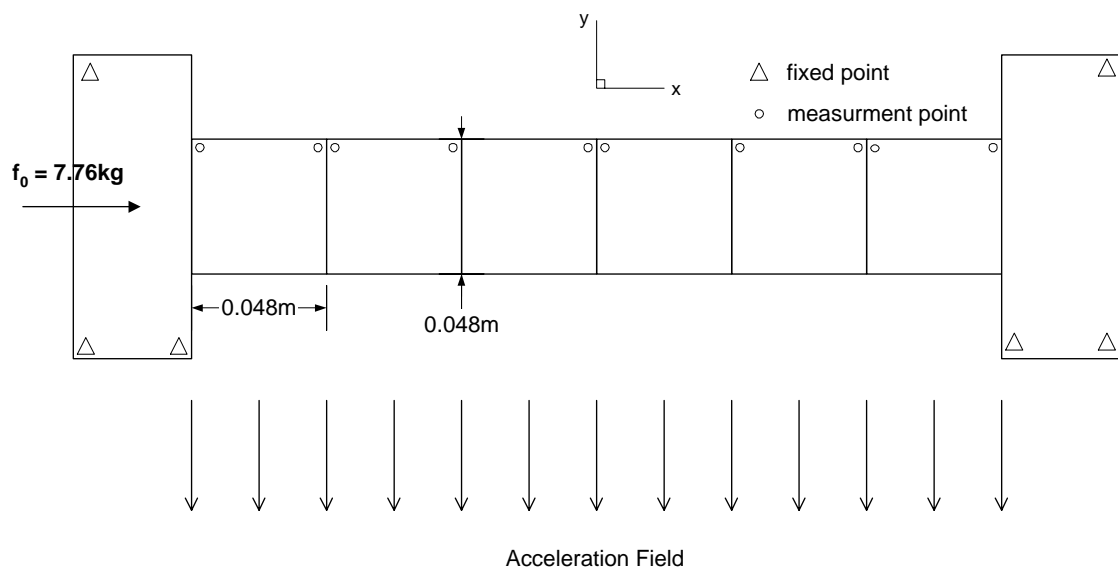


Figure 5.2 DDA model geometry.

DDA analysis was performed for the following material properties: $E = 10 \text{ GPa}$, $\nu = 0.25$, and $\rho = 2.7 \cdot 10^3 \text{ kg/m}^3$. The block dimensions were: $L = 2.5\text{m}$, $t = 0.5\text{m}$. The numerical control parameters are: $g0 = 1 \cdot 10^9 \text{ MN/m}$, $g1 = 0.001 \text{ sec}$, and $g2 = 0.001$. The dynamic control parameter $k01$ was varied during the analysis.

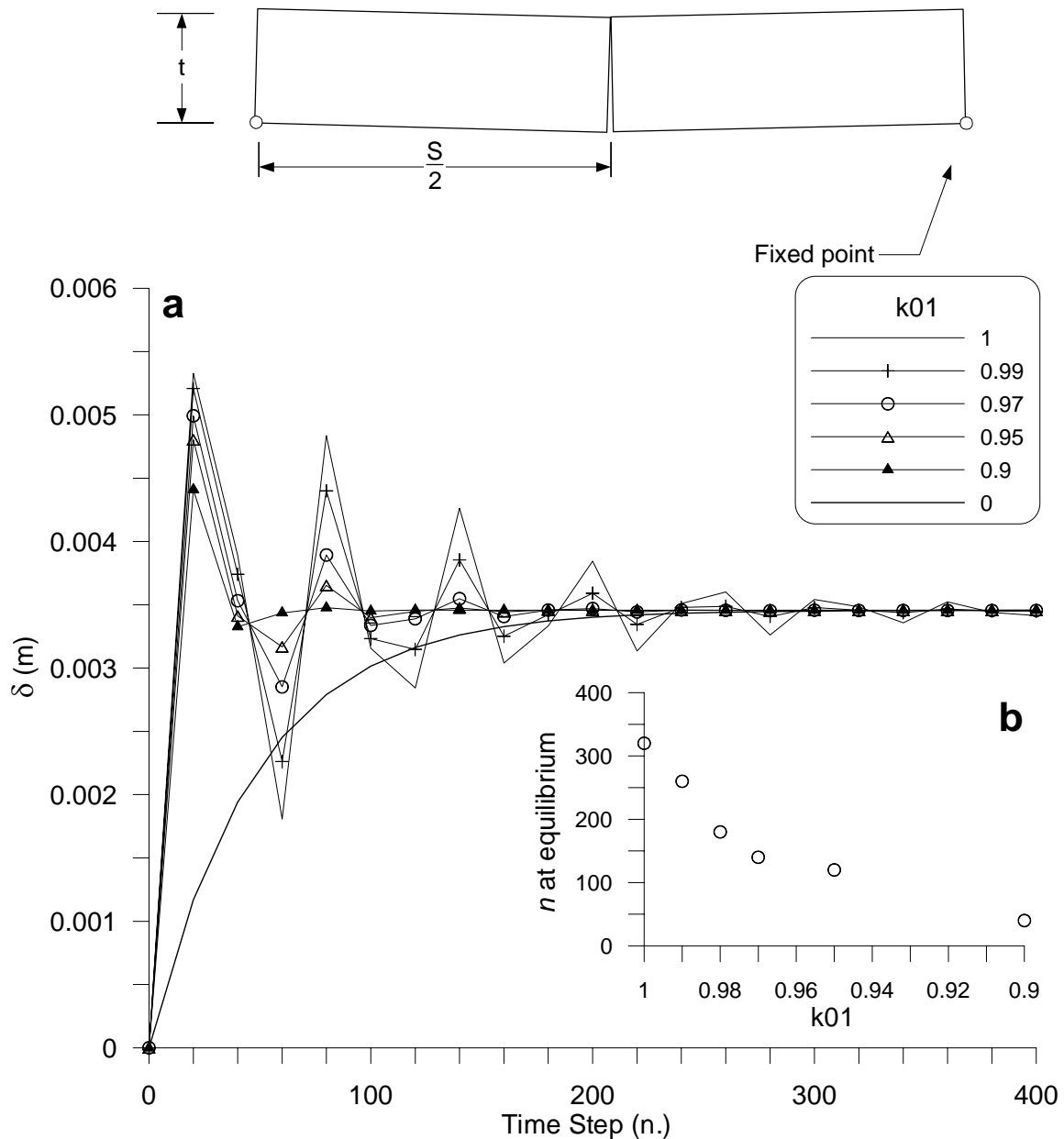


Figure 5.3. DDA model of two block system with fixed base vertices: a) mid-span deflection (δ) as a function of time; b) number of time steps n required to attain equilibrium as a function of the dynamic control parameter ($k01$).

The dynamic behavior of the system is shown in Figure 5.3. The system attained equilibrium position after deflection of $\delta = 0.003455m$. Algorithmic damping is evident, as the initial perturbation, resulting from gravity turn-on, is dissipated with analysis progress. The effect of dynamic “damping” through inter-step velocity reduction (kOI) is apparent. By reducing kOI , the convergence to equilibrium position is enhanced, as the initial perturbation decays with higher rate. For $kOI = 1$ equilibrium was attained after 320 time steps, reducing the inter-step velocity by 1% ($kOI = 0.99$) resulted in equilibrium after 260 time steps. Further reduction of kOI by 5% and 10% resulted in equilibrium after 120 and 40 time steps respectively. This trend is clearly presented in Figure 5.3b.

Setting $kOI = 0$, namely eliminating inter-step velocity transfer, may be interpreted as pseudo-static analysis. Under this condition changes in deflection evolved with time, from initial zero position, until equilibrium solution is met after 240 time steps. Thus, for a system attaining equilibrium, a slightly damped dynamic solution is more efficient numerically.

When analyzing a fully dynamic system the application of kinetic damping should be preformed with care. In cases where the system is to attain equilibrium, or when the mode of failure is independent of geometrical or mechanical constraints (such as in block sliding), the application of kinetic damping is advantageous, since the solution converges rapidly. However, when the mode of failure is determined by the block system geometry or by mechanical properties, the application of kinetic damping is not without flaws. Consider, for example, a single beam with multiple joints, the amount of deflection at mid-span is a function of both joint spacing and friction along joints. Thus, for a beam of a given span but with different joint spacing and friction, application of kinetic damping will not yield the same effect on all solutions.

While for an equilibrating system kinetic damping will enhance the solution, for a non-equilibrating system the solution will tend to retard with respect to the undamped solution.

Furthermore, two solutions of a damped non-equilibrating system are not equable, since the solutions are at different stage of evolution.

5.3.2. A six block model

The initial geometry and boundary conditions in DDA for the jointed beam are given in Figure 5.2. Material properties and friction along interfaces were modeled using the real physical properties. Rigid abutments were modeled by assigning three fixed points to each abutment block. The displacements were measured at 12 measurement points, symmetric with respect to the centerline. Six measurement points were placed conforming to the exact locations of the LVDT's in the centrifuge model. The loading history was replicated in the following manner: first the beam was pre-stressed using the initial value of the centrifuge model, then the g level was changed every 240 time steps by $1g$ increments, up to acceleration level of $12g$, Figure 5.6.

5.3.3. Selection of numerical control parameters

In the previous chapter it was shown that the numeric control parameters are interrelated. Accurate solutions were attained for properly chosen control parameters. Therefore, prior to a comprehensive analysis of the centrifuge model by DDA, an initial sensitivity analysis was performed. The time step size ($g1$), the maximum assumed displacement ($g2$) and the dynamic control parameter ($k01$) were set to 0.0005 sec, 0.001 and 1 respectively. The contact stiffness between blocks ($g0$) was changed over three orders of magnitude, from $g0 = 10 \text{ MN/m}$ to $g0 = 1000 \text{ MN/m}$, and the displacements and stresses were studied. The sensitivity analysis was performed at a loading level of $1g$.

The results of the sensitivity study are presented in Figures 5.4a,b, and c. Figure 5.4a is a plot of the vertical displacement profile, Figure 5.4b is a plot of the horizontal stress (σ_{xx}) at the block centroids, and Figure 5.4c is the time history of beam deformation. Figure 5.4a

clearly shows that for low contact stiffness of $g0 = 10 \text{ MN/m}$, the vertical movement of the beam is excessive, with respect to the measured displacement (bold line). Furthermore, from the deformation profile it is evident that the beam shears along abutments, as a single intact beam. The extremely low stresses within the blocks confirm that arching (transfer of vertical load to the abutments) within the beam is inactive, thus confirming the previous observation. Increasing the contact stiffness to $g0 = 100 \text{ MN/m}$ reduces the vertical displacement, and shows better stress prediction, however, the vertical displacements are still excessive, and the stresses are low. Increasing the contact stiffness to $g0 = 250 \text{ MN/m}$ improves the stress prediction, the displacements however are similar to those of $g0 = 100 \text{ MN/m}$. The deformation profile reveals that for both $g0 = 100 \text{ MN/m}$ and $g0 = 250 \text{ MN/m}$ the displacement attains a maximum at the center of the beam and a minimum at the abutments, implying that a mechanism of arching is active. The deformation is symmetric with respect to the beam centerline.

Clearly, the amount of DDA predicted displacement, especially at the abutments, is large with respect to the measured displacement. This discrepancy can be attributed to the following factors:

1. Constant strain/stress elements (simply deformable blocks) – preclude the development of stress concentrations within the blocks, and therefore of true compressive arching, thus leading to increased displacements.
2. Representation of frictional interface – in the centrifuge model the frictional interfaces, two facing sheets of sand-paper, are not infinitely thin, but rather consists of a deformable element with a given thickness. In DDA the discontinuity interface is infinitely thin, allowing only sliding or separation.

3. Rotational freedom – while the DDA model geometry can be regarded as densely packed, the centrifuge model exhibits higher rotational freedom, due to the nature of the frictional interfaces.

The rotation of the blocks during deformation in DDA is not evident, as opposed to the rotations recorded in the centrifuge model. However, both centrifuge model and DDA predict stability of the jointed beam after small amounts of deflection, through a build up of stresses.

For high contact stiffness, $g_0 \geq 500 \text{ MN/m}$, the deformation profile shows unrealistic behavior, loss of symmetry, and relative upward motion of blocks. For $g_0 = 500 \text{ MN/m}$ the stresses are accurate, whereas for $g_0 = 1000 \text{ MN/m}$ the stresses are excessively high.

Time histories (Figure 5.4c) reveal that for all values of contact stiffness the beam attains equilibrium position. The number of time steps until equilibrium is reached is smaller for higher values of contact stiffness. Similar effect was shown by the simple two-block example of Chapter 3. For $g_0 \geq 500 \text{ MN/m}$ equilibrium is attained after 60 time steps, whereas for $g_0 \leq 250 \text{ MN/m}$ equilibrium is attained after 220 time steps.

Examination of the iteration time history (Figure 5.5) reveals that for contact stiffness of $g_0 \leq 250 \text{ MN/m}$ the DDA solution converges after approximately 240 time steps, where the number of iterations per time step drops from $i = 6-8$ to $i = 1$. For $g_0 \geq 500 \text{ MN/m}$ the convergence of DDA solution is enhanced, and $i = 1$ is achieved after 60 to 80 time steps. However, the number of iterations per time step before equilibrium is higher for high contact stiffness, as high as $i \leq 10$, compared to $i \leq 8$ for lower values. The transition from a large number of iterations per time step to a value of $i = 1$ is regarded here as a convergence criterion.

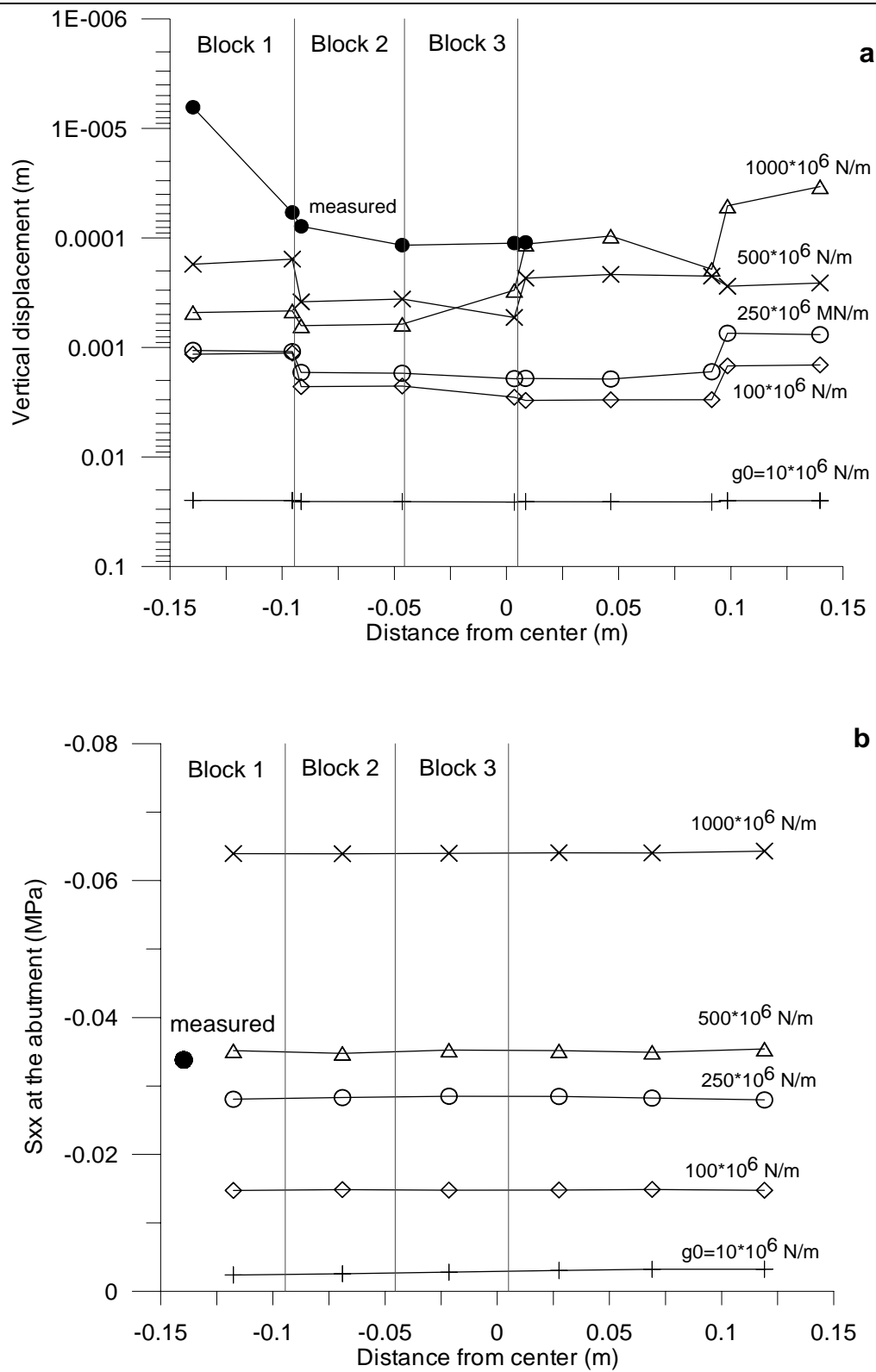


Figure 5.4. Contact stiffness sensitivity analysis for the DDA six block model: a) vertical displacements; b) horizontal stresses within the blocks..

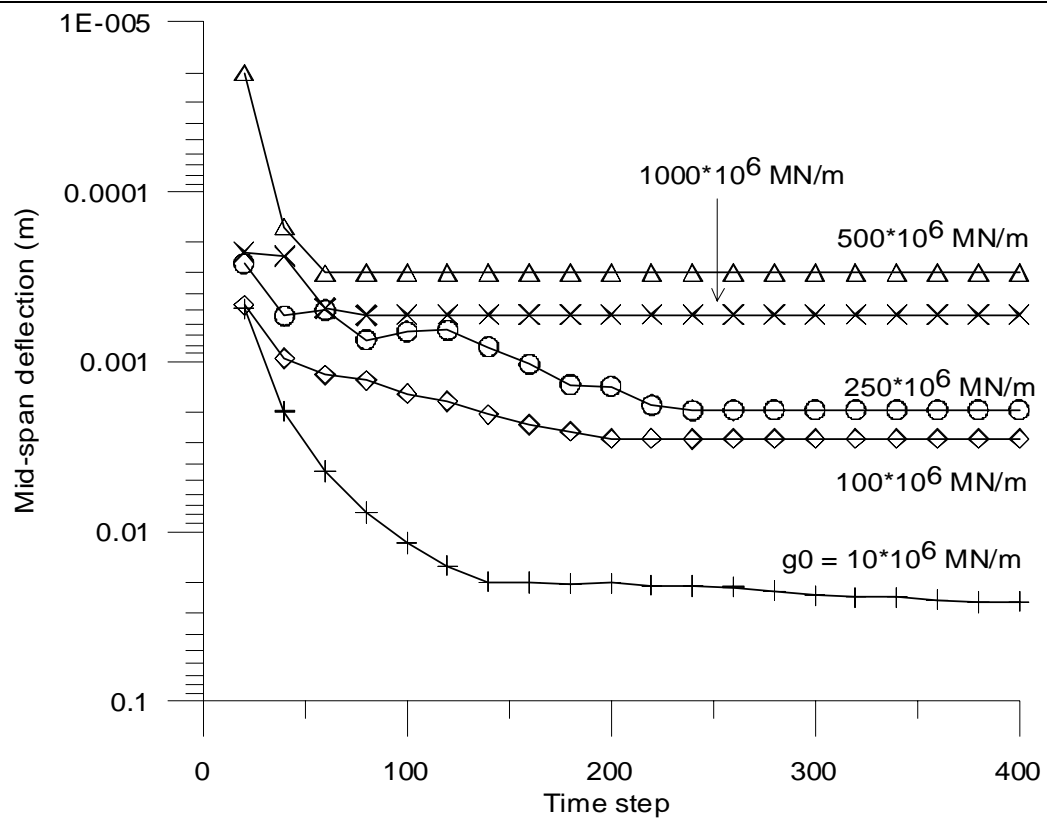


Figure 5.4 (cont.). Contact stiffness sensitivity analysis for the DDA six block model: c) time histories.

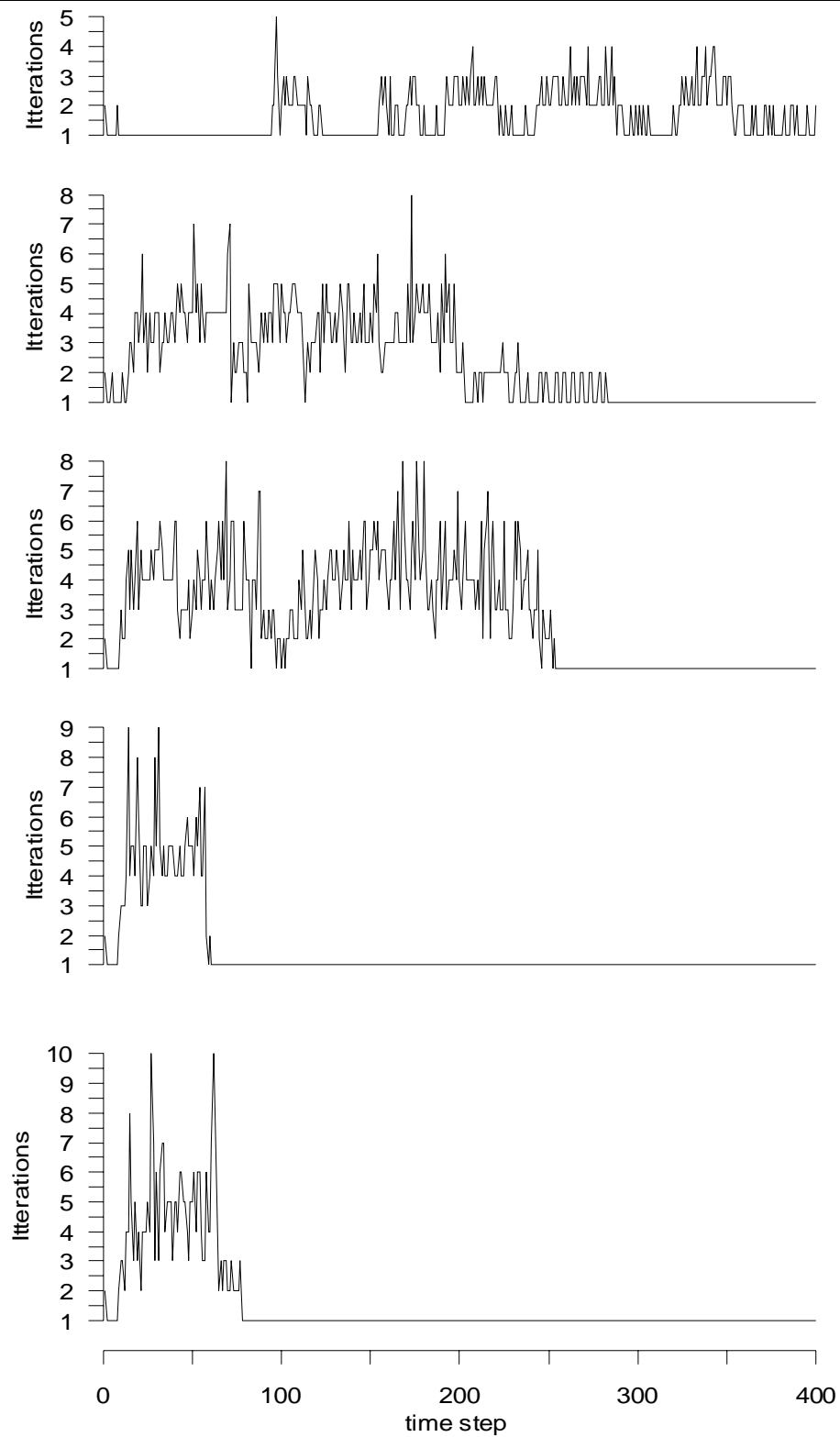


Figure 5.5. Iteration history for the DDA six block model for different values of contact stiffness.

From the discussion above it is concluded that for the given beam geometry and material properties, a contact stiffness value of $g_0 = 250 \text{ MN/m}$ yields the most accurate values with respect to displacement, stresses, and convergence of the numeric solution. This value is used in the DDA simulation of the centrifuge model for a jointed beam.

The DDA model is divided into 12 segments of loading, from $1g$ to $12g$ in $1g$ increments, each of 240 time steps, conforming to the convergence criterion described earlier. DDA loading function of the centrifuge model is depicted in Figure 5.6. The numerical control parameters and material properties for the DDA model are given in Table 5.1.

5.3.4. Results

The results of DDA are presented in Figure 5.7a and 5.7b that show vertical displacements and stresses respectively. Clearly, the amount of displacement predicted by DDA is excessive when compared with the displacements measured in the centrifuge model. However, the deformation features are similar: most of the displacements are found at the center of the beam, dying out towards the abutment. Thus, active arching within the deforming beam can be assumed.

For loading levels of $a > 4g$, the displacements are very similar, implying stable arching of the beam. In Figure 5.7b, the horizontal stresses are growing with the g level, suggesting that arching stresses are building up within the beam. Furthermore, the angle to principal stresses (θ) within the blocks is growing with g level, as shown in Figure 5.8. For loading levels of $a > 7g$ the variation of angle θ shows distinct arching: the principal stresses left of the centerline are rotated in a positive sense (counter-clockwise), whereas the principal stresses on the right hand side are rotated in a negative sense (clockwise). The magnitude of the measured and DDA computed stresses are found to be of the same order; the relative numeric error is 30% to 60% for all loading levels concerned.

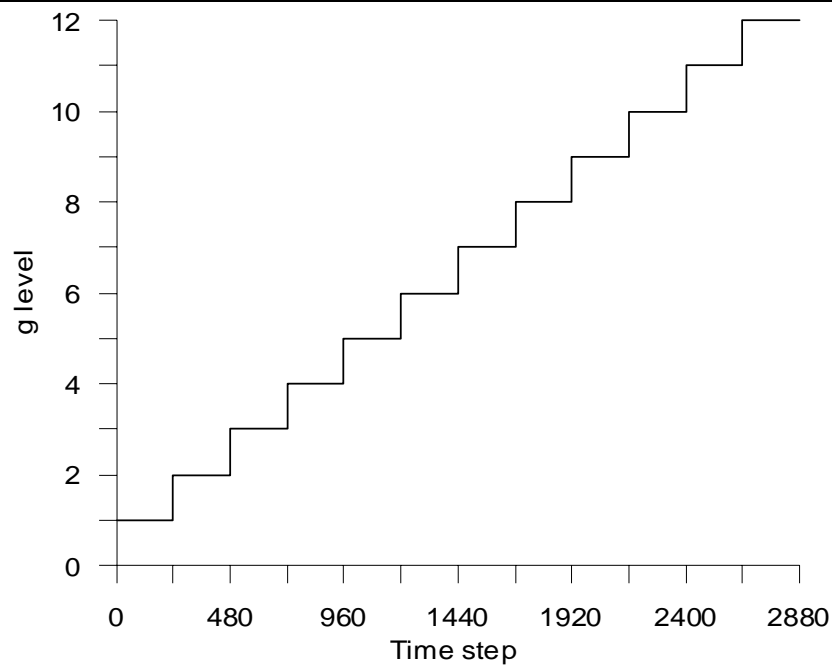


Figure 5.6. DDA six block model loading function.

Density	998 kg/m ³
Elastic Modulus	3200 MPa
Poisson's ratio	0.25
ϕ	35°
Penalty stiffness ($g0$)	250 MN/m
Time step size ($g1$)	0.0005 sec
Penetration control parameter ($g2$)	0.001
Dynamic control parameter ($k01$)	1

Table 5.1. Material properties and numeric control parameters for the DDA six block model.

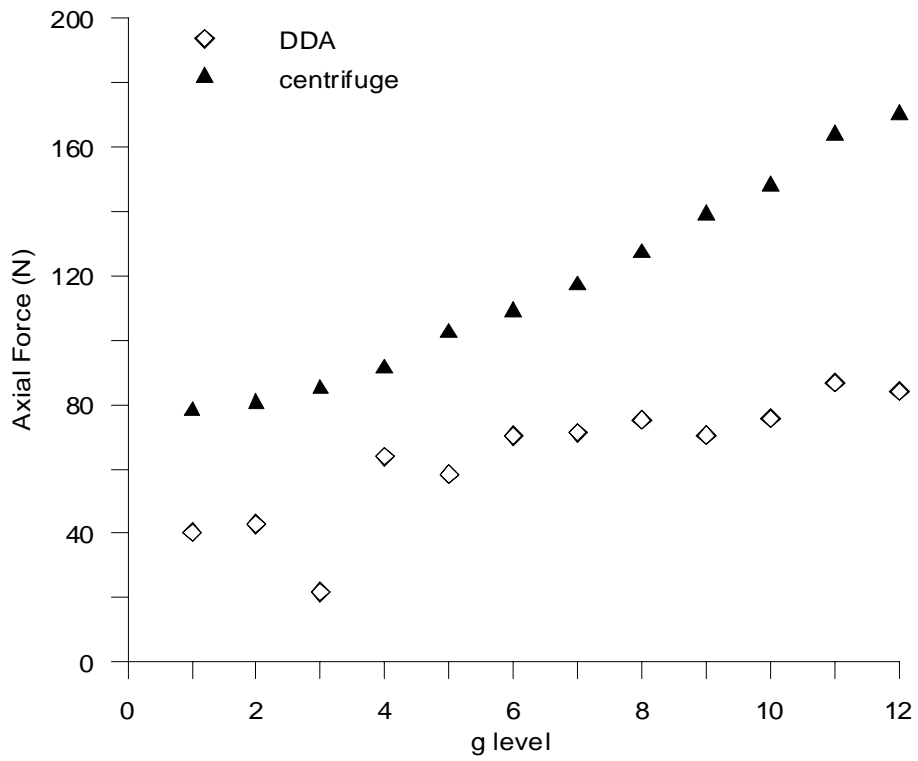
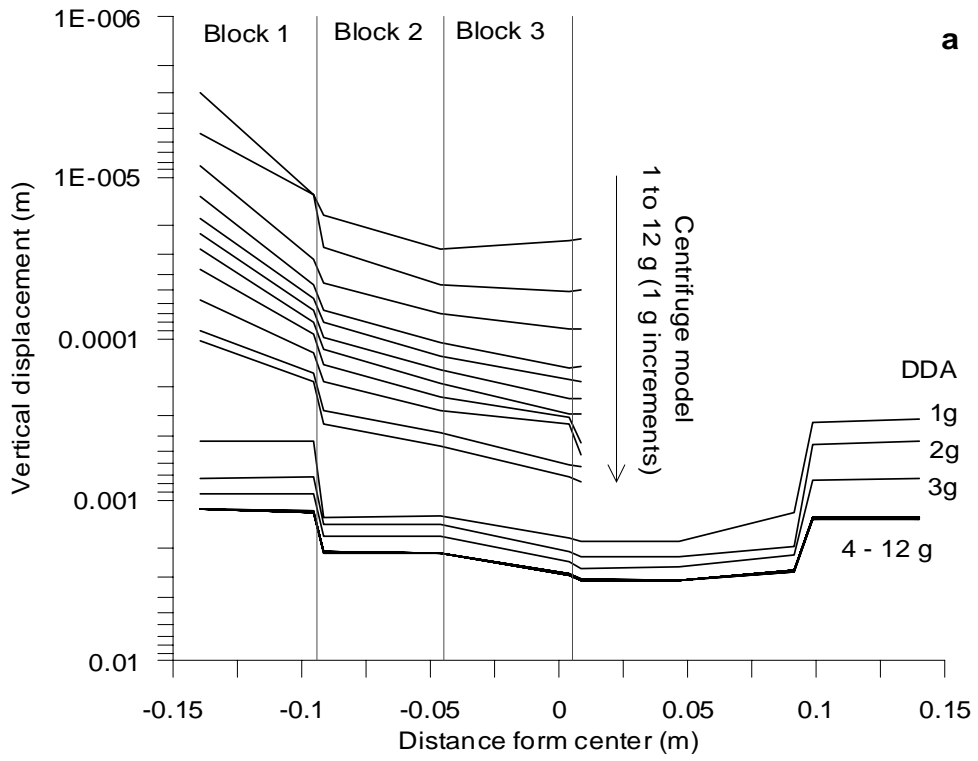


Figure 5.7. Comparison between centrifuge model results and DDA solution: a) vertical displacements; b) horizontal stresses.

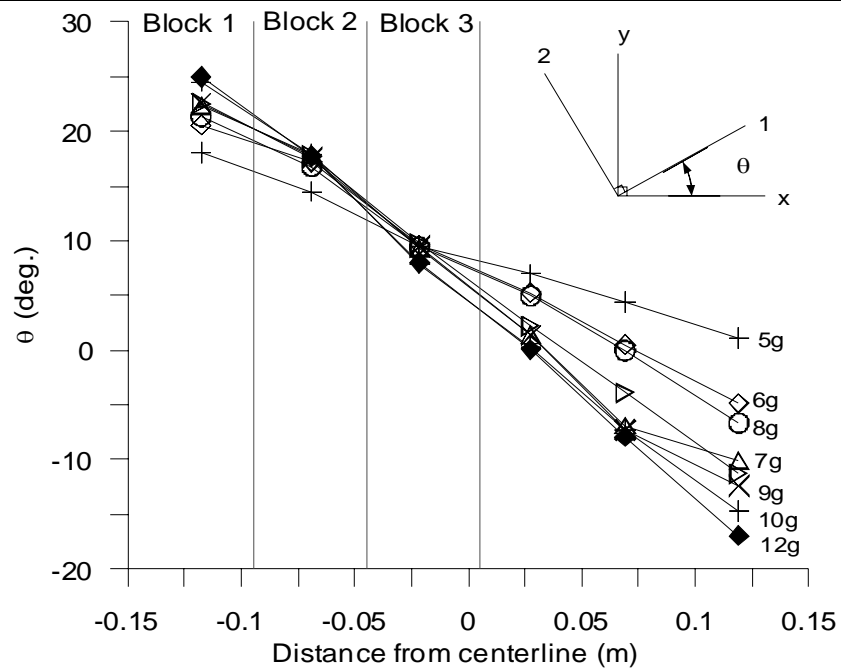


Figure 5.8. DDA six block model: angle to principal stresses (θ) within the blocks

5.4. Discussion and Conclusions

From the discussion above, it can be concluded that DDA captures the essential features of the jointed beam deformation, as found in the centrifuge model. Both centrifuge model and DDA show that an arching mechanism, transfer of vertical load to the abutments, is active within the beam. Arching precludes displacement of blocks near the abutment, and induces stability after initial displacement. This is clearly seen at high loading levels, where the principal stresses are rotated in a symmetric pattern with respect to the centerline, as shown in Figure 5.8.

However, the exact magnitude of displacements and stresses are not replicated by DDA. The discrepancies between the centrifuge model and the DDA solution arise from the following factors:

1. Representation of joints in DDA and centrifuge model.
2. First order displacement approximation in DDA.

These factors are described in section 5.3.3.

The geometric dimensions of the centrifuge model poses additional difficulties. The individual blocks are very small and tightly packed, and deformations are extremely small, maximum of $10^{-5}m$ under low loading levels. The initial perturbation associated with application of gravity is not fully dissipated through the analysis, and the numeric error remains high throughout the analysis. Furthermore, since joints exhibit intrinsic plastic behavior, similarity between the model and full size engineering prototypes is not guaranteed.

When compared with the classic Voussoir mode, DDA shows a distinct advantage. For the given geometry, Voussoir model predicts failure at loading level of $1g$. The beam buckles without achieving equilibrium.

In DDA the mode of failure, displacements and stresses are governed by the value of contact stiffness. The magnitude of the contact stiffness is purely numeric, and it is not associated with normal or shear stiffness of physical interfaces. The choice of the contact stiffness value should be made according to numeric criteria, such that correct mode of failure and numeric convergence are achieved.

Chapter 6 – The Tel Beer-Sheva Case Study

6.1. Introduction

Successful validation of numerical models by closed form solutions for simple problems, or by comparison to small-scale physical models is essential. However, no analytical solution or laboratory model can duplicate the scale and character of the loading, boundary and environmental conditions inherent to full-scale problems. Rock masses are heterogeneous with respect to their mechanical properties, with complex boundary conditions. Furthermore, in discontinuous rock masses the spatial arrangement of the discontinuities is complex, and in times only partially attainable. Comparison of numerical predictions to actual behavior in well-documented case studies can help insure that extrapolation from simple problems to field scale problems is basically valid.

Case studies used for the validation of a DEM should comply with the following requirements: (1) a well-defined geometry and boundary conditions; (2) accurately determined material properties of the continuous rock; (3) accurately determined spatial distribution of discontinuities and the mechanical properties of discontinuities. The case study of Tel Beer-Sheva meets these requirements.

The case of Tel Beer-Sheva was previously studied by Benary (1996) and Hatzor and Benary (1998). Their research showed that: 1) the classic Voussoir model is unconservative for the given rock mass structure; and 2) the stability of a laminated Voussoir beam is dictated by the interplay between friction angle along joints and joint spacing.

In this study several issues are explored in greater depth: the mechanical properties of the rock mass are further explored: transverse isotropy of the continuous rock is defined and the mechanical properties of the discontinuities are studied using direct shear apparatus.

The numerical part of this study is performed under the guidelines developed in Chapters 4 and 5. The numerical study emphasizes the kinematics and deformation of both a single layer and multi-layered roof, with comparison to the classic Voussoir solution.

6.2. Site Description

The ancient site of Tel Beer-Sheva is located approximately 3 km southeast of the modern city of Beer Sheva. Situated on a hilltop at elevation of 307 m MSL, the site is bordered by two ephemeral streams (wadi): Wadi Beer-Sheva (south) and Wadi Hebron (north). The ancient city of Beer-Sheva is dated to the Iron age at 2700 B.P to 3200 B.P. The ancient water reservoir, dated to 3000 B.P., was used as a water storage facility for times of drought or siege. A schematic layout of the archeological site and the underlying water reservoir is presented in Figure 6.1.

The large storage facility beneath the city was fed by seasonal run-offs from Wadi Hebron, through a tunnel running beneath the city walls. From within the city the access to the water tank was through a large vertical shaft. The intake capacity of the reservoir, disregarding support elements, is approximately 250 m³. The walls of the reservoir were plastered to prevent leakage.

The excavation sequence of the water reservoir is unknown. However, evidence of failure within the period of excavation, or short time after, is found in the form of a large support pillars coated with the same plaster. The water reservoir layout is presented in Figure 6.2. The main hall of the reservoir is a rectangle 14 m long and 15 m wide. An elongated room, 7m long and 3 m wide extruds from the main hall. Two pillars, found at the center of

the main hall, support the roof at areas where failure occurred. The morphology of the failure zones and their relation to the support pillars are described in section 6.2.2.

6.2.1. *Geology*

Tel Beer-Sheva is located in an elevated area bordering two major synclinal structures the Beer-Sheva syncline (south) and the Shefela syncline (north). The water reservoir is excavated in the sedimentary Gareb formation (Upper Cretaceous), comprised of alteration of horizontal layers of chalk 0.3m to 0.8m thick, with some thinner (up to 0.1m) layers of marly chalk of low plasticity and swelling potential (Benary, 1996).

Gareb formation is unconformably overlaid by the polymictic Ahuzam conglomerate (Upper Pliocene), locally attaining thickness of up to 6 m, containing cemented, poorly sorted, angular to rounded pebbles of limestone and chert. Overlying the Ahuzam conglomerate are Quaternary riverbed deposits, mixed with archeological layers, locally attaining thickness of 3 m.

6.2.2. *Geometrical properties of discontinuities and failure zone morphology*

An extensive mapping of joint sets at the site was performed by Benary (1996). The following section summarizes the main findings by Benary. The joints were mapped both within the underground water reservoir and a nearby outcrop (within 300 m) exposed by Wadi Beer-Sheva. Three vertical joint sets were mapped. The geometrical properties of the joint sets are given in Table 6.1.

Joint sets J1 and J2 are most abundant with mean spacing of 0.2m and 0.25m respectively. The bedding planes are horizontal with mean spacing of 0.5m. The strike of joint set J1 is nearly parallel to the axis of the intake tunnel, while J2 is perpendicular to J1 and co-linear with the reservoir walls. The intersection of the closely spaced joints with the bedding planes forms a dense network of mostly equidimensional cubic blocks.

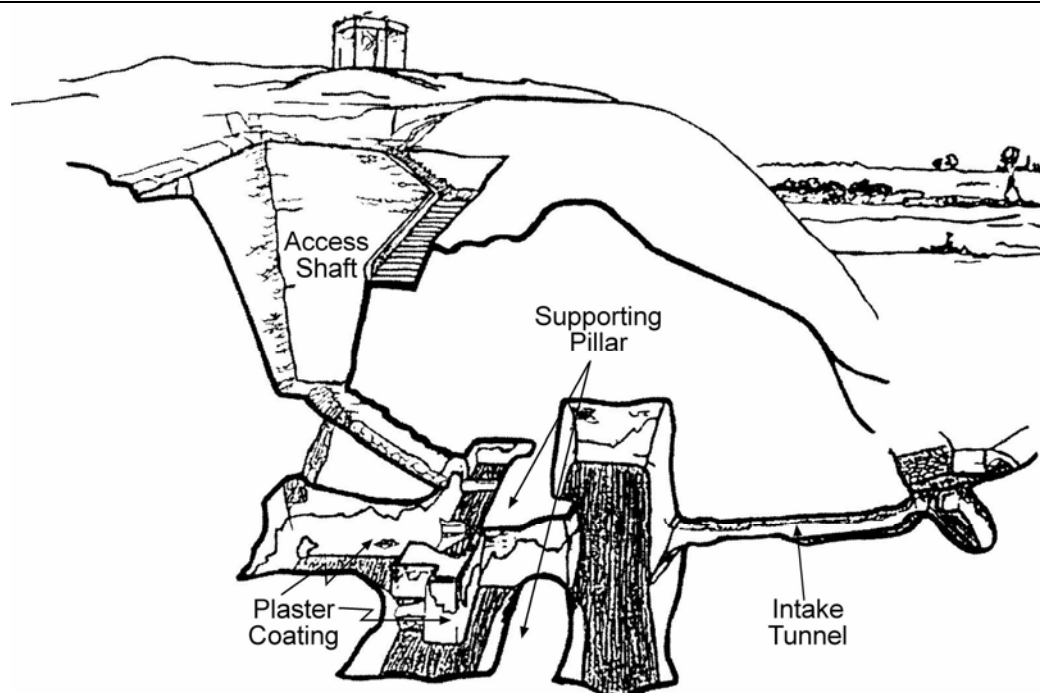


Figure 6.1. Schematic drawing of the Tel Beer-Sheva archeological site and the water reservoir. (Source: Hatzor and Benari, 1998).

The excavation of the water reservoir, and consequent stress release, led to spatial rearrangement of the initial tight packing, where most movement occurred along the pre-existing joints.

Joint set	Dip	Strike (°)	Mean Spacing (m)	Persistence (m)
J1	Sub-vertical	039 – 061	0.2	>10
J2	Sub-vertical	124 – 127	0.25	Bounded by J1*
J3	Vertical	107 – 112	0.6	>15
Bedding	Horizontal		0.5	Infinite

Table 6.1. Principal joint sets in the Gareb chalk at Tel Beer-Sheva site, from Benary (1996).

The roof of the water reservoir collapsed into a shape of a three dimensional dome.

Three distinct levels were mapped by Benary (1996):

- Original excavation level at absolute level of 286 m – Zone 1.
- Intermediate failure level at absolute level of 287 m – Zone 2.
- Upper failure level at absolute level of 289 m – Zone 3.

All zones are developed along natural bedding planes. The transition between the different levels ranges from vertical to step like, running along block boundaries, defined by the intersections of joints and bedding planes. Longitudinal and transverse cross sections are presented in Figure 6.3a,b respectively.

The western pillar supports the roof at Zone 3. The lateral extent of the pillar is unknown due to plaster coating. However, given the fact that the pillar supports the uppermost failure zone, the minimum extent is within the boundaries of Zone 3. Furthermore, lining extends beyond the boundaries of Zone 3 into Zone 2, where the host rock is exposed. The exposure of rock mass at the extreme end of the western pillar is found to be in line with the external wall of the access shaft. Based on these observations the minimum extent of the western pillar is drawn (dashed line at Figure 6.2). The eastern pillar supports Zone 2, and does not attain Zone 3. Again, the lateral extent is not clear. However, based on similar considerations the extent of the pillar is drawn. Plaster coating of the reservoir walls is confined to Zone 1 level, and original chisel marks are found only at Zone 1.

Based on all previously described observations the assumed minimum active span of the opening at the time of failure was 8 meters, conforming with Zone 3. The assumed maximum active span, drawn at Figure 6.2, was 10 meters conforming to Zone 2.

6.3. Mechanical Properties of Intact Rock

6.3.1. Experimental procedure

Intact rock samples were tested using hydraulic, closed-loop, servo-controlled, triaxial load frame (TerraTek system model FX-S-33090) with stiffness of 5×10^9 N/m. Axial and radial strains were recorded using four arm axial and radial strain cantilever sets with 10% and 7% strain range respectively, both with 1% linearity full scale. Total axial load capacity in compression was 1400 kN, but the applied axial load was limited by the load cell capacity. In this research we used a 222 kN load cell, with over range capacity of 100%, and 0.5% linearity full scale, for better resolution of low loads. Axial stroke capacity was 113.78mm. All tests were performed under a constant strain rate of 10^{-5} s^{-1} ; and complete stress-strain curves were obtained.

Solid cylinders were prepared according to ASTM standards (D4543-85 and D2216-92) regarding end roughness (0.01 mm) and perpendicularity (0.005 radians). Uniaxial tests were performed according to ASTM standard D3148-93. The cylinder axes were oriented parallel to bedding planes (the angle between the normal to bedding planes and maximum principal stress σ_1 is $\beta = 90^\circ$).

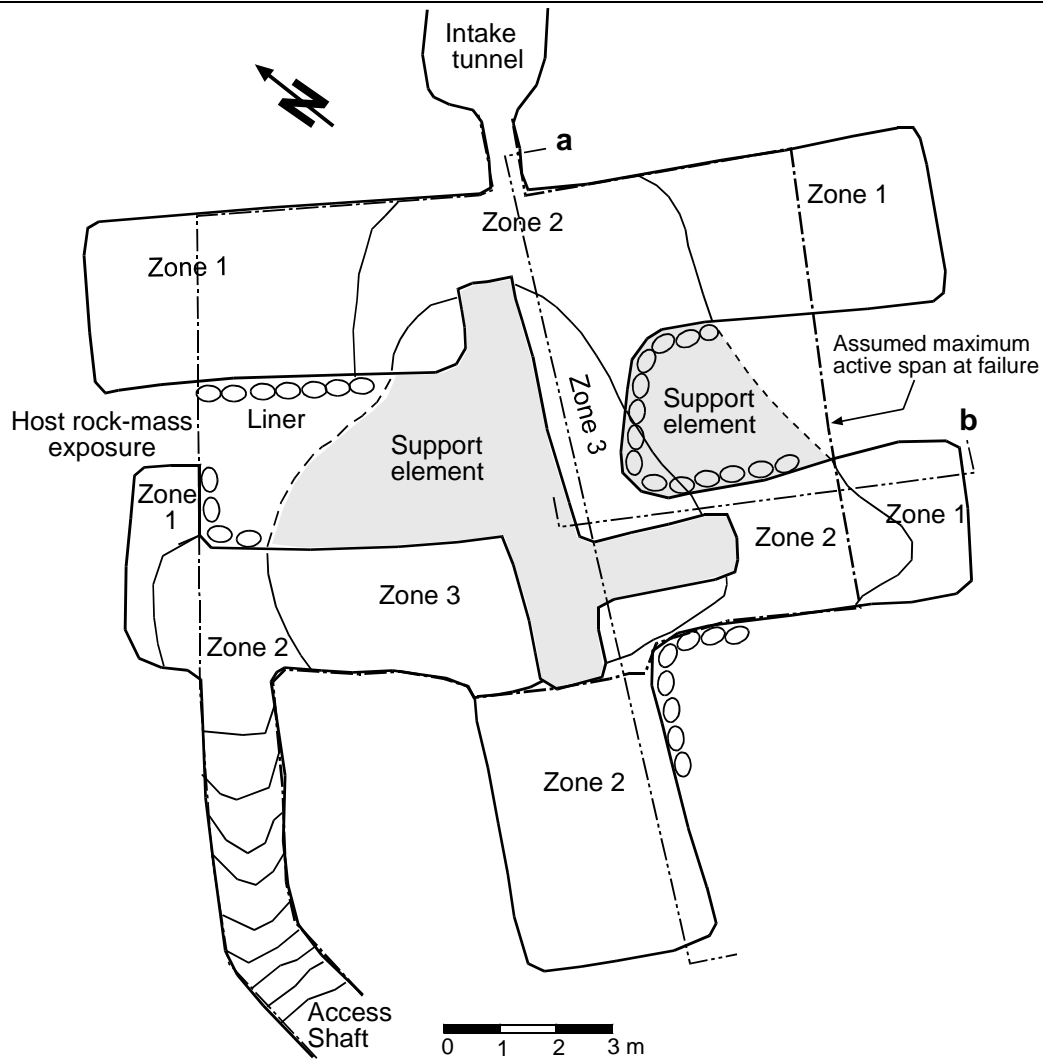


Figure 6.2 General layout and failure zone mapping of the water reservoir, after Benary (1996). Cross-sections *a* and *b* are presented in Figures 6.3a and 6.3b respectively.

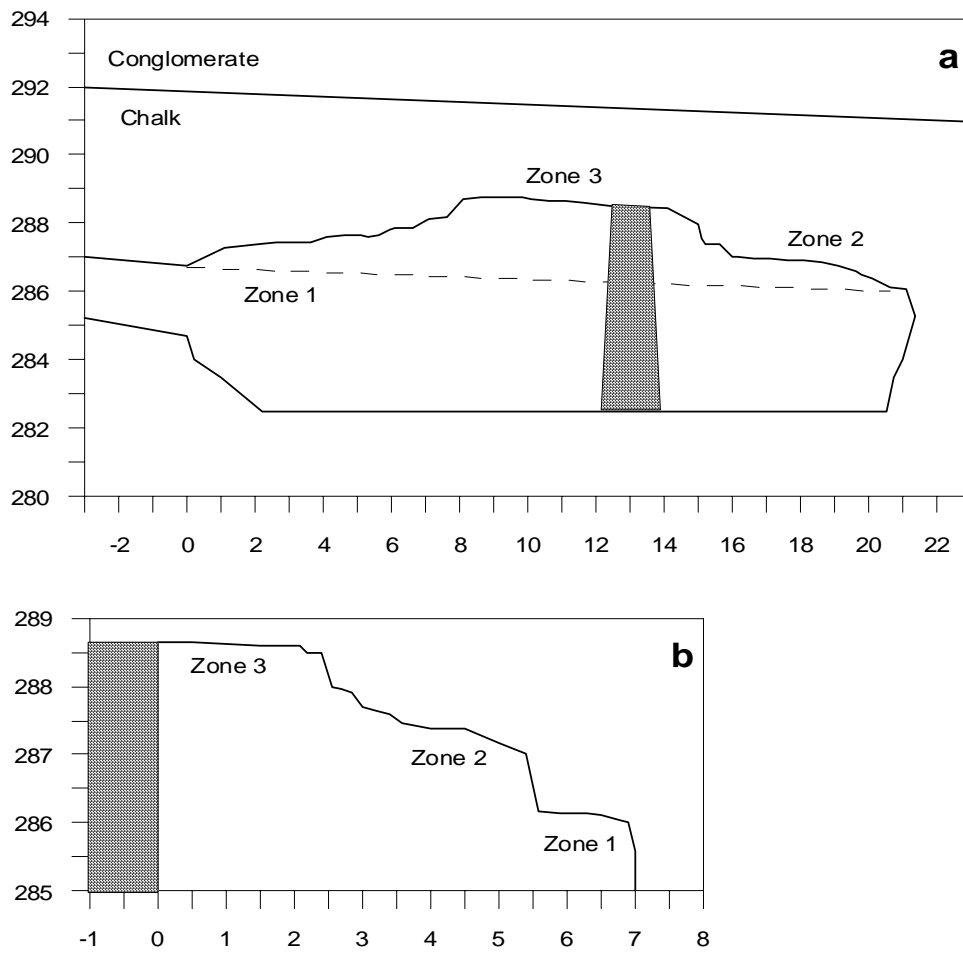


Figure 6.3. Cross-sections of the water reservoir: a) longitudinal cross-section; b) transverse cross-section (Source: Benari, 1996).

The tested samples were drilled from two blocks extracted from two overlaying beds in a natural riverbed outcrop below the archeological site of Tel Beer-Sheva, where the level of exposure is approximately at the level of the water reservoir.

Benary (1996) performed both uniaxial and triaxial tests oriented normally to bedding planes (i.e. $\beta = 0^\circ$), on samples taken from two vertical cores which penetrated the reservoir beds.

6.3.2. Test results

Four samples were tested here under uniaxial compression, the mechanical properties of which are summarised in Table 6.2. Two representative stress-strain curves for uniaxial compression at $\beta = 90^\circ$ and $\beta = 0^\circ$ are shown in Figure 6.4. The variation in the mechanical properties between samples TBS-1 and TBS-2 can be attributed to local variations as described in the previous section.

Gareb chalks exhibit pronounced anisotropy both in strength and in elasticity. The uniaxial compressive strength ratio ($UCS_{\beta=90^\circ} / UCS_{\beta=0^\circ}$) varies from 3 to 5, and the elastic modulus ratio ($E_{\beta=90^\circ} / E_{\beta=0^\circ}$) is varies from 3 to 4. Transverse isotropy parallel to bedding planes is assumed: in three tests the radial strains ($\varepsilon_{R1} \perp \varepsilon_{R2}$ and aligned parallel to beddings) exhibit essentially identical behavior, with inter-strain linear coefficient ranging from 0.98 to 1.1.

6.3.3. Estimation of the in-situ stresses

Based on these findings the in-situ stresses can be estimated. The vertical stress is assumed gravitational, given by $\sigma_v = \rho g z$ where z is depth. The ratio of horizontal to vertical stresses $k = \sigma_h / \sigma_v$, may be estimated using the elasto-static thermal model of Sheorey (1994):

$$k = 0.25 + 7E_h \left(0.001 + \frac{1}{z} \right) \quad (6.1)$$

where z (m) is depth below surface and E_h (in GPa) is the average deformation modulus measured in the horizontal direction. This direction of measurement is important particularly in layered sedimentary rocks, in which the deformation modulus may be significantly different in different directions. For the case of Tel Beer-Sheva $E_h = 7.485 \text{ GPa}$

A direct measurement of the in-situ horizontal stress was not performed in this research. However, hydraulic fracturing measurements by Polishook (1995), at a site located about 15 km southwest from Tel Beer-Sheva at depths of 52-70 meters show good agreement with Sheorey's model (refer to Figure 6.5). The measurements were performed on younger Eocene strata (Adulam formation), composed mainly of horizontally layered thick chalk, within the Beer Sheva syncline. Good agreement between the measured and calculated values supports the applicability of the model, and precludes significant contribution from overlooked tectonic stresses.

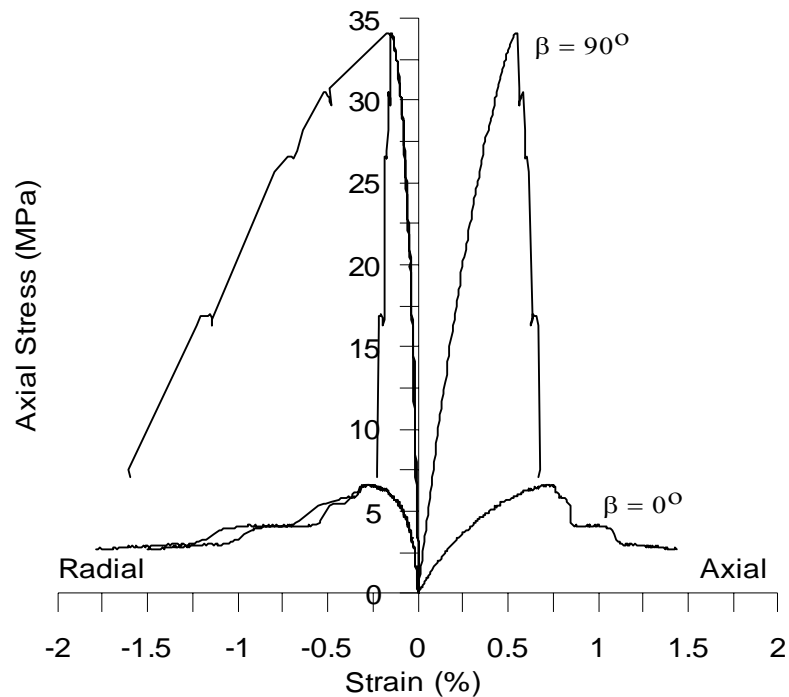


Figure 6.4 Complete stress-strain curves for the Gareb chalk at uniaxial compression parallel ($\beta=90^\circ$, this study) and normal to bedding ($\beta=0^\circ$, Benari, 1996).

Sample	β ($^\circ$)	ρ (kg/m^3)	n (%)	E (GPa)	ν (%)	UCS (MPa)
TBS-1a	90	1930	28	8.34	0.172	34.12
TBS-1b	90	1960	27	8.16	0.160	29.35
TBS-2a	90	1880	30	6.94	0.164	25.08
TBS-2b	90	1850	31	6.50	0.190	21.78
Benary (1996)	0	1910*	29*	1.9	0.05	6.6

* average value.

Table 6.2. Mechanical properties of the Gareb chalk at Tel Beer-Sheva. ρ is density, n is porosity (calculated for $G.S. = 2.7$), ν is Poisson's ratio, E is elastic modulus, and UCS is unconfined compressive strength.

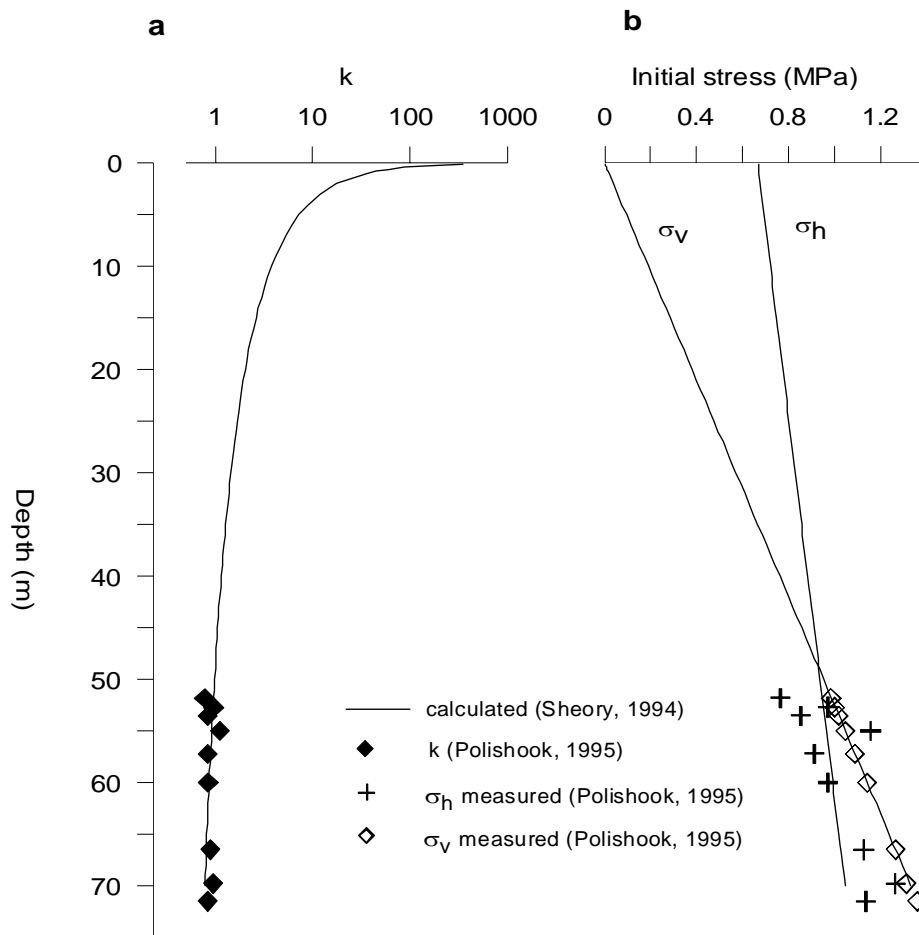


Figure 6.5. a) Calculated and measured stress ratio k at the Beer-Sheva syncline; b) horizontal and vertical stresses at the Beer-Sheva syncline.

6.4. Mechanical Properties of Discontinuities

6.4.1. Direct Shear testing apparatus and sample preparation

The mechanical properties of the discontinuities were tested using a direct shear system manufactured by TerraTek, a servo controlled test system built of two load frames combined to act simultaneously (Figure 6.6):

- Normal load frame: a 4-column fixed platen with a stiffness of 7.0 MN/m. Axial load capacity in compression was 1000 kN. The load cell capacity was 1000 kN, with over range capacity of 100%, and 0.5% linearity full scale.
- Shear load frame: a 4-column fixed platen with a stiffness of 3.5 MN/m. Horizontal load capacity was 300 kN. Horizontal stroke capacity was 102mm. The load cell capacity was 300 kN, with over range capacity of 100%, and 0.5% linearity full scale.

Joint displacement was monitored by 6 LVDTs, 4 for normal displacement and 2 for shear displacement, with 50 mm range and 0.25% linearity full scale. The LVDT's were fitted to the still frames encapsulating the sample, thus accurately capturing the joint displacement. The shear box size was 170 mm × 170 mm × 340mm capable of accepting samples of size up to 150 mm × 150 mm × 300mm.

The samples were cemented into the shear box using Portland 350 cement, such that the surface of the joint coincided with the plane of shearing, and a gap of approximately 1cm was left unbonded between the upper and lower boxes. Natural joints were sampled in the field, at the research site. Polished surfaces were attained by saw cutting continuous chalk blocks. The saw-cut surfaces were polished twice: large asperities were reduced using a

Silicon Carbide grit 120 polishing powder; final leveling was attained using Silicon Carbide grit 300 polishing powder.

6.4.2. Direct shear tests of natural joint

Two-segment tests were performed on TBS-1, both performed under constant displacement rate (shear rate of 0.00127 mm/sec). The joint was tested as sampled without any additional treatment. Normal load was increased between the segments to obtain a failure envelope. Test TBS-1 was performed under normal loads of 0.7 MPa; 1.7 MPa; 3.7 MPa. Test TBS-1A was performed under normal loads of 2.95 MPa; 4.95 MPa and 6.95 MPa. The results are presented in Figure 6.7a, and the variation of resulting friction angle as a function of normal stress is given in Figure 6.7b. Peak friction angle under the specified loading condition was $\phi = 47^\circ$ (at $\sigma_n = 700$ kPa, not shown in Figure 6.7a), the friction angle was reduced during the test down to a value of $\phi = 24^\circ$. Degradation of the friction angle as a function of increasing normal stress represents the degradation of the asperities along the joint surface. Thus, the peak friction angle is $\phi_p = 47^\circ$ and the residual friction angle is $\phi_r = 24^\circ$, the maximum roughness angle is $i = \phi_p - \phi_r = 23^\circ$.

6.4.3. Shear rate effect – polished interface

In order to attain better understanding of artifacts associated with shear rate a single polished surface was tested under varying rate conditions. Sample TBS-2 was subjected to three cycles of shearing under different shear rates: 0.0033 mm/sec, 0.0127 mm/sec and 0.0254 mm/sec. The normal stress was set constant for all three tests at 3150 kPa. Results of the test are given in Figure 6.8. Friction angle for the three cycles is practically the same, $\phi = 29^\circ$ for forward shear and $\phi = 25^\circ$ for backward shear. The shear stiffness, given in Figure

6.8b, shows a pronounced strain rate effect. The strain rate and shear stiffness are inversely proportional: with lower shear rate resulting in higher stiffness.

The nature of the shearing process is changed as well during the increase of shear rate. For low shear rate, 0.0033 mm/sec, shearing is clearly of stick slip type with shear stress amplitude variation of approximately ± 100 kPa. With increased shear rate the amplitude of the stick slip oscillations is reduced to approximately ± 30 kPa. Further increase in shear rate reduced the oscillations to values lower than ± 10 kPa. It is unclear whether this is a shear rate effect, or roughness degradation due to cyclic shearing. Constant value of friction angle during the consecutive shearing cycles implies that roughness is negligible.

6.4.4. Direct shear tests of a polished interface

Sample TBS-4, a polished surface, was tested under various normal loading conditions. Normal stress levels were: 500 kPa, 1000 kPa, 1500 kPa, and 2000 kPa. The shear rate was set constant at 0.0254 mm/sec. Shear displacement – shear stress curves for sample TBS – 4 are given in Figure 6.9a. The shear stiffness values showed proportional increase with the increase in normal stress (Fig 6.9b), as expected. Friction angles during shearing cycles show pronounced anisotropy. During forward shear the friction angles reduced from $\phi = 47^\circ$ at $\sigma_n = 500$ kPa to $\phi = 38^\circ$ at $\sigma_n = 2000$ kPa (Fig 6.9c). For backward shear the friction angles rose from $\phi = 30^\circ$ at $\sigma_n = 500$ kPa to $\phi = 35^\circ$ at $\sigma_n = 2000$ kPa.

Dilatancy data and visual examination of the sample revealed that friction anisotropy is related to accumulation of crushed material (bulge) along the shear interface during the first cycle. The geometry of the bulge was such that during forward shear the relative motion between the mating surfaces led to vertical contraction, while backward shear led to vertical dilation. The bulge was mechanically reduced during the consecutive cycles of shear. The difference between the forward – backward friction angles decreased, from 14° at $\sigma_n = 500$

kPa to 2° at $\sigma_n = 2000$ kPa. Friction angle value converged to $\phi = 35^\circ$ at $\sigma_n = 2000$ kPa. Friction angle for a polished chalk surface as measured at sample TBS – 2 is $\phi = 25^\circ - 29^\circ$. The differences between these two values represent the residual geometry and shear strength of the bulge. Such a phenomenon can occur in natural environments when shear initiates along discontinuities in weak rock. Crushing of intact rock material in the vicinity of discontinuity can cause an accumulation of rock material along the shear surface, thus significantly contributing to shear resistance along the sliding plane.

Direct shear tests for this research were performed under constant normal stress (CNS). This configuration is less suitable for underground applications where shear sliding of blocks is usually constrained between joints, and therefore best represented by constant normal position (CNP) tests. The friction angle attained from CNS tests is usually lower than one attained from CNP tests. However, the deformation of the jointed beams is such that both position and normal stresses are changed during deflection. Therefore, neither CNP nor CNS tests are truthful replica of the shear processes active in jointed beam deformation.

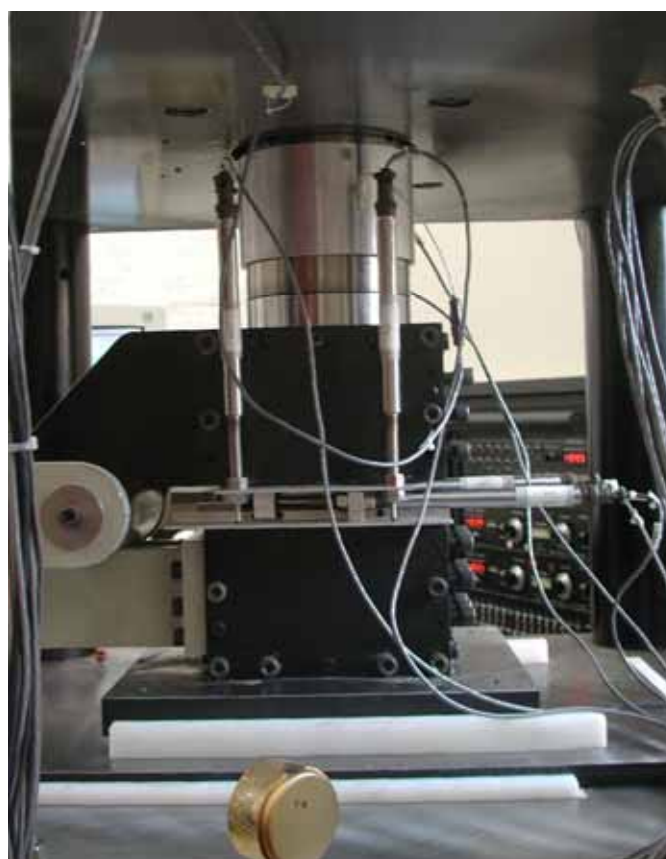


Figure 6.6. Direct shear system at the Rock Mechanics Laboratory of the Negev: a) general view; b) assembled shear box and displacement detectors (LVDT's).

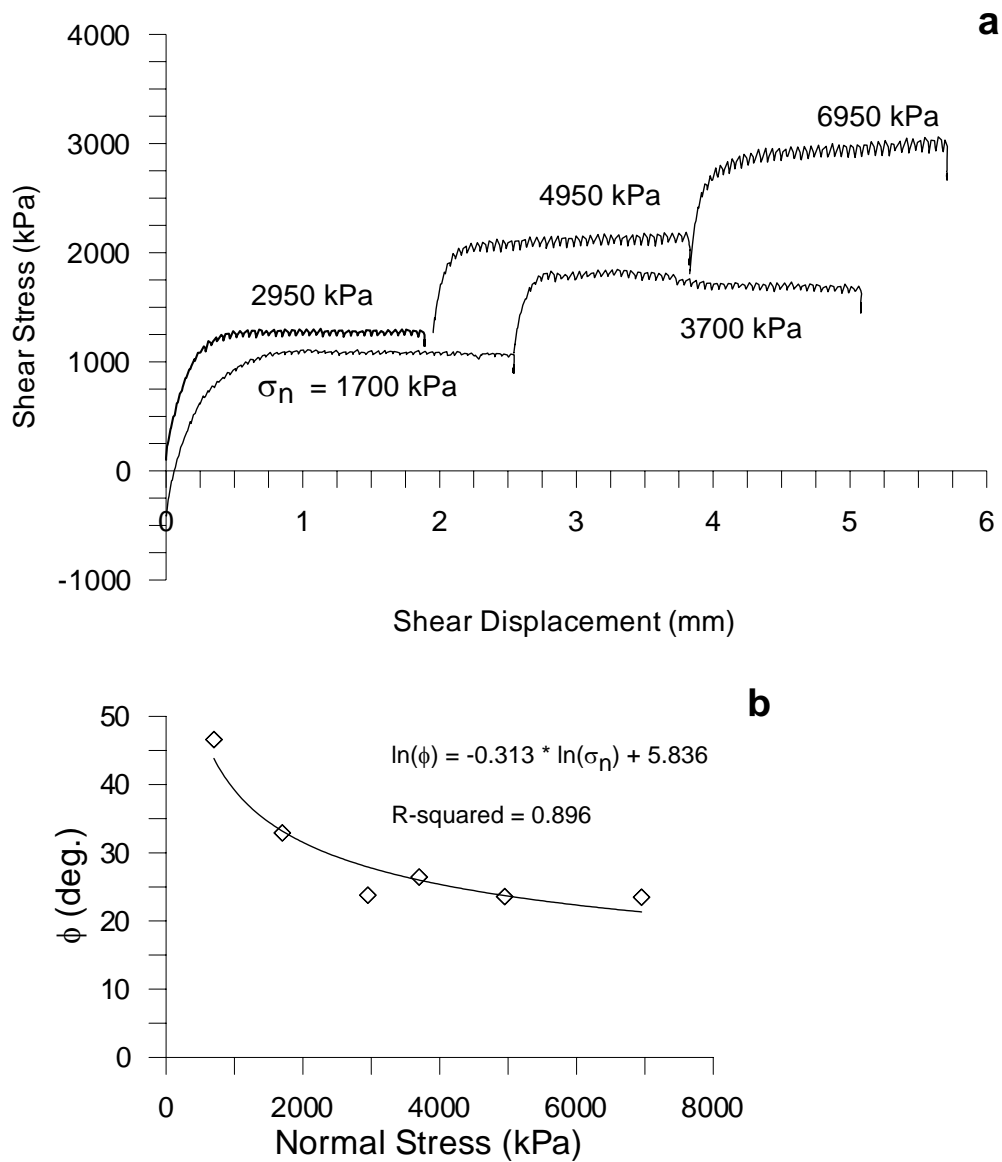


Figure 6.7. Direct shear results of a natural joint in Gareb formation, sample TBS-1: a) shear displacement vs. shear stress; b) friction angle vs. normal stress.

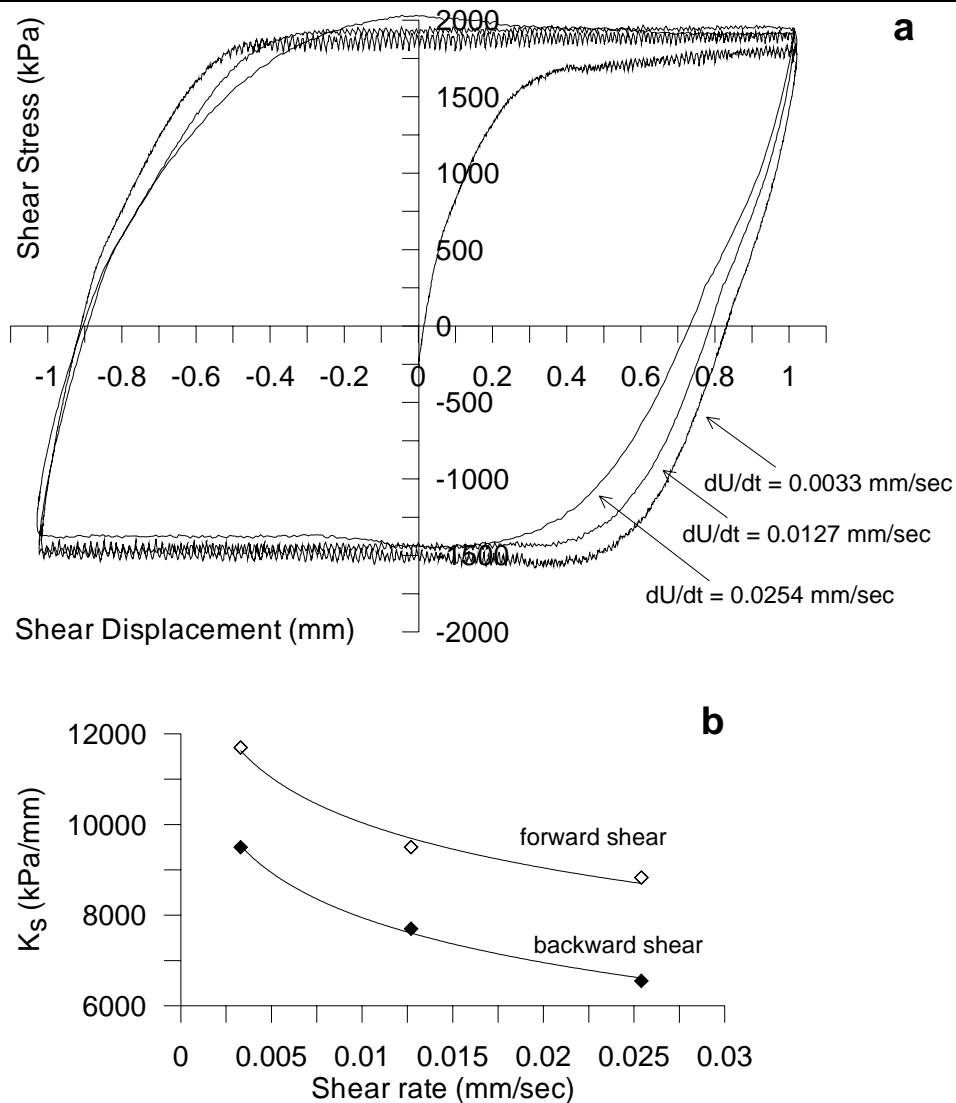


Figure 6.8. Direct shear results for polished surface in Gareb chalk, sample TBS – 2: a) shear stress – shear displacement curves; b) shear stiffness k_s as a function of shear rate.

dU/dt (mm/sec)	k_{sf} (kPa/mm)	k_{sb} (kPa/mm)
0.0033	11,700	9500
0.0127	9500	7700
0.0254	8830	6550

Table 6.3. Shear stiffness at different shear rate values for sample TBS-2. dU/dt is shear rate, k_{sf} and k_{sb} are shear stiffness for forward shear and backward shear respectively.

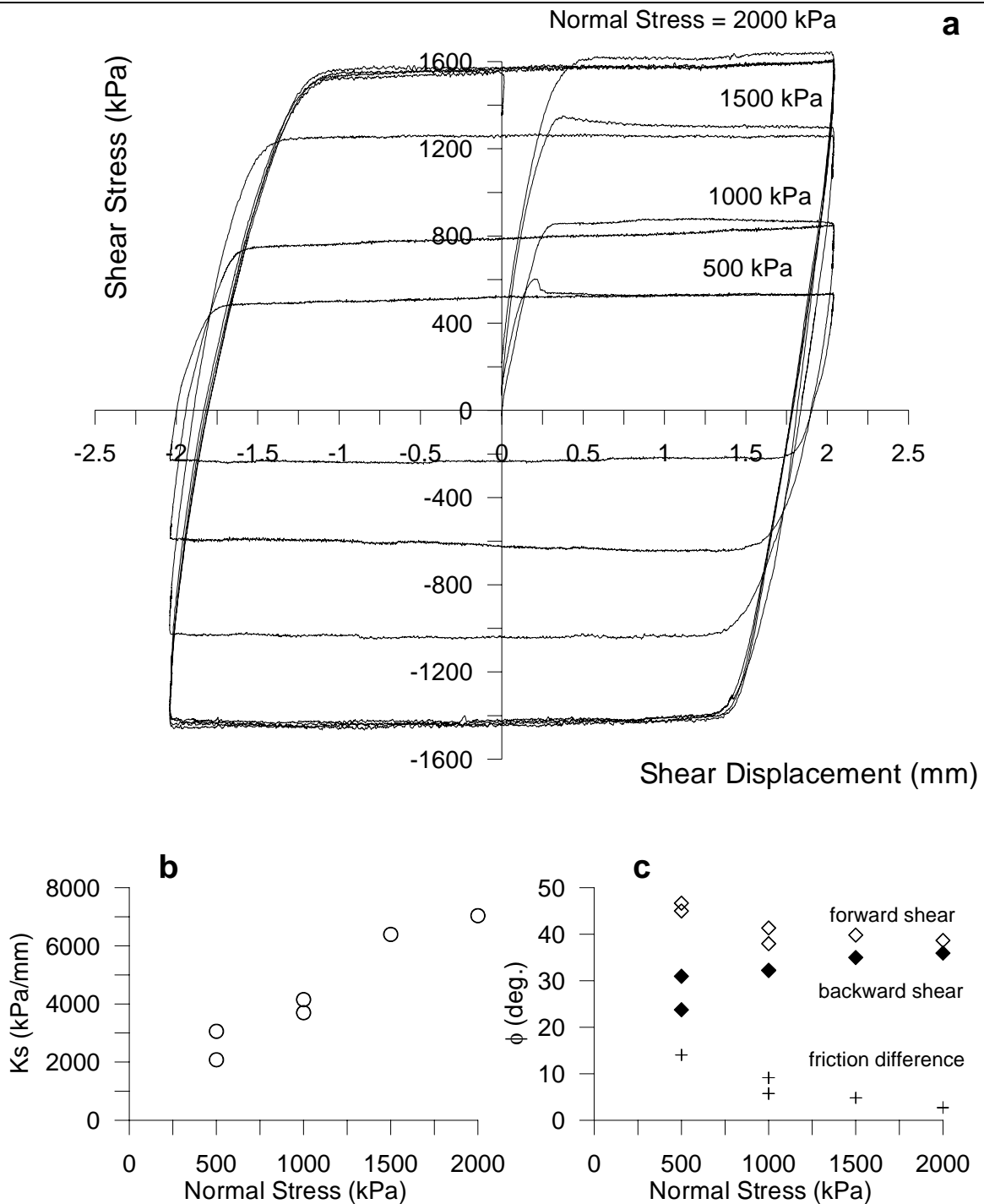


Figure 6.9. Direct shear results for a polished surface, sample TBS-4: a) shear displacement vs. shear stress; b) shear stiffness (k_s) vs. normal stress; c) friction angle (ϕ) vs. normal stress

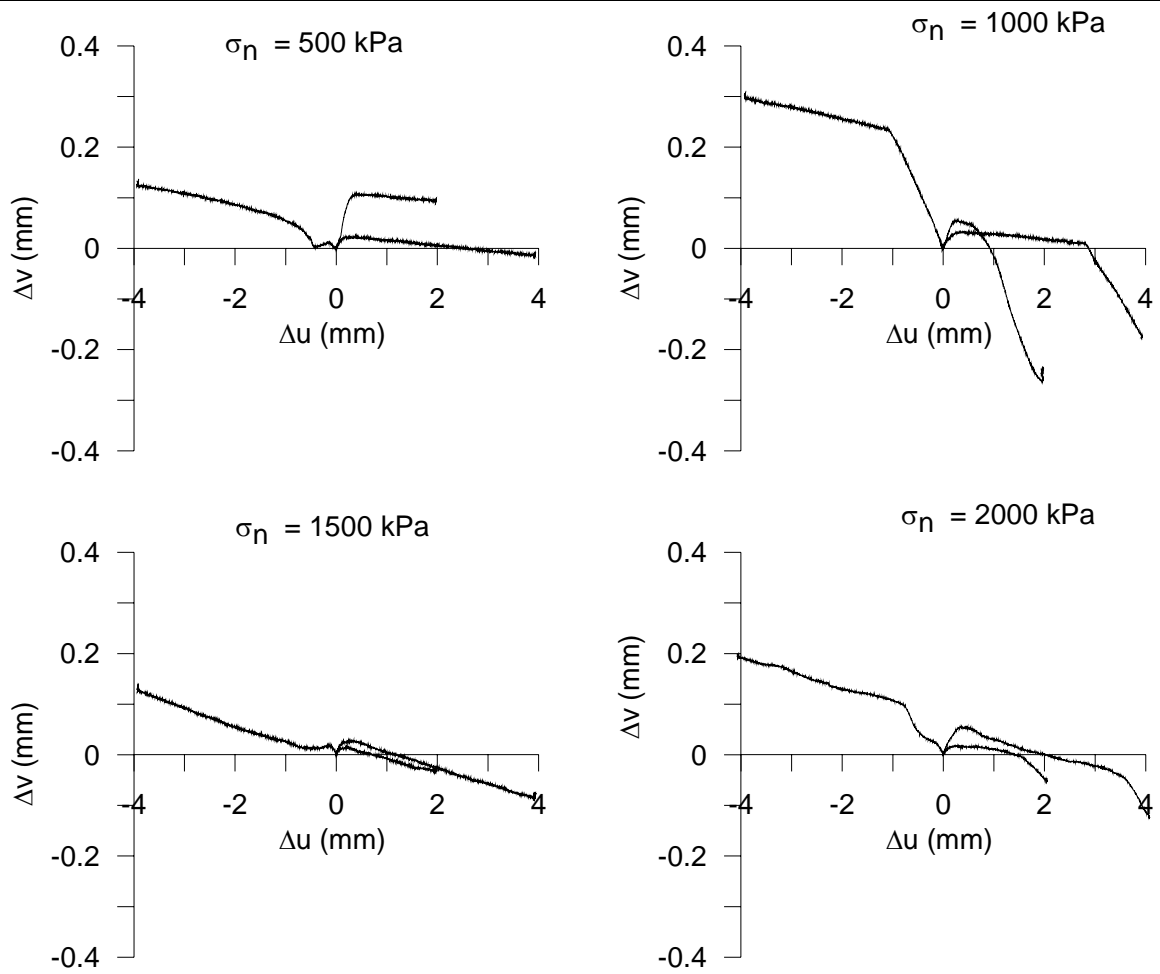


Figure 6.10. Sample TBS-4: normal displacement (Δv) vs. shear displacement (Δu) at different levels of normal stress.

6.5. Stability Analysis Using Classical Voussoir Model

Stability analysis of the Tel Beer-Sheva water reservoir was performed using the iterative procedure (Appendix) introduced by Brady and Brown (1985), and corrected by Diederichs and Kaiser (1999). The mechanical properties of the rock mass in-situ were used in the analysis (Table 6.4.). Since the rock mass was found to be transversely isotropic the values of E , ν , and UCS chosen for the analysis were the values measured in the direction parallel to bedding, which for the case of a roof in horizontally oriented layers is horizontal. Three modes of failure were considered: (1) lateral compressive failure at mid-span and abutments; (2) shear along abutments; and (3) snap through (buckling).

Density	1900 kg/m ³
Elastic Modulus	7840 MPa
Poisson's ratio	0.17
UCS	27.6 MPa
Friction angle along joints	47°

Table 6.4. Representative material properties of the Gareb Chalk.

The factor of safety against failure in compression and in shear was calculated for a wide range of beam geometries. The beam span (S) was varied from 5m to 16m, thus accounting for most possible geometries at time of failure. The beam thickness (t) was varied from 0.25m to 5m, from a single bed to the total thickness of the chalk layers, respectively.

An equation for the Factor of Safety ($F.S.$) against failure in compression is given in equation A9 of the Appendix, and the results as calculated for this study are plotted in Figure 6.11a. For beam thickness lower than 0.5m and span greater than 10m the failure is by snap through, indicated by a non-converging solution. The factor of safety against failure in

compression for all other geometries is greater than 3, increasing for thicker beams due to larger moment arm (Z) and lower axial stress (f_c).

An equation for the Factor of Safety ($F.S.$) against shear along abutments is given in equation A10 of the Appendix, and the results as calculated for this study are plotted in Figure 6.11b, where the beam span is normalized to beam thickness. Assuming that the peak friction angle along joints is $\phi = 47^\circ$, as found by direct shear tests, and assuming that the active span at time of failure was 8m, the factor of safety against shear ranges from $F.S. = 8.3$ to $F.S. = 0.83$ for beam thickness ranging from 0.5m to 5m respectively. Assuming that the active span at time of failure was 12m, the factor of safety against shear ranges from $F.S. = 12.4$ to $F.S. = 1.24$ for beam thickness ranging from 0.5m to 5m, respectively. Beams of low S/t ratio are prone to shear failure since the required moment arm (Z) for equilibrium increases with decreasing aspect ratio.

Assuming a roof span of 8m and layer thickness of 5m the failure of the ancient water reservoir at Tel Beer Sheva can be explained using the Brady and Brown procedure. However, this is not the case: the thickness of Zone 3 is 1m to 2m which is the maximum active thickness of the failed layer. Given a thickness of 2m the factor of safety against shear failure is $F.S. = 2$, for beam thickness of 1m the factor of safety is even higher than $F.S. > 4$.

For active span greater than 8m the factor of safety rises above 1 for all thickness values considered. Moreover, for beam with $r = S/t > 4$, the required friction angle for stability is $\phi > 47^\circ$. Therefore, under the given geometrical constraints and material properties the roof would not fail according to the Brady and Brown procedure.

From the described above it is concluded that classic Voussoir procedure is unconservative, predicting required friction angles for roof stability lower than the available friction angle along joints. The unconservative nature of the analysis can be attributed to the following factors:

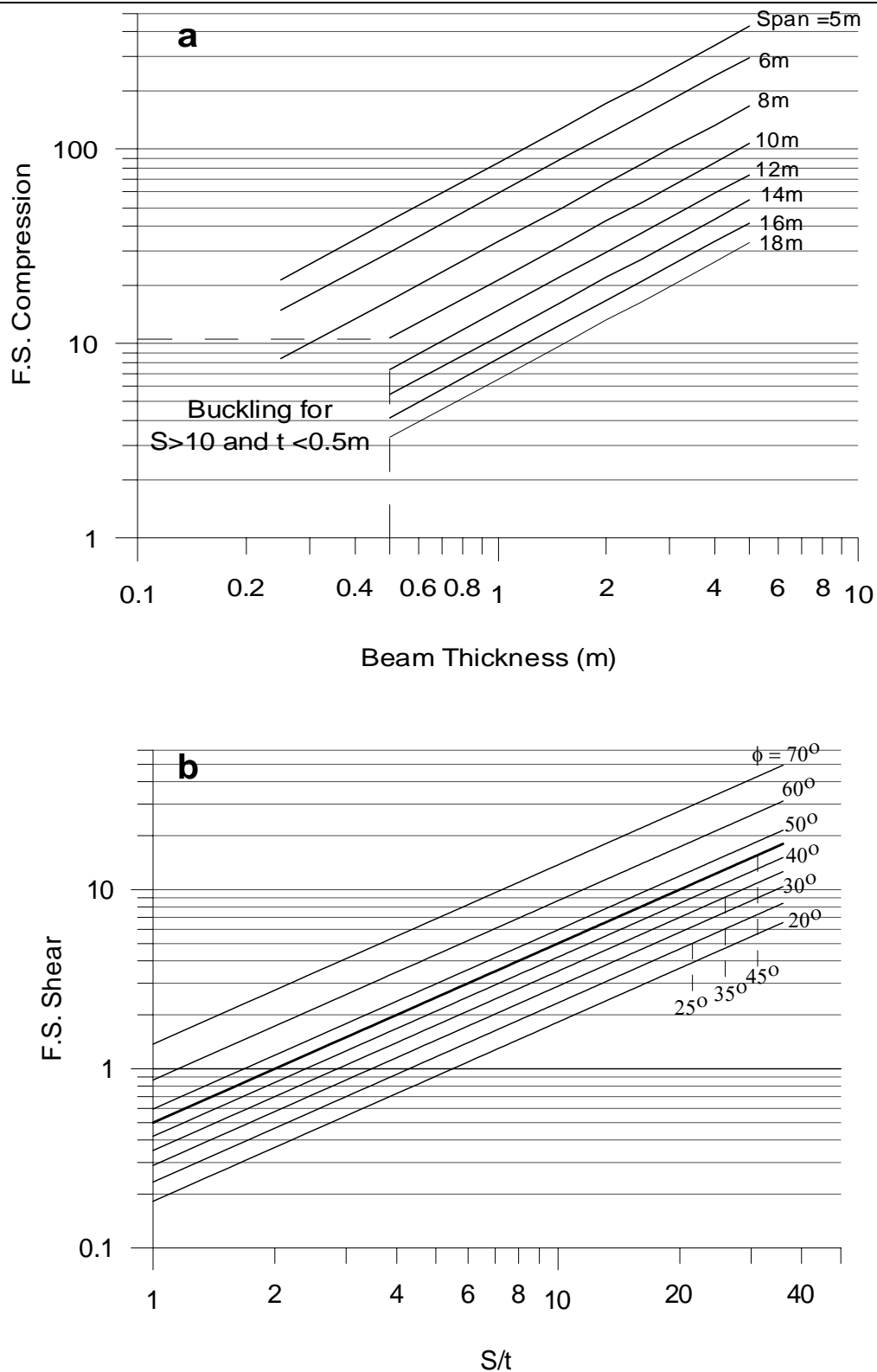


Figure 6.11. Classic Voussoir beam analysis of the Tel Beer-Sheva water reservoir: a) factor of safety ($F.S.$) against compressive failure; b) factor of safety ($F.S.$) against shear along abutments for different values of beam span (S) to thickness (t) ratio, heavy line indicates mobilized friction angle.

1) Large number of discontinuities - the rotational freedom required for stable arching in a multi-fractured beam is larger than the one required for a three-hinged beam. In a closed domain, such as the densely fractured and tightly packed rock mass of Tel Beer-Sheva, this requirement is compromised. Consequently, the vertical reaction at the abutments is not fully developed. Thus, under gravitational loading the beam will shear along the abutments. Therefore, the friction angle required for equilibrium according to the Voussoir analysis will be significantly lower than the one required for a multi fractured beam.

2.) Partial inter-bed separation - Voussoir analysis assumes that the rock mass has parted along smooth breaks forming a series of beams, thus assuring that no gravitational load is transferred to the lower members of the beam stack. In the case of Tel Beer-Sheva this assumption is not satisfied; the failed rock mass consisted of up to 4 individual beds (assuming total thickness of 2m). Thus, a vertical load transfer between beams should be considered.

When the roof is excavated in a densely fractured rock mass the classic Voussoir solution is shown to be inadequate. The large number of individual blocks, and their interactions, impedes on the analytical solution. It is concluded, therefore that for a realistic solution a numerical scheme must be employed. In the next section a back analysis of the failure at Tel Beer-Sheva using DDA is presented. The focus of the analysis is on the kinematics of a multi-block structure. The deformation of the roof as a function of joint mechanical and geometrical properties is studied, and some limitations of DDA are explored.

6.6. Numerical Analysis Using DDA

6.6.1. Numerical problems associated with multi-block systems

The transition from simple problems with a limited number of blocks to full-scale problems where the number of blocks is large (hundreds to thousands) introduces numerical problems associated with the large number of contacts involved. Most of the difficulties are associated with the no penetration/no tension contact constraint between blocks, which is the criterion controlling the convergence of the solution in each time step. In the numerical implementation of this criterion a small penetration is used. Proper choice of the penetration control parameter (g_2) assures that: there are no unnecessary contacts (where g_2 is too large) or penetrations (where g_2 is too small).

In Chapter 4 it has been shown that: 1) the numeric control parameters are interrelated; and 2) the accuracy of the solution is governed by the conditioning of the global stiffness matrix. Best accuracy is achieved for optimized time step size (g_1) and contact stiffness (g_0). In DDA the contacts between blocks are represented by elastic springs, rather than by a constitutive joint model. Therefore, the stiffness value should be chosen such that it complies with numeric convergence rather than with natural joint stiffness values.

The effect of g_1 and g_0 parameters on the convergence rate of DDA solution for a multi-block system was studied for three cases: 1) 67 blocks; 2) 98 blocks; and 3) 168 blocks. All configurations consisted of a stack of jointed beams, similar to the configuration presented in Figure 6.14b. Each case was modeled for four different g_1, g_2 couples, which for simplicity were assumed equal: 1) $g_1=g_2=0.01$; 2) $g_1=g_2=0.005$; 3) $g_1=g_2=0.001$; and 4) $g_1=g_2=0.0005$. The penalty stiffness for each g_1, g_2 couple was varied in increments from $50 \cdot MN/m$ to $100,000 \cdot MN/m$. All simulations were performed for $k_0 = 1$, the number of time

steps was set such that the total time of each simulation was 0.25 sec . Material properties of the blocks were set to $E = 7.48 \text{ GPa}$, $\nu = 0.17$, and $\rho = 1.9 \cdot 10^3 \text{ kg/m}^3$ (Gareb chalk). Friction angle along joints was set to $\phi = 45^\circ$ ($\mu = \tan\phi = 1$). The results of the analysis are presented in Figure 6.13, which is a series of plots showing the average number of iterations for a time step $i_{av} = i/n$ (where i is the total number of iterations and n is the total number of time steps) as a function of penalty stiffness for different values of $g1$, $g2$.

For $g1 = g2 = 0.01$ the average number of iterations per time step increases with $g0$, in a nearly linear fashion. For the configuration of 67 blocks the solution diverges when $g0 > 100 \text{ MN/m}$, whereas for the configurations of 98 and 168 blocks the solution converges up to $g0 = 10,000 \text{ MN/m}$, where i_{av} values increase up to 24 iterations per time step.

For $g1 = g2 = 0.005$ the solution converges for all studied configurations, with i_{av} ranging from 2 to 16 for all values of $g0$. Setting $g1 = g2 = 0.001$ improves the convergence rate of the solution: for $50 \text{ MN/m} < g0 < 1000 \text{ MN/m}$ the convergence rate is nearly constant at $i_{av} = 1.8$ for all studied configurations. Increased $g0$ degrades the convergence rate, as $i_{av} = 6.4$ at $g0 = 50,000 \text{ MN/m}$. For $g1 = g2 = 0.0005$ the solution rapidly converges for $50 \text{ MN/m} < g0 < 5000 \text{ MN/m}$ for all studied configurations, with $i_{av} \leq 1.5$. Setting $g0 > 5000 \text{ MN/m}$ degrades the convergence rate, up to values of $i_{av} = 3.5$.

From the discussion above it is clear that for multi block configurations the DDA solution converges independently of penalty stiffness value ($g0$), provided that the time step size ($g1$) and penetration control parameter ($g2$) are sufficiently small. In Chapter 4 it was shown that the accuracy of the numeric solution is improved for high values of penalty stiffness. Based on these observations it can be concluded that the numeric control parameters for multi block analysis should be chosen such that solution accuracy is not compromised by the convergence rate, and that the failure mode is correct.

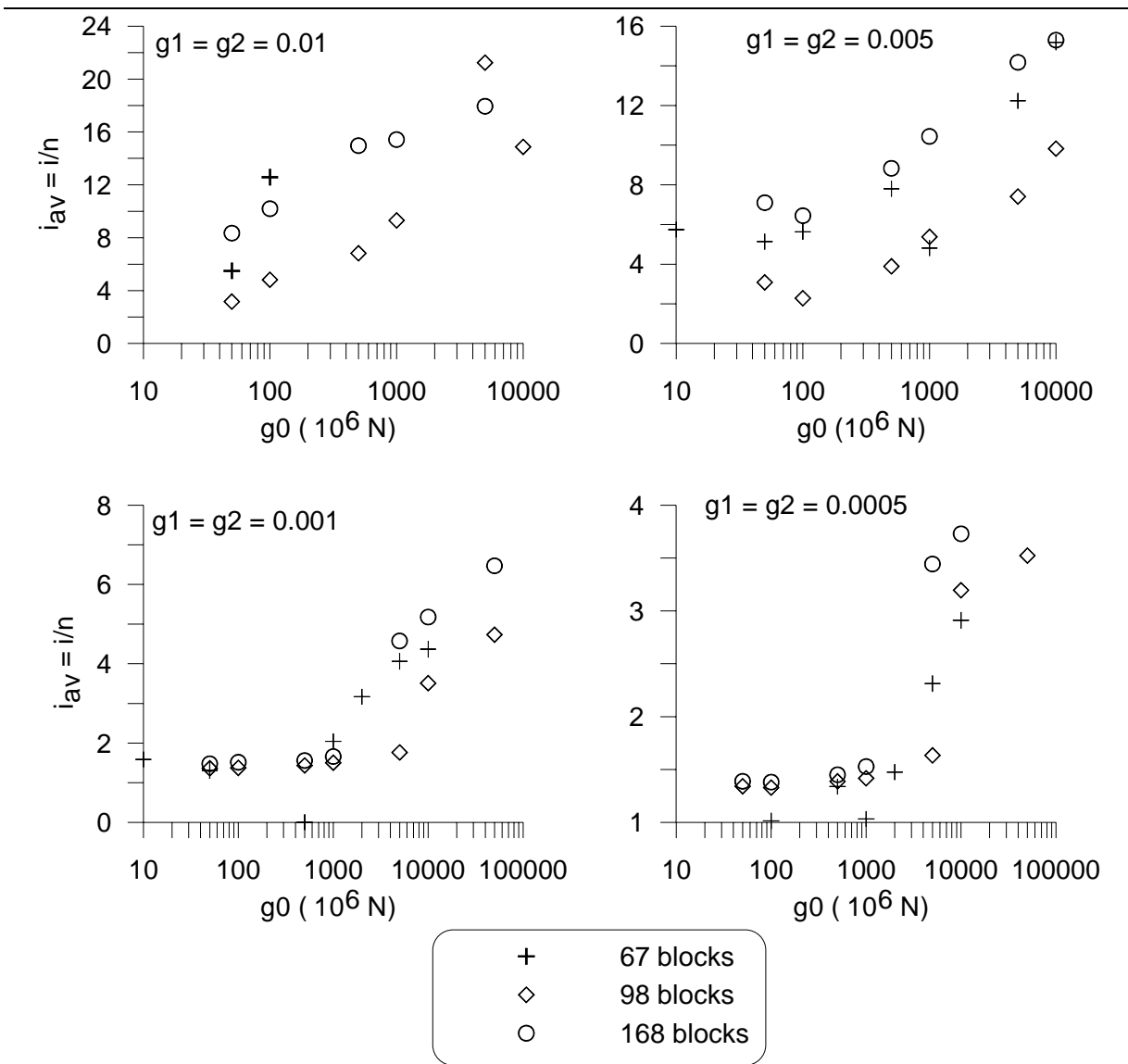


Figure 6.13. DDA multi block model: average number of iterations per time step ($i_{av} = i/n$) as a function of penalty stiffness (g_0) for different values of time step size (g_1) and penetration control parameter (g_2).

6.6.2. DDA analysis of the Tel Beer-Sheva water reservoir – numerical setup

DDA analysis of the Tel Beer-Sheva ancient water reservoir was performed for two geometric configurations:

1. A single layer of thickness $t = 0.5\text{ m}$, representing the immediate roof of the excavation, Figure 6.14a.
2. A 5m stack of horizontal beams, each of thickness $t = 0.5\text{ m}$, conforming with the actual roof thickness, Figure 6.14b.

The active span of both configurations was set to $S = 8\text{ m}$. While configuration 1 is compatible with the Voussoir model, configuration 2 is a realistic model of the roof of the water reservoir. Two fixed blocks, each containing three fixed points, represent the abutments.

The effect of joint friction was studied for a constant joint spacing of $S_j = 0.25\text{ m}$ (in accordance with the average spacing of J1 and J2 observed at the site) while the friction along joints (ϕ_{av}) was varied from $\phi_{av} = 20^\circ$ to $\phi_{av} = 80^\circ$. The effect of friction angle was studied for $\phi_{av} = 47^\circ$ (peak friction angle from direct shear tests) while joint spacing was changed from $S_j = 0.25\text{ m}$ to $S_j = 4\text{ m}$. For configuration 1 the displacements were measured at the lower fiber of the beam at selected points in intervals of 0.5 m . For configuration 2 the displacements were measured at five locations as shown in Figure 6.14b: 1) $m1$ - mid-span of immediate roof; 2) $m2$ - mid-span at $m1+2.5\text{ m}$; 3) $m3$ - mid span at $m1+5\text{ m}$; 4) $m4$ - left abutment at $m1+2.5\text{ m}$; 5) $m5$ - right abutment at $m1+2.5\text{ m}$.

Material properties of the Gareb chalk and numeric control parameters of DDA analysis are given in Table 6.5. The joints are modeled as no-tension, no-cohesion interfaces, namely shear resistance along joints is purely frictional, in compliance with field findings.

Density	1900 kg/m ³
Elastic Modulus	7840 MPa
Poisson's ratio	0.17
Penalty stiffness (<i>g0</i>)	1000 MN/m
Time step size (<i>g1</i>)	0.00025 sec
Penetration control parameter (<i>g2</i>)	0.00025
Dynamic control parameter (<i>k01</i>)	1

Table 6.5. Material properties and numeric control parameters for the DDA model of the Tel Beer-Sheva water reservoir.

In the field, the chalk layers are overlain unconformably with a 5m thick conglomerate layer; the unconformity plane is considered open and discontinuous. The conglomerate layer in the field is continuous without apparent cracks or joints.

The first order displacement approximation in DDA results in constant stress/strain elements. Therefore, because the conglomerate layer consists of a single block, its deformation cannot be modeled properly with DDA. Consequently the vertical deflection of the layer and vertical load on the chalk cannot be evaluated accurately. Since the conglomerate layer is continuous, however, the mid-span deflection can be assessed by analogy to an elastic, simply supported beam (Obert and Duval, 1967). The mechanical properties of the conglomerate layer are unknown since the material is highly heterogeneous; assuming a low stiffness of $E = 100 \text{ MPa}$ the deflection at mid-span would be $\delta = 0.00094m$, for $E = 1000 \text{ MPa}$ the deflection at mid-span would be $\delta = 0.000094m$. These deflection are quite small and, therefore, it is assumed that load transfer between the conglomerate and the chalk is negligible; hence, the conglomerate layer is not modeled here.

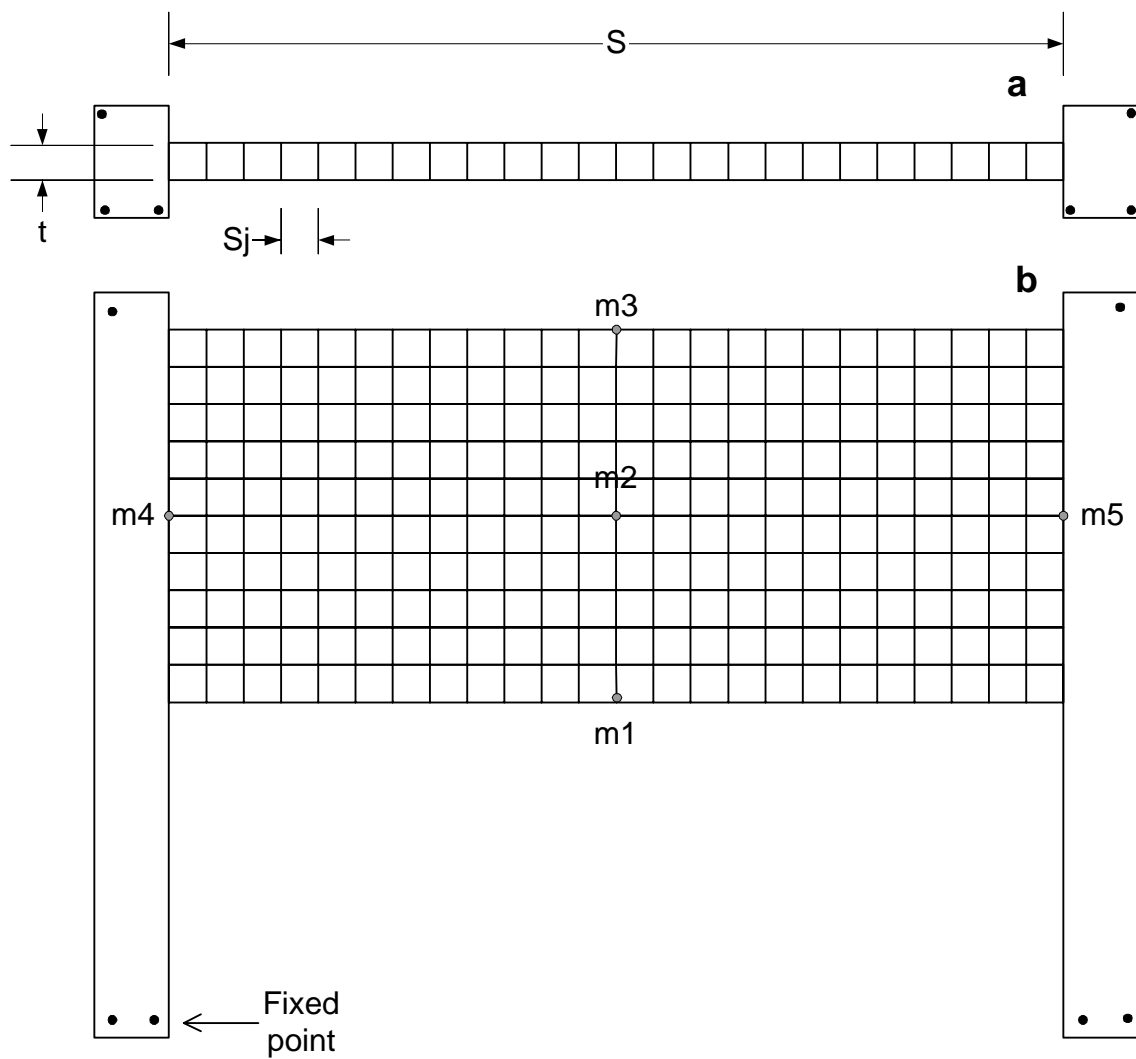


Figure 6.14. Geometry of DDA model of the Tel Beer-Sheva water reservoir: a) single layer model; b) multi-layered model.

6.6.3. DDA analysis of the single layer configuration

The results of DDA analysis for the single layer configuration are presented in Figure 6.15a, which is a plot of mid-span deflection (δ) after 0.25sec versus friction angle (ϕ) and joint spacing (S_j). Figures 6.15b,c are time histories of mid-span deflection for different values of friction angle and joint spacing respectively.

Given joint spacing of $S_j = 0.25\text{m}$ the beam deflects progressively and eventually fails for friction angles of $\phi_{av} < 78^\circ$. For friction angles of $\phi_{av} \geq 78^\circ$ the beam attains stable equilibrium after small initial deflection. Figures 6.16a,b,c show the displacements, u , v , and rotation ω respectively, of the lower fiber after 0.25sec for selected values of friction angle: a) 30° ; b) 45° ; c) 75° ; d) 80° . DDA graphic outputs of the final deformed positions of the blocks for these selected values of friction are presented in Figure 6.17.

At low values of $\phi_{av} = 30^\circ$ and $\phi_{av} = 45^\circ$ most of the deformation is achieved through differential inter-block shear, which attains maximum at the mid-span and minimum at the abutments. The rotation of the blocks is mostly uniform and symmetric, up to ± 0.1 radians, where at the left hand side of the beam the blocks rotate clockwise and vice versa. Similar beam deflection profile was attained by Evans (1941) while experimenting with brick beams. The deformation characteristics are changed when the friction angle along joints rises, e.g. $\phi_{av} = 75^\circ$ and $\phi_{av} = 80^\circ$, inter-block shear is reduced while the rotation at the beam ends rises to ± 0.3 radians.

From the rotation data it is evident that at low values of friction angle the moment arm of the lateral couple is not developed effectively and beam deformation occurs mainly due to inter-block shear, which consequently leads to failure. Where the available shear resistance along joints is sufficiently high to preclude excessive vertical displacements, block rotation

and build-up of lateral thrust equilibrate the overturning moment of the vertical couple, and the beam reaches equilibrium position.

Increasing the block aspect ratio ($r_b = S_j/t$) of the individual blocks by setting $S_j = 0.5m$ ($r_b = 1$), and assuming peak friction angle of $\phi_{av} = 47^\circ$ (peak friction angle from direct shear tests), results in mid-span deflection of $\delta = 0.08m$ (after 0.25 sec), compared with $\delta = 0.22m$ for $S_j = 0.25m$. However, the beam does not attain equilibrium, and eventually fails. Examination of the deformation time histories for beams of different aspect ratio (Figure 6.15c) reveals that equilibrium is marked by the oscillatory nature of the solution (this effect was described in section 6.6.1), as opposed to gradually increasing deflection of failing beams. Equilibrium is met when $r_b \geq 2.5$ ($S_j \geq 1.25$) and $\delta \leq 0.025m$. The style of deformation is similar: for unstable geometry the beam fails by inter-block shear, with relatively small rotations, while for stable geometries stability is achieved through effective rotation.

From the described above it is evident that a single beam of span $S = 8m$, thickness $t = 0.5m$, block aspect ratio $r_b = S_j/t = 0.5$, and friction angle along joints of $\phi_{av} = 47^\circ$ is not stable. Stability is assured for $\phi_{av} \geq 78^\circ$. According to classical Voussoir solution for beam of span $S = 8m$, thickness $t = 0.5m$ (block aspect ratio $r_b = 8$) stability is assured for $\phi_{av} > 20^\circ$, with expected deflection of $\delta = 0.002m$. DDA analysis predicts similar deflection for block aspect ratio of $r_b = 4$.

The underlying assumption of immediate roof (single layer) analysis is that vertical load from overlaying layers is transmitted laterally to the abutments, rather than vertically as transverse loads to the lower layers. This condition is not satisfied within the layers overlying the water reservoir, namely the failure zone is up to 2.5m thick. Given average bed thickness of $t = 0.5m$ the failure zone contained 5 individual layers. The stability of a multi-layered and jointed structure, the laminated Voussoir beam (a term introduced by Hatzor and Benary, 1998), is explored in the following section.

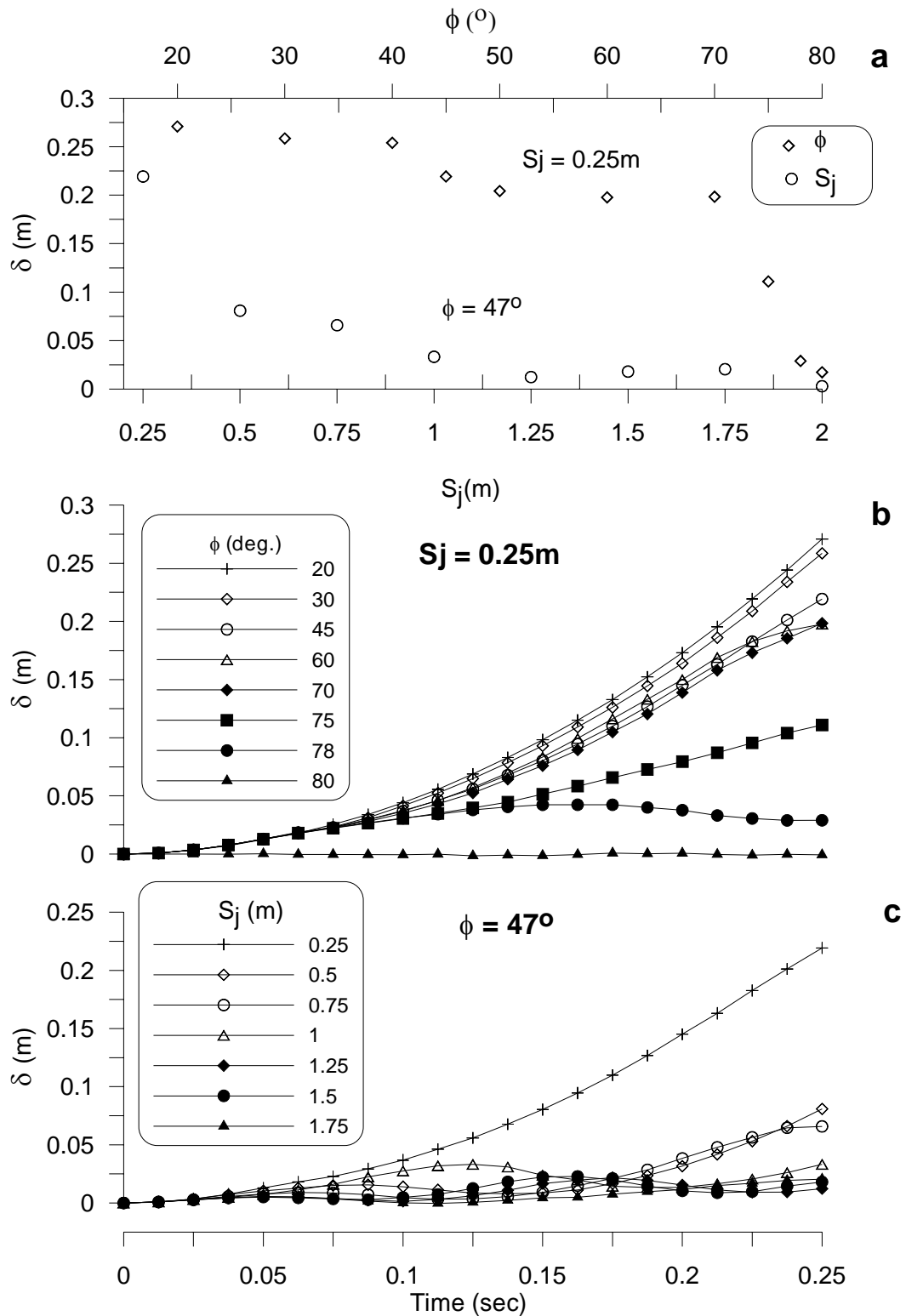


Figure 6.15. DDA prediction for mid-span deflection of the single layer model: a) as friction angle (ϕ) and joint spacing (S_j); b) time histories for different values of friction angle, for joint spacing of $S_j = 0.25m$; c) time histories for different values of joint spacing, for available friction angle of $\phi = 47^\circ$.

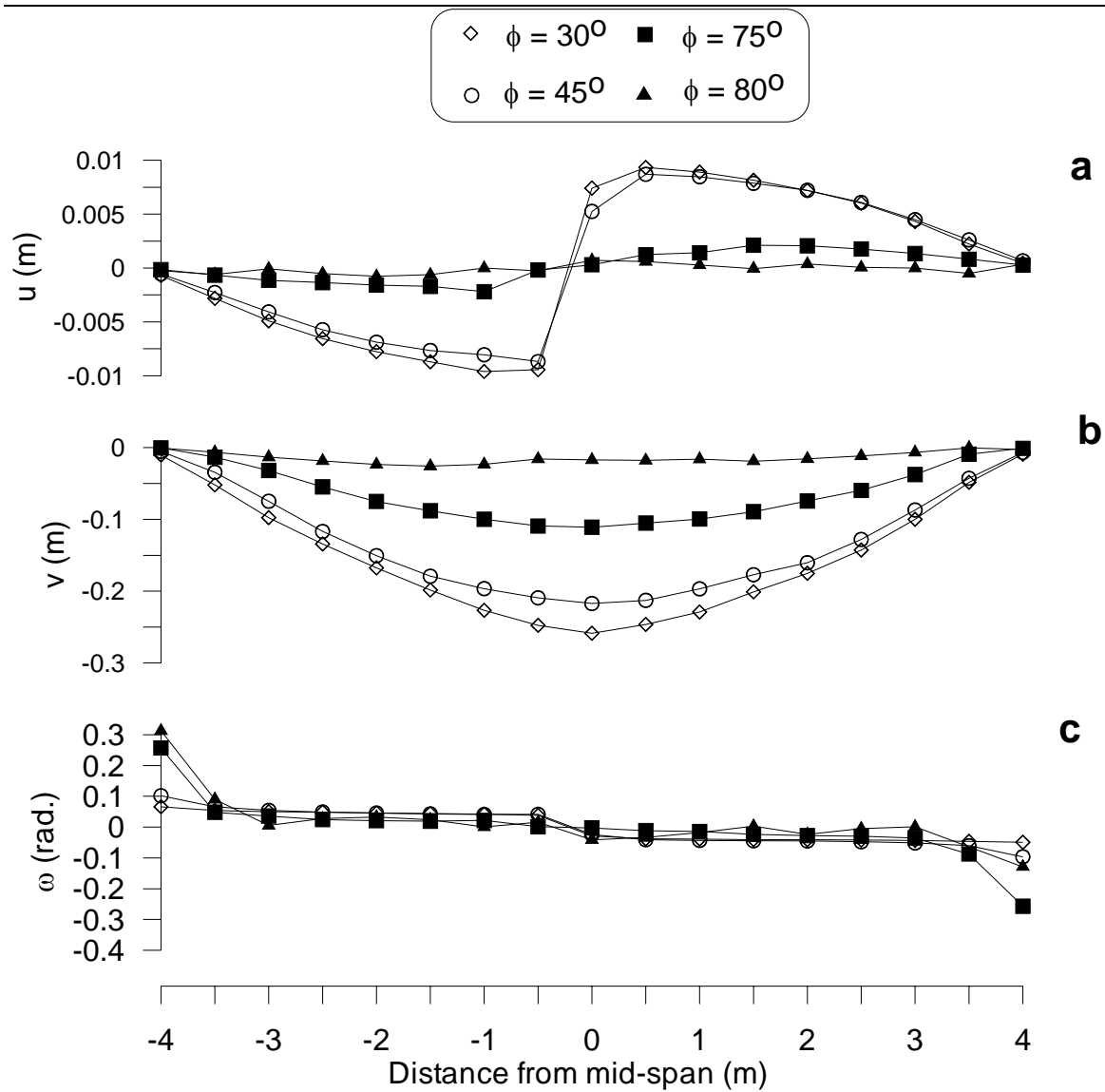
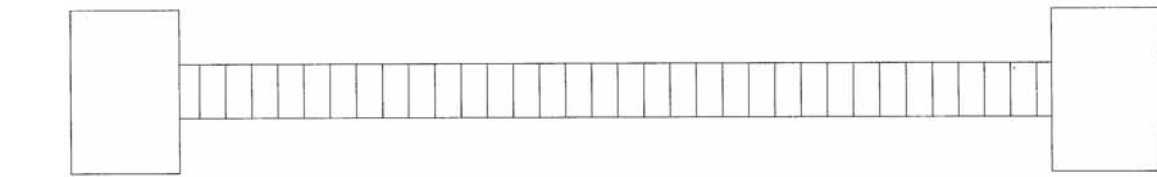
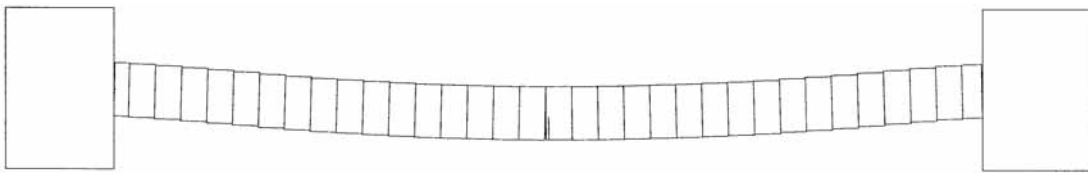


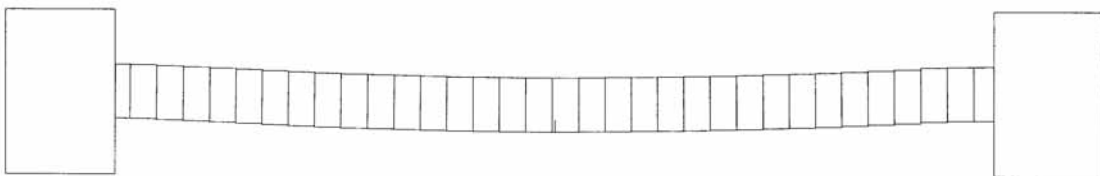
Figure 6.16. Deformation profiles of the DDA single layer model, measured at the lowermost fiber of the beam: a) horizontal displacement (u); b) vertical displacement (v); and c) rotation (ω).



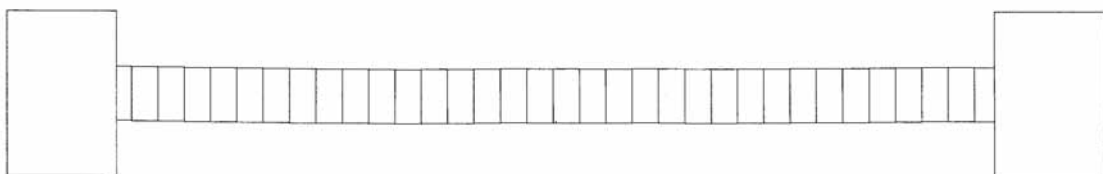
a)



b)



c)



d)

Figure 6.17. DDA graphic output of single layer deformation for different values of joint friction angle: a) original geometry; b) $\phi_{av} = 45^\circ$; c) $\phi_{av} = 75^\circ$; d) $\phi_{av} = 80^\circ$.

6.6.4. DDA analysis of sequence of layers - laminated Voussoir beam

The results of DDA analysis for the laminated voussoir configuration are presented in Figure 6.18a, which is a plot of mid-span deflection (δ) after 0.25sec versus friction angle (ϕ) and joint spacing (S_j). The deflection data is provided for three points located midspan separated vertically by 2.5m as follows: 1) $m1$ - mid-span of immediate roof; 2) $m2$ - mid-span at $m1+2.5m$; 3) $m3$ - mid span at $m1+5m$. Time histories of the three measurement points for different values of joint spacing are presented in Figure 6.18b,c,d. Graphic output of deformed system of blocks after 0.25 sec for $S_j = 0.25m$ and selected values of friction angle are given in Figure 6.19: a) $\phi_{av} = 30^\circ$; b) $\phi_{av} = 50^\circ$; c) $\phi_{av} = 60^\circ$; d) $\phi_{av} = 70^\circ$.

For block of aspect ratio $r_b = 0.5$ the deflections are excessive for all analyzed values of friction angle, and failure is expected. The deflections through the stack of layers show that $\delta_{m1} > \delta_{m2} > \delta_{m3}$. For $\phi_{av} < 50^\circ$ the deflections at the specified measurement points are essentially similar: $\delta_{m1} \approx 0.43m$; $\delta_{m2} \approx 0.26m$; and $\delta_{m3} \approx 0.18m$. The vertical differences of the deflection values, $\Delta_{1,2} = \delta_{m1} - \delta_{m2}$ and $\Delta_{1,3} = \delta_{m1} - \delta_{m3}$, are similar as well: $\Delta_{1,2} \approx 0.18m$ and $\Delta_{1,3} \approx 0.08m$, thus implying that for $\phi_{av} < 50^\circ$ the transverse loads across the stack are independent of the friction angle along the joints. Most of the deformation is achieved through inter-block shear since lateral thrust is not fully developed and the gravitational load is not equilibrated, leading to progressive failure.

When shear resistance is increased, $\phi_{av} = 60^\circ$, the deflection of the layers is reduced, and rotation of the individual blocks in the lowermost layers is evident (Figure 6.16c). Maximum inter-block shear is taking place at the center of the stack, fading towards the abutments. For $\phi_{av} > 60^\circ$ increased shear resistance reduces inter-block shear displacement. Deformation characteristics are changed from inter-block shear of individual layers to increased rotation of the individual blocks, followed by lesser shear. The displacements are

reduced to $\delta_{m1} < 0.15m$, $\delta_{m2} < 0.13m$ and $\delta_{m3} < 0.11m$, while the vertical difference is $\Delta_{1,2} \approx \Delta_{1,3} < 0.03m$. Thus the behavior of the roof is changed from a succession of layers to coherent beam encompassing the overall thickness of the layers. However, stability is not achieved since the deflections are yet extensive (refer to Figure 6.18).

Increasing the aspect ratio of the individual blocks to by setting $r = 1$ ($S_j = 0.5m$), and assuming friction angle of $\phi_{av} = 47^\circ$ (peak friction angle from direct shear), reduces the displacements to $\delta_{m1} = 0.131m$, $\delta_{m2} < 0.116m$ and $\delta_{m3} < 0.106m$, compared with $\delta_{m1} = 0.434m$, $\delta_{m2} < 0.246m$ and $\delta_{m3} < 0.155m$ for $r = 0.5$ ($S_j = 0.25m$). Further increasing the block aspect ratio to $r_b \geq 1.5$ assures the stability of the roof by reducing the deflection to $\delta_{m1} < 0.05m$, $\delta_{m2} < 0.03m$ and $\delta_{m3} < 0.01m$. Equilibrium solutions are attained for block of $r \geq 1.5$ ($S_j \geq 0.75m$).

6.6.5. Limitations of DDA

Analysis of the Tel Beer-Sheva water reservoir by DDA suffers from a number of drawbacks associated with geometrical definitions and numerical problems. These shortcomings affect DDA predictions when compared with findings at the site. However, these limitations are conservative, as opposed to the unconservative nature of the classic Voussoir analysis.

The dome-like geometry of the failure area indicates that the problem is truly three dimensional (3-D) rather than two-dimensional (2-D). This observation limits the applicability of both DDA and classic Voussoir analysis, since both are two-dimensional methods. The stabilizing effect of the compressive stress in the normal to plane direction σ_{zz} is ignored. A true 3-D model of the problem is extremely difficult, due to the extremely large number of block elements involved. For a single layer configuration the number of

blocks is 1024, for sequence of layers the number of blocks exceeds 10,000. The number of DDA deformation variables and degrees of freedom for 3-D DDA analysis is 3 and 12, respectively, compared with 2 and 6 for 2-D DDA analysis. Each element in the global stiffness matrix is a 12×12 sub-matrix. The global stiffness matrix for a system of n blocks is $12n \times 12n$ matrix. Thus, the global stiffness matrix becomes extensively large. Furthermore, contact formulation of the 3-D problem is difficult mainly due to great number of contacts involved and increased deformational freedom at each contact. The convergence of such a large system is extremely difficult and slow. At present, the applicability of 3-D DDA to full-scale problems is limited. Therefore, 2-D analysis is numerically and practically advantageous over 3-D analysis, at present time.

In analysis presented above the abutments are assumed rigid, this achieved by assigning three fixed points to each abutment block. Consequently, the cracked beams will first shear along abutments simultaneously with inter-block shear until a sufficient kinematical freedom is gained and block rotation will take place. This in turn will produce movement resisting moments, until stable arching is attained. Therefore the vertical displacements as calculated by DDA are larger than the ones expected to occur within a natural rock mass, where the abutments are not rigid, but rather deformable, and where blocks rotation are expected to co-act with shear displacements.

The graphic output of Figure 6.19 shows that for friction angles lower than 70° the beds are separating, and apparently are deflecting under their own weight. This result should be examined in light of the geometrical and mechanical constraints of the DDA model: stiff abutments and simply deformable blocks. The individual blocks cannot deform, and the beam has to shear along abutments to allow rotational freedom. The upper beams transfer the vertical loads downward primarily along the abutments. Larger displacement along abutments

allows larger rotational freedom, and consequently larger mid-span deflection. Based on these insights the deflection under own weight assumption should be ruled out.

The jointed layers are modeled such that each layer is free to shear along the abutments. In the field the layers only partially comply with the model, since individual end blocks may be supported by the abutments, forming a structure of cantilever beams, which consequently reduce the active span. However, the relatively dense jointing of the Gareb chalk (ca. $0.25m$) minimizes this effect.

The first order displacement approximation in DDA results in constant strain/stress elements, and stress concentrations within the blocks are not computed. The stability of the beams however is achieved through rotation, which must produce stress concentration at the contacts. Moreover, in weak rocks such stress concentrations can lead to failure of the intact rock, thus to changes in contacts size and stiffness, which in turn can lead to further deterioration of the individual blocks integrity and overall structural stability. A complete stress distribution for the entire modeled region is not available. This shortcoming is acute when the individual blocks are large. However for small blocks the stresses within the blocks are nearly constant. Thus for a system consisting of a large number of small blocks, as in the case of Tel Beer-Sheva, the stress distribution is assumed to be modeled with adequate accuracy.

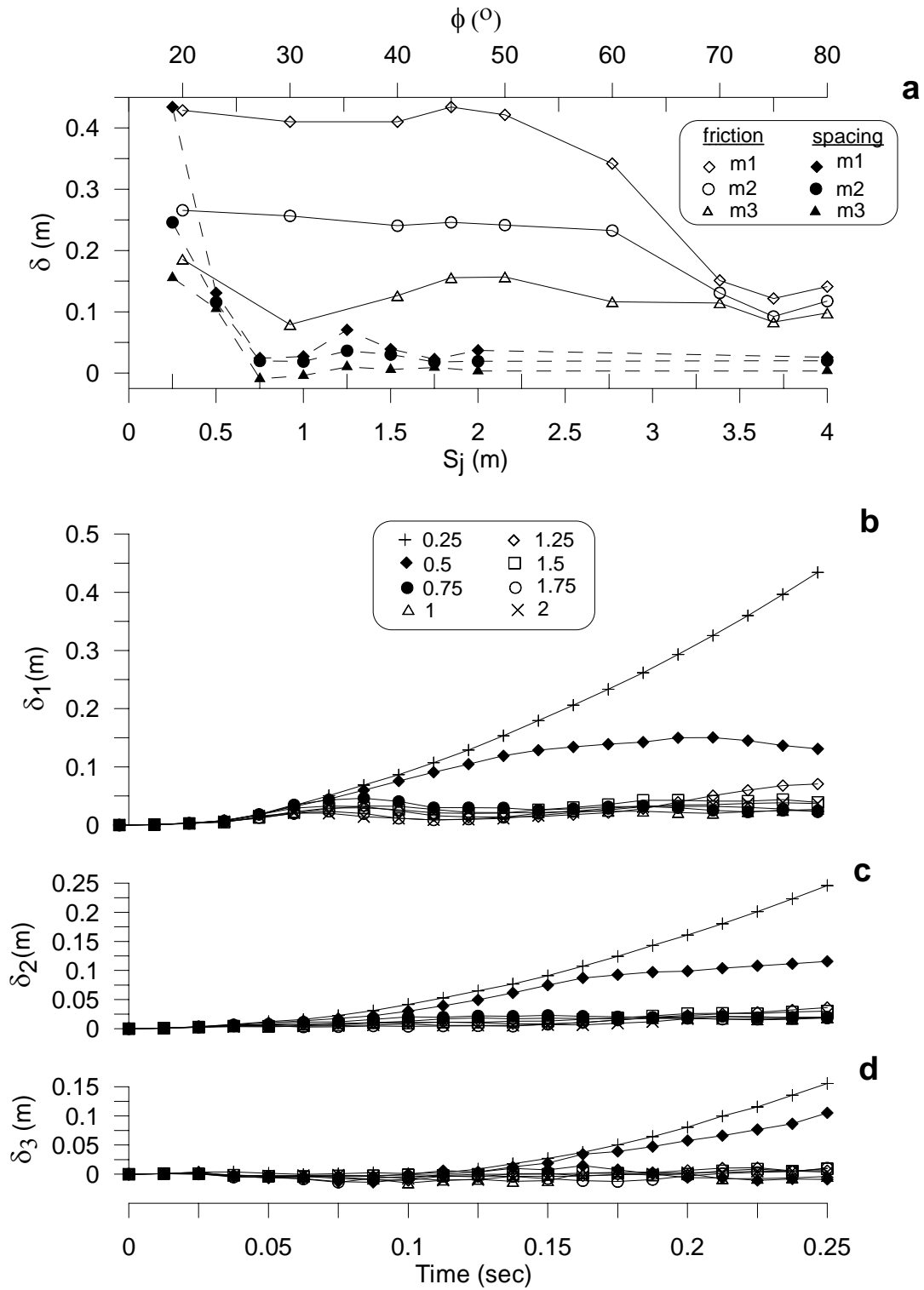
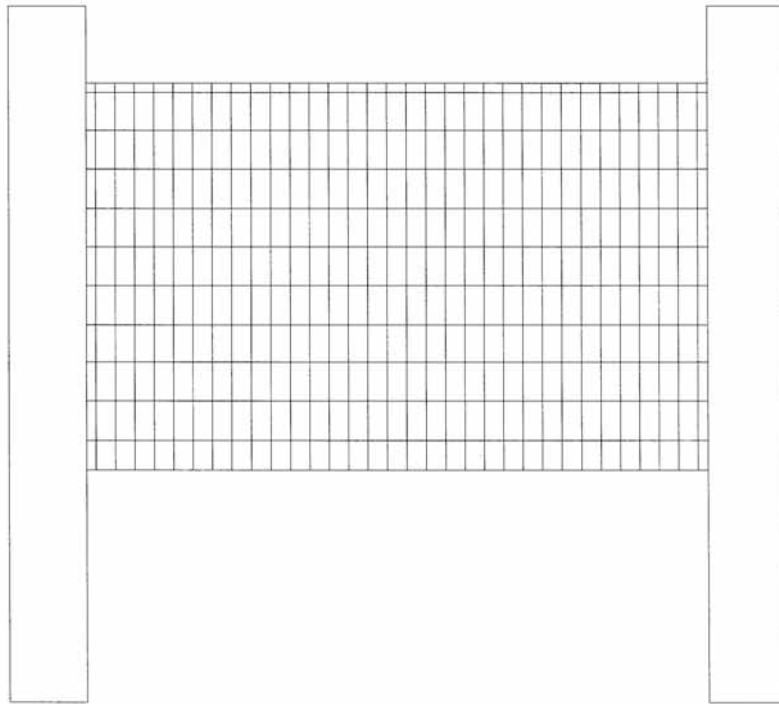
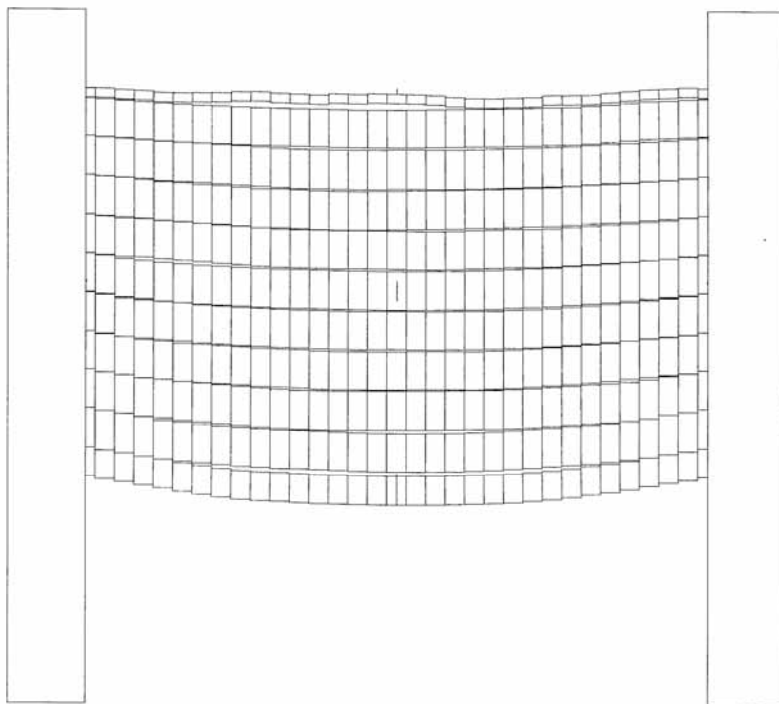


Figure 6.18. a) DDA prediction for mid-span deflection of the multi-layered model, at measurement points $m1$, $m2$, and $m3$ as a function of friction angle (ϕ) and joint spacing (S_j); b), c) and d) are time histories for different values of joint spacing at measurement points $m1$, $m2$; and $m3$ respectively.

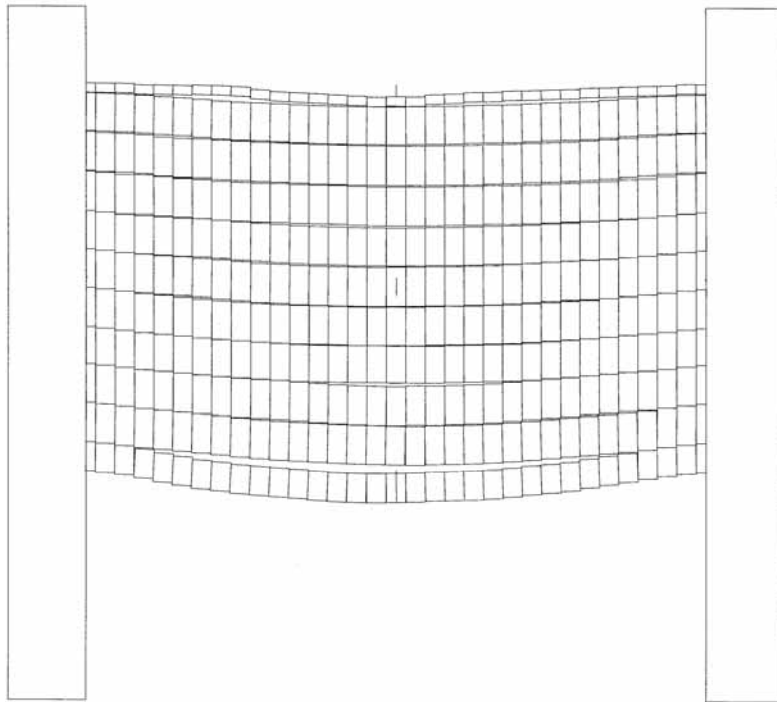


a)

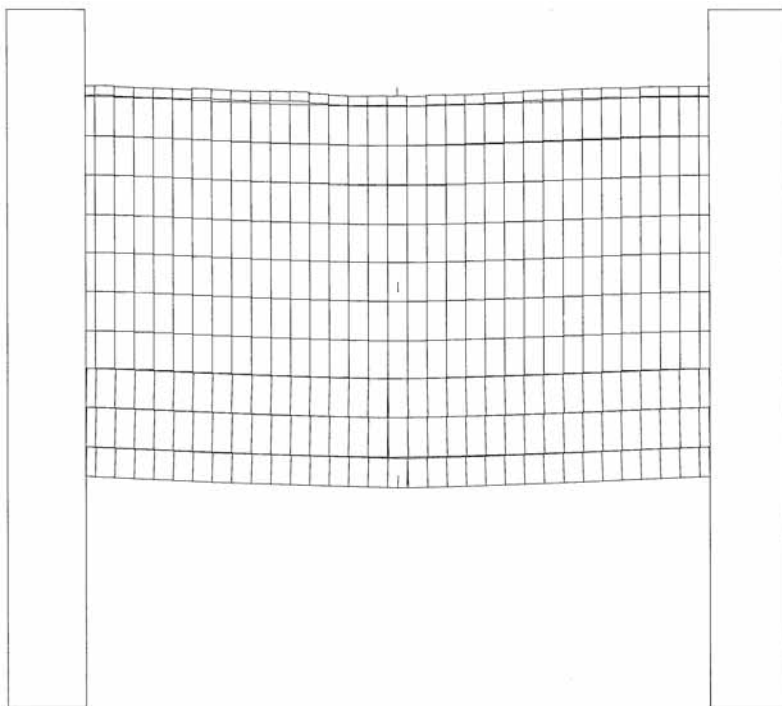


b)

Figure 6.19. DDA graphic output of the multi-layer deformation for different values of joint friction angle: a) original geometry; b) $\phi_{av} = 30^\circ$.



c)



d)

Figure 6.19. (cont.) DDA graphic output of the multi-layer deformation for different values of joint friction angle: c) $\phi_{av} = 50^\circ$; and d) $\phi_{av} = 70^\circ$.

6.6.6. Comparison between DDA and classic Voussoir solutions

Stability analysis of the Tel Beer – Sheva water reservoir showed that the classic Voussoir analysis is unconservative. Voussoir analysis predicts stability for friction angles of $\phi_{av} > 20^\circ$, but with a peak friction angle of $\phi_p = 47^\circ$ the roof has failed. DDA analysis for a single layer with multiple joints showed that stability is assured for friction angles of $\phi_{av} > 75^\circ$. Clearly DDA prediction is more accurate, albeit conservative (refer to previous section). The mode of failure of the multi-jointed beam is clearly shown in Figure 6.16: maximum inter block shear developed at the mid span, whereas at the abutments block rotation attained maximum value. This mode of failure can be regarded as sagging. DDA showed that when the shear resistance along joints is increased stability is achieved through increased rotation of blocks near the abutments. Investigation of block size effect showed that the beam stability improves for blocks with high aspect ratio; thus the findings of Passaris et al., (1993) are confirmed.

DDA showed that for the case of Tel Beer-Sheva analysis of the immediate roof (i.e. single layer) is only partially applicable, given the fact that at least a portion of the vertical load was transmitted vertically rather than laterally to the abutments. The stability of the laminated Voussoir is governed by similar processes: stability is achieved when shear resistance is sufficient to induce rotation of individual blocks close to the abutments. Then the global behavior of the layers is changed from a succession of layers each imposing vertical load on the layers below, to a coherent beam where loads are transformed laterally to the abutments. This transition is indicated by almost uniform deflection of the individual layers across the bulk of the sequence (Figure 6.18). Therefore the solution obtained by DDA using a single layer configuration seems to be unconservative, suggesting that a mult-layer analysis is warranted.

Chapter 7 - Stability Analysis of Underground Openings in Horizontally Stratified and Vertically Jointed Rock

7.1. Introduction

In the previous chapters the validation of DDA using analytical solutions, physical models, and a case study were discussed, and the advantages of DDA over the classic Voussoir model were shown. Furthermore, it was shown that DDA accounts for variations in joint spacing and shear resistance (friction) along joints, leading to different modes of failures and amount of deflection. Therefore, with given joint spacing and joint friction angle the stability of underground openings in discontinuous rock can be assessed.

Lee et al., (2003) showed that when two joint sets are encountered at a tunnel excavation face, the most critical joint combination consists of a set of horizontal joints (bedding planes) intersecting vertical joints. Furthermore, they have shown that the displacement of a key block at the roof tends to increase as the block size decreases. However, no particular reference is made by Lee et al., to joint spacing and tunnel dimensions.

This chapter explores the stability of underground openings excavated in horizontally stratified and vertically jointed rock masses. This study concentrates on:

1. The effect of joint spacing and shear resistance on the height of loosening above the excavation.
2. The relation between joint spacing and excavation span.

The paramount uncertainty associated with modeling discontinuous rock masses lies with the geometrical structure of the rock mass, e.g. joints length and spacing distributions. The main difficulty arises from the fact that most of the data regarding these parameters are collected either from boreholes or from limited surface exposures; in rare cases exploratory tunnels are excavated. The extrapolation from limited field data to a conceptual model of the rock mass and then to a numerical model introduces further uncertainties.

Joint spacing, defined as the perpendicular distance between two neighboring discontinuities, has been widely explored over the past three decades, and various techniques for data collection and analysis were proposed (refer to Priest, 1993). It was found that within a given joint set the joint spacing follows certain distribution laws, such as: normal, log-normal, and negative exponential among others. It has also been suggested that joint spacing is related to bed thickness, genesis, and geological setting (refer to Wu and Pollard, 1995). The distribution law reflects this, as well as the measuring and analysis technique. Similar findings were reported on issues of joint length (Zhang and Einstein, 1998; Mauldon, 1998).

In the current research the modeled rock mass is synthetic, with no reference to a particular, naturally occurring rock-mass. The discontinuous rock-mass was generated using the one-dimensional perturbation algorithm proposed by Shi and Goodman (1989). The algorithm inputs are: the average joint spacing S_j , the average joint length L_j , the average joint bridge B_j and the degree of randomness $0 < D_r < \frac{1}{2}$. When $D_r = \frac{1}{2}$ a full perturbation is applied, when $D_r = 0$ no perturbation is applied. The distribution function is assumed uniform, for simplicity.

7.1.1. Model geometry and mechanical properties

The analysis domain is 50m high and 40m wide. The opening geometry is of a horseshoe shaped tunnel (Figure 7.1), with span $B = 2a$ and height $h_t = b+c$. Fixed boundaries

are represented by four fixed blocks (each containing a minimum of three fixed points). Two joint sets are generated using the perturbation algorithm of Shi and Goodman (1989): a set of horizontal bedding planes and a set of vertical joints. The horizontal bedding planes are assumed of infinite extension, with average spacing of $S_j = 1m$ and degree of randomness of $D_r = 0.25$. The vertical joints are generated for different values of average spacing. The spacing, trace length, bridge length and degree of randomness are given in Table 7.1. Two different opening geometries are studied: 1) span $B = 10m$ and height $h_t = 10m$; and 2) span $B = 15m$ and height $h_t = 10m$. The analysis matrix is given in Table 7.1.

The vertical joints are generated such that the number of potential cantilever beams within the rock mass was minimized. Figure 7.2 shows a schematic representation of two types of rock masses: a) not containing cantilever beams; b) containing cantilever beams. The presence of cantilever beams reduces the displacements in the rock mass and enhances stability (Terzaghi, 1946). Therefore, in a rock mass not containing cantilevers the displacements are expected to be maximized.

Model	ϕ (°)	S_j (m)					D_r	L_j (m)	B_j (m)
B = 10m $h_t = 10m$	20	1.5	2	3	4	5	0	25	1
	30	1.5	2	3	4	5			
	40	1.5	2	3	4	5			
	50	1.5	2	3	4	5			
	60	1.5	2	3	4	5			
B = 15m $h_t = 10m$	20	2	3	4	5	6	0	25	1
	30	2	3	4	5	6			
	40	2	3	4	5	6			
	50	2	3	4	5	6			
	60	2	3	4	5	6			

Table 7.1. DDA modeling matrix.

The displacements within the rock mass are measured at seven measurement points along a vertical line rising from the excavation crown. The locations of the measurement points are given in Table 7.2.

Mechanical properties of the intact rock material are chosen to conform to “average” values of sedimentary rocks. The mechanical properties of the intact rock material and numeric control parameters are given in Table 7.3. The shear resistance along discontinuities was assumed purely frictional; cohesion and tensile strength are assumed zero. The discontinuities represent clean planar joints without surface roughness, wall annealing or infilling. The friction angle for bedding planes and vertical joints is assumed equal for simplicity; this is by no means limitation of the DDA method or its numeric implementation.

Measurement point	x,y coordinates (m)	Remarks
mp1	0, 0	excavation crown
mp2	0, 4.5	
mp3	0, 8.5	center of domain
mp4	0, 13.5	
mp5	0, 18	
mp6	0, 23	
mp7	0, 28	

Table 7.2 Locations of measurement points in DDA model. x,y coordinates are with respect to excavation crown.

Density	2500 kg/m ³
Elastic Modulus	10000 MPa
Poisson's ratio	0.25
Penalty stiffness ($g0$)	1000 MN/m
Time step size ($g1$)	0.0002 - 0.0004 sec ⁽¹⁾
Penetration control parameter ($g2$)	0.0002
Dynamic control parameter ($k01$)	1

Table 7.3. Material properties and numeric control parameters for DDA model. ⁽¹⁾ Time step size was adjusted to avoid numerical problems.

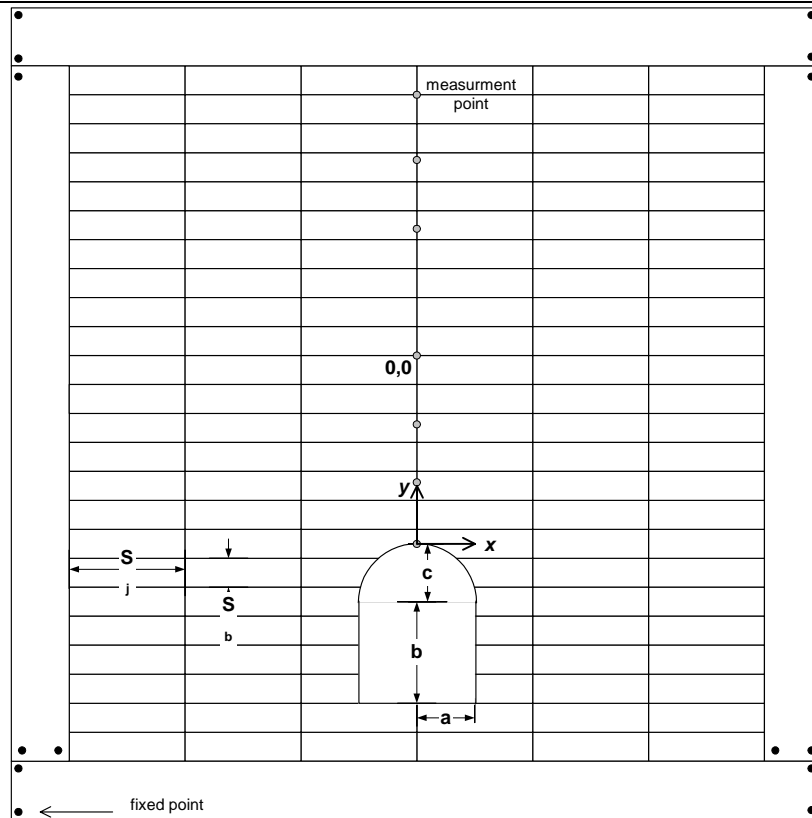


Figure 7.1. Geometry of the DDA model.

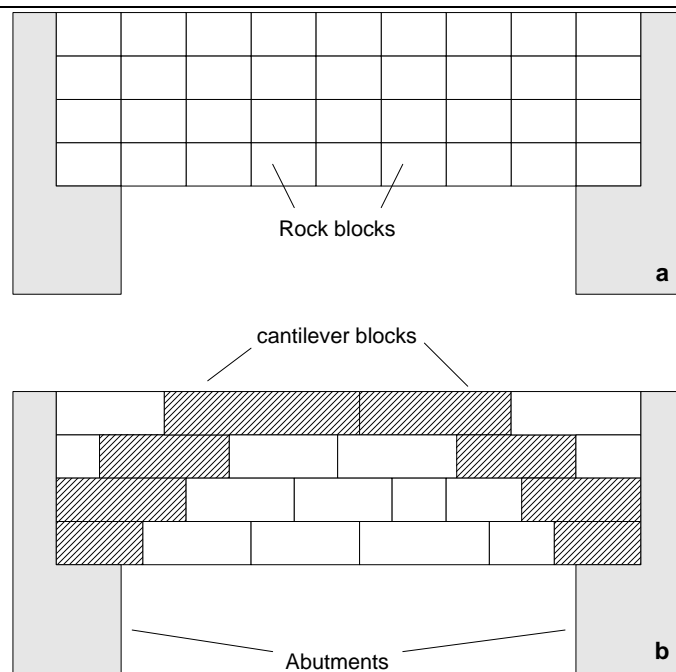


Figure 7.2. Two types of rock masses: a) not containing cantilever beams; b) containing cantilever beams.

7.1.2. Selection of contact stiffness

In sections 4.2, 5.3.3 and 6.6.1 it was shown that the accuracy of DDA solution depends on proper selection of numerical control parameters. Given a sufficiently small time step ($g1$) and penetration control parameter ($g2$), the nature of the DDA solution is determined by inter-block contact stiffness ($g0$). It was shown that when the number of blocks is large the contact stiffness should be chosen such that that convergence of numerical solution is achieved.

In the current model the maximum number of blocks for analysis was 1102 (for $S_j = 1.5 m$). A sensitivity analysis was performed for this specific geometric configuration. The maximum time step size was set to $g1 = 0.0004 sec$, the penetration control parameter was set to $g2 = 0.0002$, and the number of time steps was $n = 2500$. The contact stiffness was changed from $g0 = 250 MN/m$ to $g0 = 1000 MN/m$. The results of the sensitivity study are presented in Figure 7.3.

Figure 7.3a shows three time histories for different values of contact stiffness. When $g0 = 250 MN/m$ the solution is clearly non-converging within the time span, with a “wave length” of approximately 1500 time steps. Setting $g0 = 750 MN/m$ changes the solution; the oscillatory nature of an equilibrium solution is clearly visible. The “wave length” and amplitude of oscillations are reduced implying smaller initial perturbation and faster convergence. Increasing the contact stiffness to $g0 = 1000 MN/m$ enhances the convergence, and shows two pronounced modes of displacement. At the crown progressive deflection is taking place, while at all other measurement points the deflection attains equilibrium position.

Figure 7.3b shows the number of open close iterations over computation time. For $g0 = 250 MN/m$ the average number of iterations per time step is $i_{av} = 2.61$, for $g0 = 750 MN/m$ the average number of iterations is $i_{av} = 3.11$, and for $g0 = 1000 MN/m$ the average number of iterations is $i_{av} = 3.22$. Increasing the contact stiffness slightly impends on the numerical

efficiency. Based on these observations the contact stiffness value chosen for the analysis is $g_0 = 1000 \text{ MN/m}$.

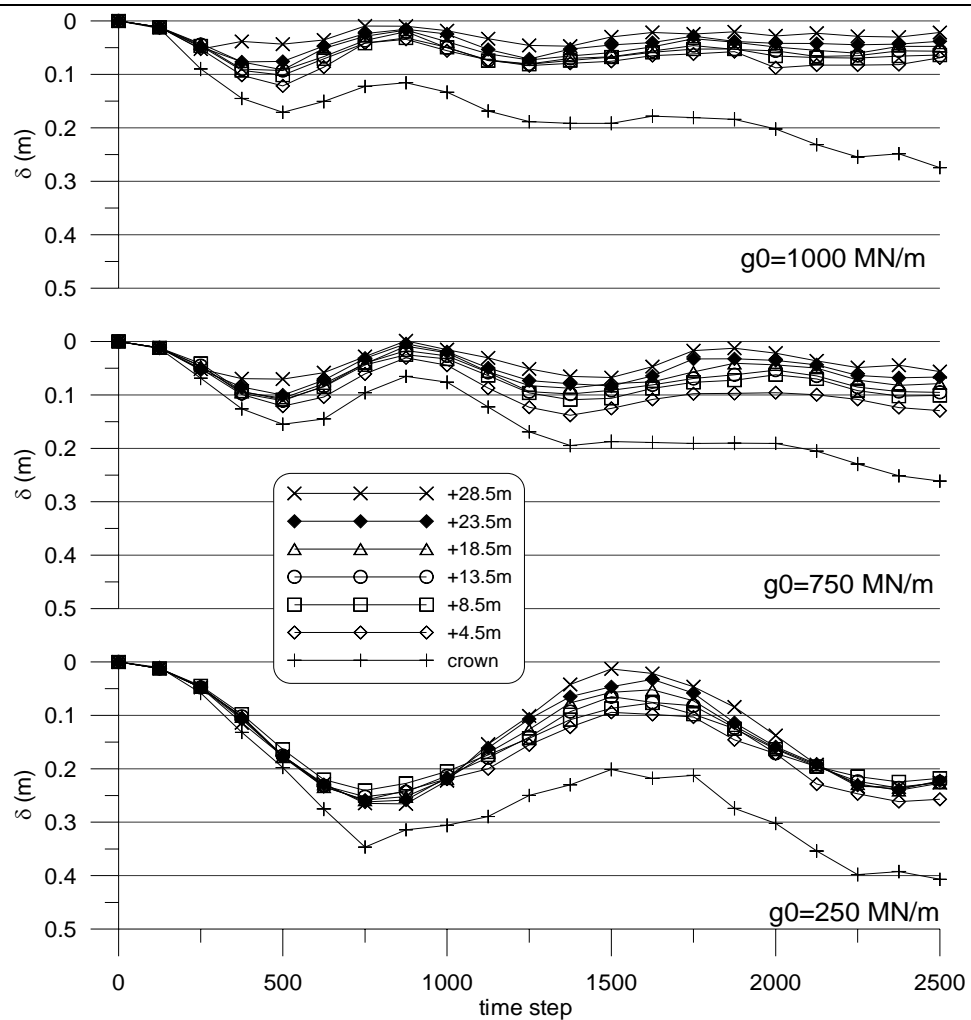


Figure 7.3. Contact stiffness sensitivity analysis for a DDA model of tunnel span $B = 10\text{m}$ and vertical joints spacing $S_j = 1.5$: a) vertical deflections (δ) for different values of. Maximum time step size to $g_1 = 0.0004 \text{ sec}$, penetration control parameter $g_2 = 0.0002$

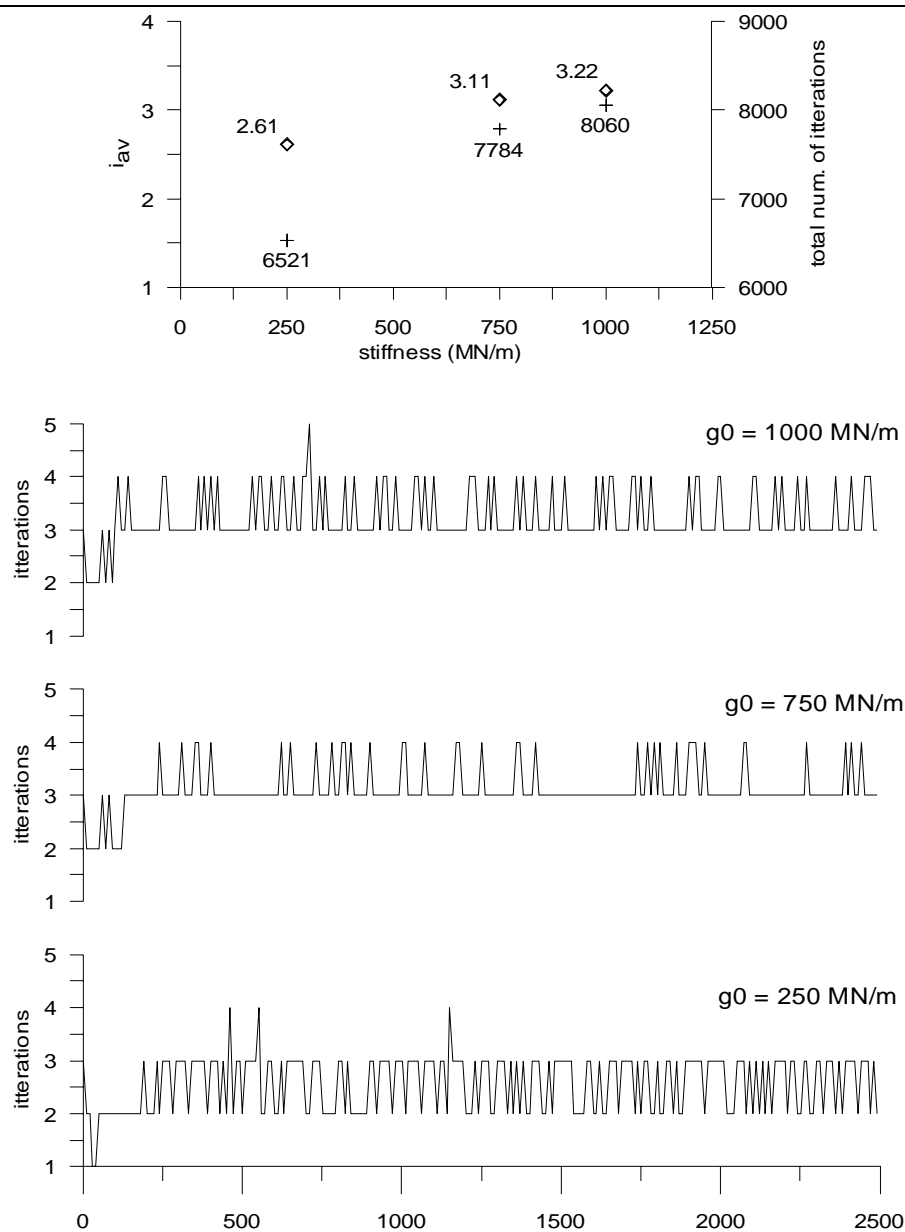


Figure 7.3. (cont.). Contact stiffness sensitivity analysis for a DDA model of tunnel span of $B = 10m$ and vertical joints spacing of $S_j = 1.5$: b) iteration time history for different values of contact stiffness.

7.1.3. Criteria for stable arching

The displacement curves in Figure 7.3a show two modes of deformation: 1) increasing displacement with time (measurement point 1); and 2) equilibrium position, after an initial

displacement marked by an oscillatory solution (measurement points 2-7). The nature of the oscillatory (equilibrium) solution was described in section 5.3.1, and it is defined here as the first criterion of stable arching.

DDA analysis of the laminated Voussoir beam (section 6.6.4) shows that stability is achieved when shear resistance is sufficient to induce rotation of individual blocks close to the abutments. The behavior of the layers is changed from a stack of beams each imposing vertical load on the underlying layers, to a coherent beam where loads are transferred laterally to the abutments. This transition is indicated by a nearly uniform deflection profile within the rock mass, leading to homogenization of displacements (Figure 6.18). This process is defined as the second criterion of stable arching.

Using these two criteria, the vertical extent of the loosened rock or the height of the arching zone can be determined. The height of the loosening zone is equivalent to Terzaghi's (1946) rock load, used for assessing rock loads on steel sets. The vertical extent of the loosening zone can be used for design of active support elements such as rock bolts.

7.2. Results

7.2.1. Roof span of 10m

Representative time histories of vertical displacements above the 10m wide opening are given in Figure 7.3a, which shows DDA results for joint spacing of $S_j = 1.5m$ and joint friction angle of $\phi = 20^\circ$. The crown of the excavation is in a state of progressive failure, which is clearly marked by the progressive downward displacement. The vertical displacements at points located at $y > 4.5m$ above the crown are oscillatory confined to values of $\delta < 0.1m$, thus implying stable arching.

When examining the DDA graphic output for this particular simulation, Figure 7.4, the inter-bed separation immediately above the crown is clearly visible. The separation dies out with vertical distance from the crown. An additional feature that must be noted is the failure of rock wedges created by the intersection of the discontinuities and the perimeter of the opening, clearly visible at the upper right part of the opening. These wedges can be found either by DDA or by analytical methods, such as Block Theory (Goodman and Shi, 1985). Failure of these wedges further reduces the stability of the crown by enlargement of the active span.

The vertical displacement (δ) profiles for the different values of joint spacing are given in Figure 7.5. The displacements are taken after 2500 time steps, which with a time step size of $\Delta t = 0.0004 \text{ sec}$ is equal to $t = 1 \text{ sec}$. For joint spacing of $S_j \leq 2m$ the displacement at the crown is $\delta_{y=0m} \approx 0.2 \text{ --} 0.3m$, depending on the available friction angle along the joints. The displacements die out with vertical distance from the crown, and at $y > 8.5m$ the displacements are reduced to values of $\delta_{y>8.5} < 0.1m$, approaching values of $\delta \approx 0.05m$. For joint spacing of $S_j \geq 3m$ the displacements are reduced to $\delta < 0.1m$, approaching values of $\delta \approx 0.05m$, and homogenization of displacements is evident.

Vertical displacement differences ($\Delta\delta/\Delta y$ where y is the vertical distance) calculated between pairs of measurement points within the vertical profile, are presented in Figure 7.6. For joint spacing of $S_j \leq 2m$ the displacement differences indicate that homogenization of displacements begins at $y > 4.5m$ above the crown, and that the difference approaches zero. For joint spacing of $S_j \geq 3m$ the displacement difference $\Delta\delta/\Delta y < 0.005$, with very little variation from the crown up.

From the described above it can be concluded that for a tunnel span of 10 meters the height of the loosening zone above the excavation is $h < 0.5h_t$ for joint spacing of $S_j \leq 2m$. For joint spacing of $S_j \geq 3m$ the rock mass above the opening attains stable arching. The rock mass

response is dictated by the joint spacing and to a lesser extent by joint friction, for the modeled range of friction angles. Only in one case, $S_j = 2m$ and $\phi = 60^\circ$, the friction angle inhibit excessive deflections and induce stable arching. Where the joint spacing is sufficiently large stable arching is independent of friction angle. The findings of this section are summarized in Table 7.4.

		Friction angle ($^\circ$)				
		20	30	40	50	60
Joint spacing (m)	1.5	< 0.45	< 0.45	< 0.45	< 0.45	< 0.45
	2	< 0.45	< 0.45	< 0.45	< 0.45	Stable
	3	Stable	Stable	Stable	Stable	Stable
	4	Stable	Stable	Stable	Stable	Stable
	5	Stable	Stable	Stable	Stable	Stable

Table 7.4. Normalized height of loosening zone ($h_r = h/h_t$) above an underground opening for a horseshoe tunnel of width $B = 10m$ and height $h_t = 10m$.

7.2.2. Influence of joint randomness

Modeling the transverse joints as long, perfectly persistent and with constant spacing results in a rock mass structure with a minimum number of cantilever blocks. In this configuration the deflections above the underground opening are expected to attain maximum values. However, joints are seldom persistent, and statistical variations are to be expected. In order to study the effect of joint variability on rock mass response the simulations for joint spacing of $S_j = 1.5m$ are repeated, with the following changes with respect to the transverse joints: trace length $L_j = 5m$, bridge length $B_j = 0.5m$ and degree of randomness of $D_r = 0.25$. All other mechanical and geometrical parameters are kept the same. The results of the simulations and comparison with the “uniform” simulation are presented in Figure 7.7. The graphic output of the simulation for friction angle along joints of $\phi = 20^\circ$ is given in Figure 7.8.

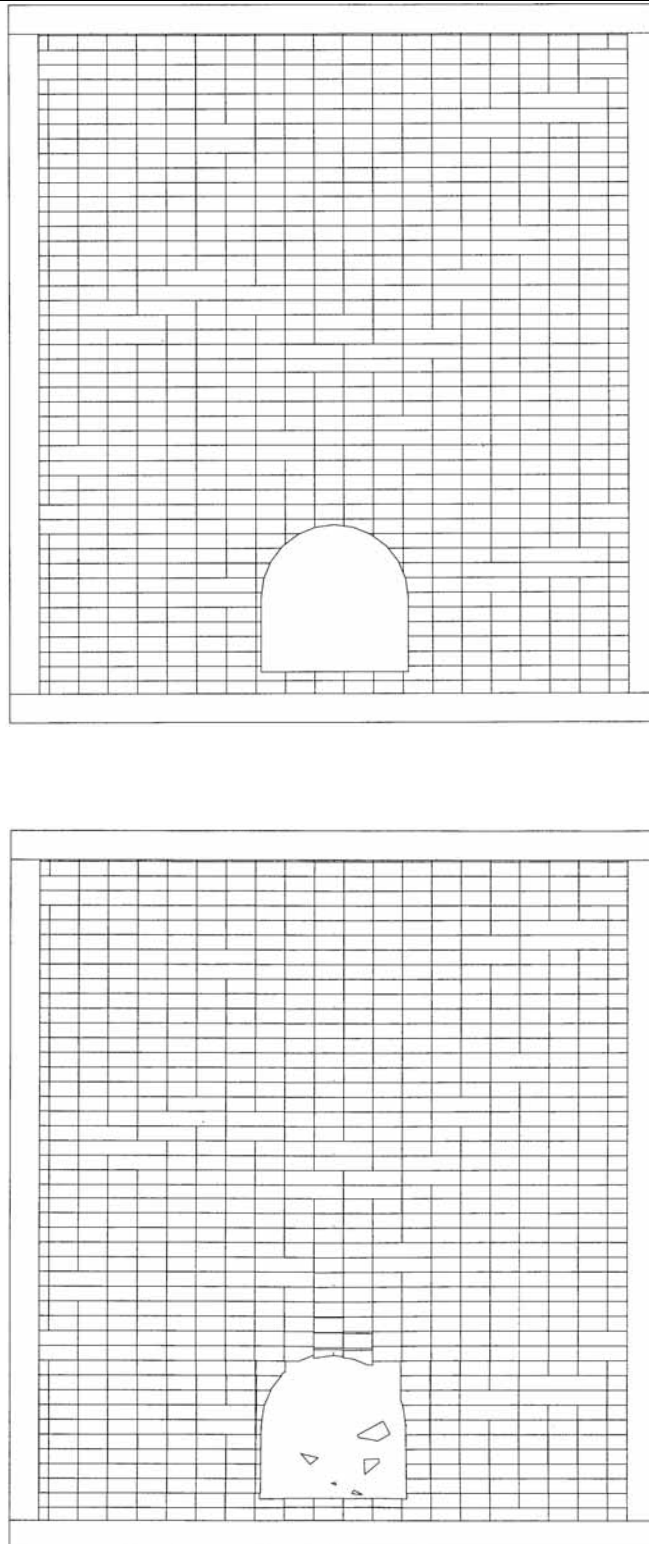


Figure 7.4. DDA graphic output for tunnel span of $B = 10m$ and vertical joint spacing of $S_j = 1.5$: a) initial configuration (top); b) deformed configuration (bottom).

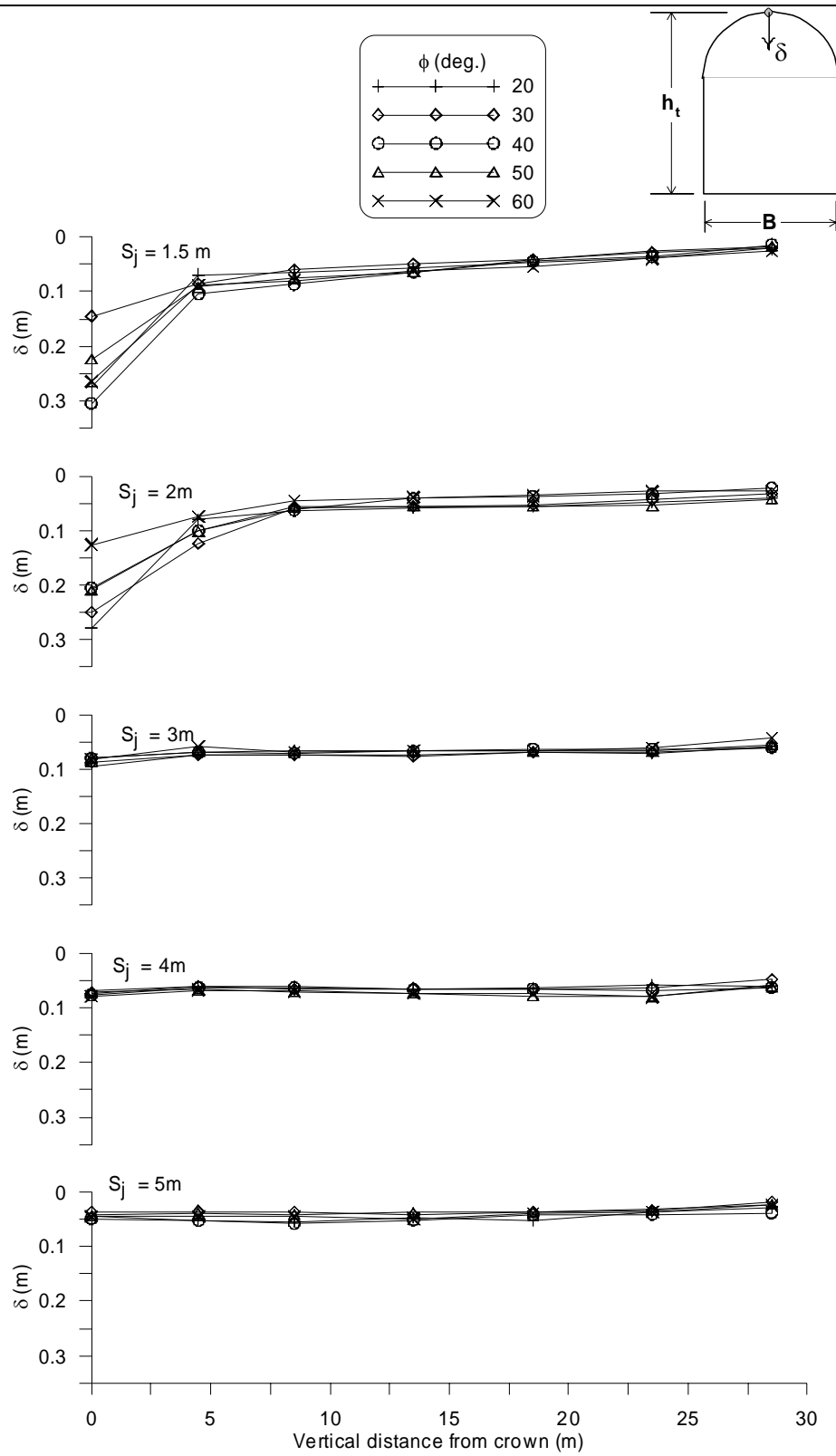


Figure 7.5. Vertical displacement (δ) profile above an underground opening of span $B = 10\text{m}$, for different values of joint spacing (S_j) and friction along joints (ϕ).

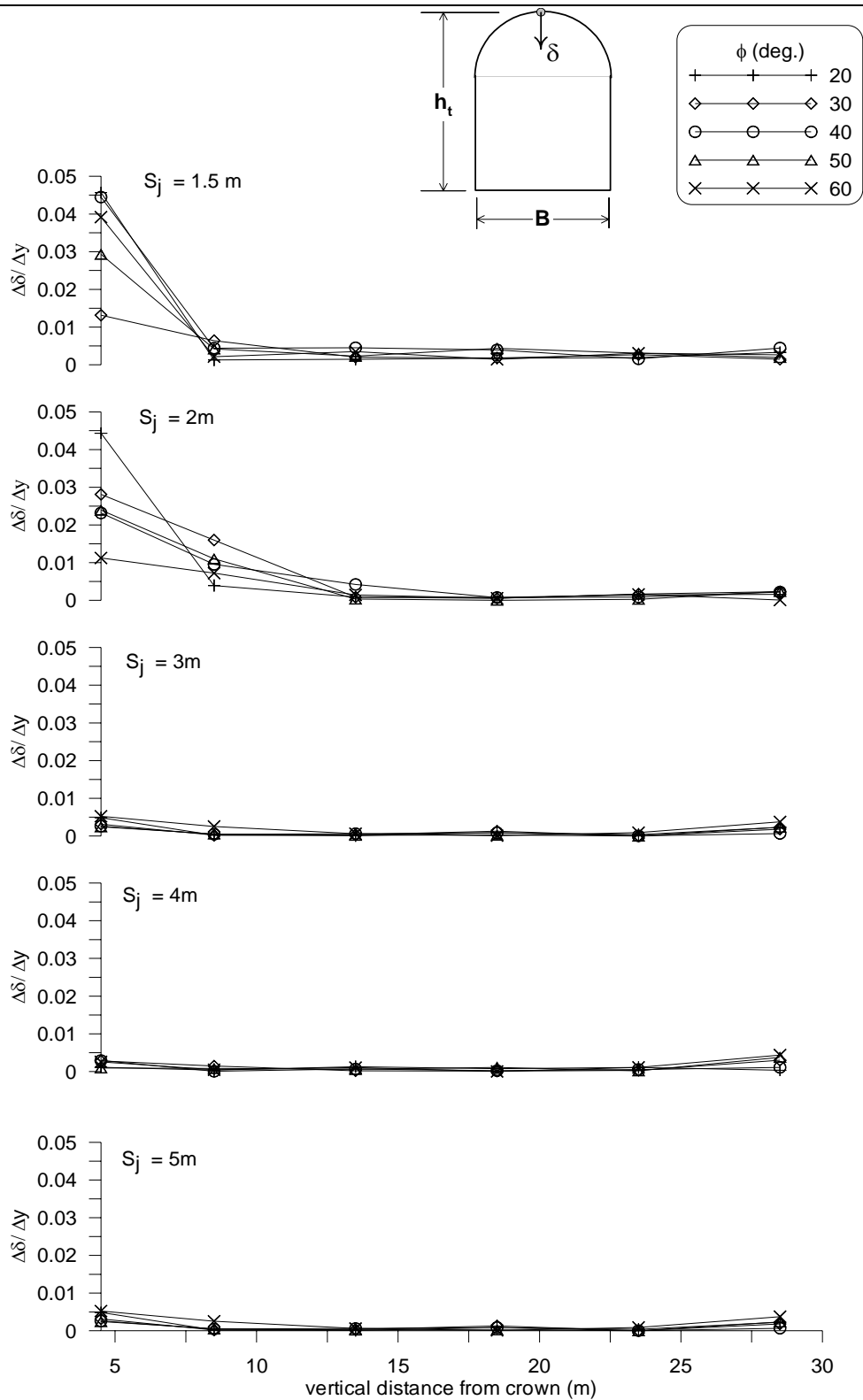


Figure 7.6. Vertical displacement difference ($\Delta\delta/\Delta y$) profile above an underground opening of span $B = 10m$, for different values of joint spacing (S_j) and friction along joints (ϕ).

Introduction of joint randomness reduces the vertical displacements. The downward crown displacement is reduced from $\delta_{y=0m} \approx 0.15 - 0.3m$, depending on the available friction angle along joints for non-random joints to $\delta_{y=0m} \leq 0.06m$ for the same opening geometry with random joint statistics, with no apparent influence of joint friction. The vertical displacement difference immediately above the crown is reduced from $\Delta\delta/\Delta y < 0.04$, depending on the available joint friction angle, to $\Delta\delta/\Delta y < 0.005$, with no apparent influence of joint friction.

The reduction of displacements and their homogenization, through the introduction of joint variability is attributed to the combined action of the following factors:

1. Nominal enlargement of joint spacing - resulting in enlargement of the Voussoir blocks and reduction of vertical displacements.
2. Presence of cantilever blocks – resulting in reduction of vertically transformed loads within the rock mass, refer to Terzaghi (1946).

The two configurations described can be regarded as the end-members of the modeled rock mass. The first end-member (uniform joints) is clearly conservative, whilst the second end-member (non-uniform joints) is less conservative. The initial value of joint spacing for the two realizations is $S_j = 1.5m$, which results in rather large Voussoir blocks and a relatively small number of blocks in a single beam. Thus, introduction of joint randomness and nominal enlargement of Voussoir blocks further improves the overall performance of the rock mass. However, when joint spacing is small and the number of blocks in a single beam is relatively large (as in the case of Tel Beer-Sheva) the influence of joint randomness on the overall performance of the rock mass is expected to be weaker.

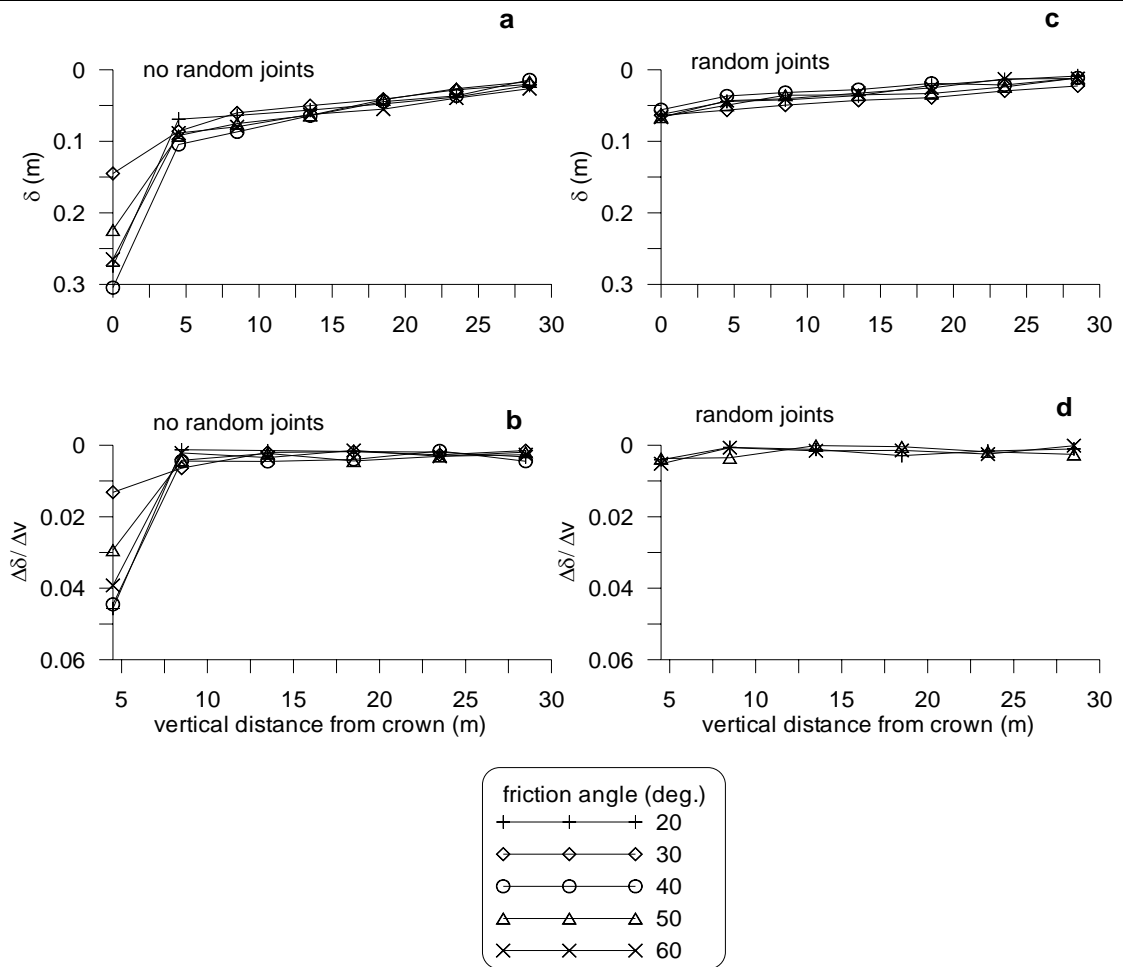


Figure 7.7. Rock mass response above an underground opening of span $B = 10m$, and joint spacing of $S_j = 1.5m$: a) vertical displacements - non-random ($D_r = 0$) joint configuration; b) vertical displacement difference - non-random joint configuration; c) vertical displacements – random ($D_r = 0.25$) joint configuration; d) vertical displacement difference - random joint configuration.

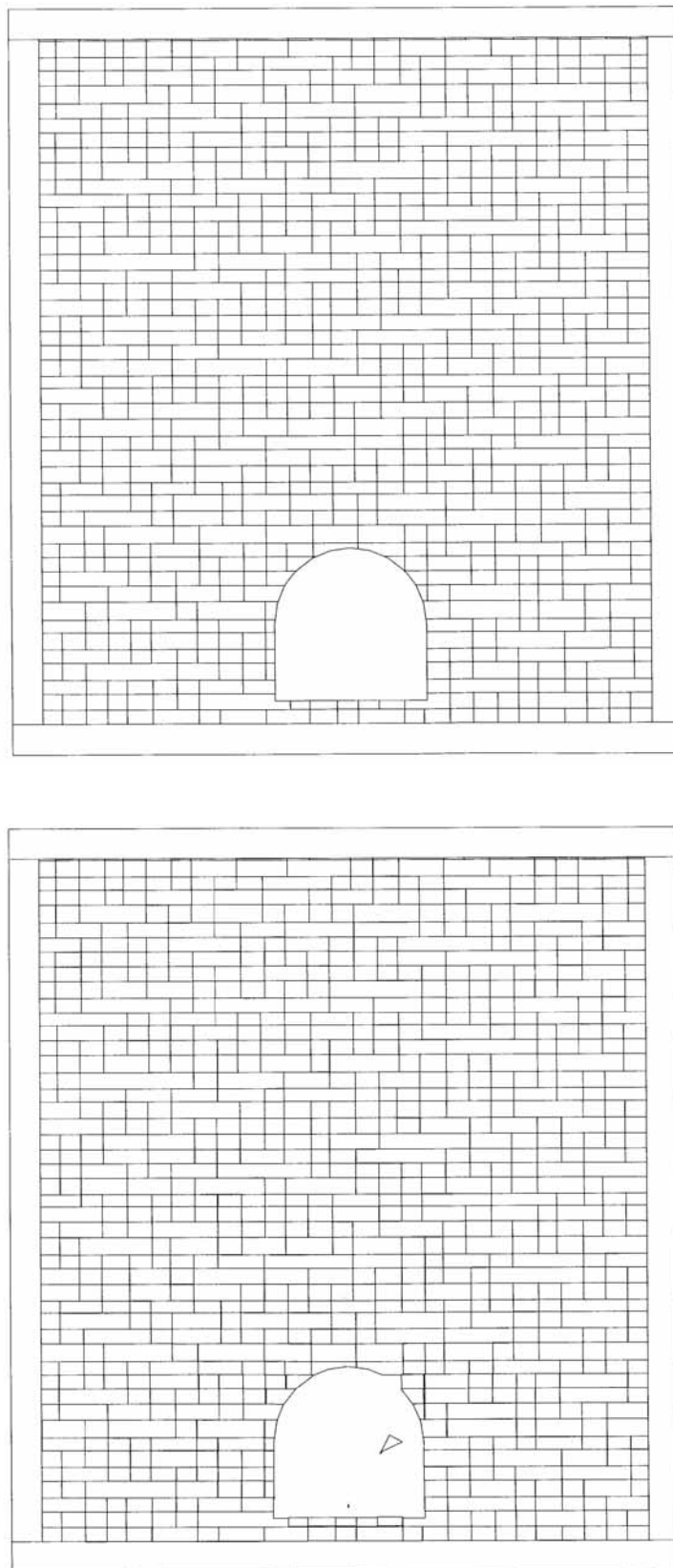


Figure 7.8. DDA graphic output for tunnel span of $B = 10m$, vertical joint spacing of $S_j = 1.5m$ with random statistics: a) initial configuration (top); b) deformed configuration (bottom).

7.2.3. Roof span of 15m

The vertical displacement profiles for the different values of joint spacing are given in Figure 7.9, and the displacement difference profiles are given in Figure 7.10. Clearly, enlarging the opening span by 50%, while keeping the height unchanged, modifies the rock mass response. For joint spacing of $S_j = 2m$ and friction angle of $\phi = 20^\circ$ the crown ($y = 0$) displacement is $\delta = 1.8m$, at $y = 4.5m$ the displacement is $\delta = -0.6m$, and approaching $\delta = 0.2m$ at $y > 25m$, which is the magnitude of crown displacement for opening span of $B = 10m$. The graphic output for this particular case is given in Figure 7.11. It is clearly seen that the rock mass immediately above the crown is sagging, and inter-bed separation is clearly present. The height of the loosening zone encompasses at least eight successive beds above the crown, compared with three successive beds for $B = 10m$ case (Figure 7.12). Furthermore, the larger span enhances failure of rock wedges formed by intersection of discontinuities and excavation perimeter. Increasing the joint friction angle reduces the overall displacements; the crown displacement for $\phi \geq 30^\circ$ is $\delta < 0.6m$, and approaches $\delta \approx -0.2m$ for $y > 4.5m$.

Enlarging the joint spacing to $S_j = 3m$ reduces the vertical displacements at the crown to $\delta = 0.54m$ for $\phi = 20^\circ$, $\delta = 0.38m$ for $\phi = 30^\circ$, and $\delta < 0.25m$ for $\phi \geq 40^\circ$. The displacements are reduced with vertical distance approaching $\delta = 0.1 m$. For joint spacing of $S_j \geq 4$ displacements are homogenized, decreasing with an increase in joint spacing to values of $\delta \approx 0.1 m$. Vertical displacement differences reveal similar trends: decreasing with increase of joint spacing, and homogenization of displacements for $S_j \geq 4$. The findings of this section are summarized in Table 7.5.

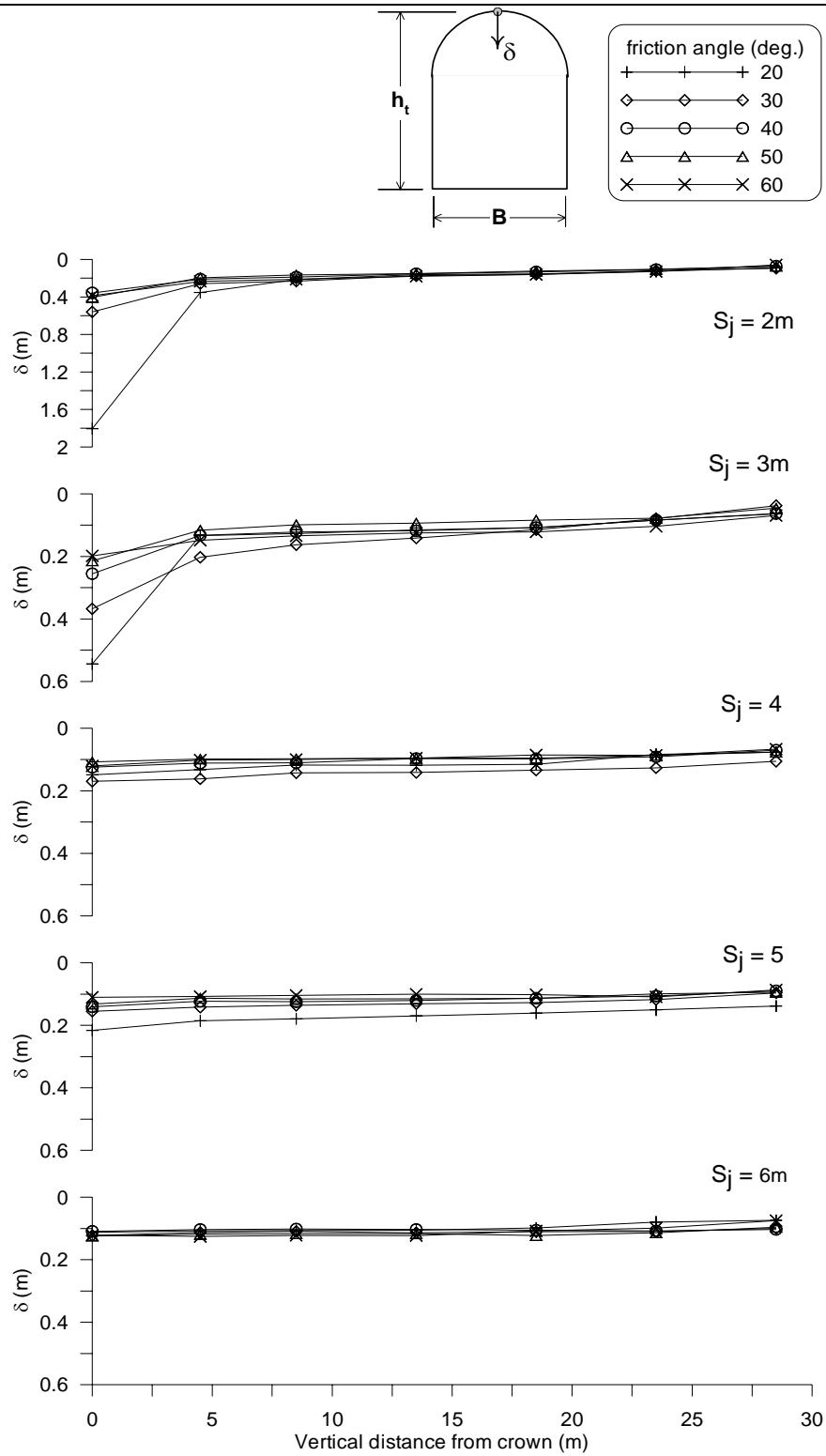


Figure 7.9. Vertical displacement (δ) profile above an underground opening of span $B = 15m$, for different values of joint spacing (S_j) and friction along joints (ϕ).

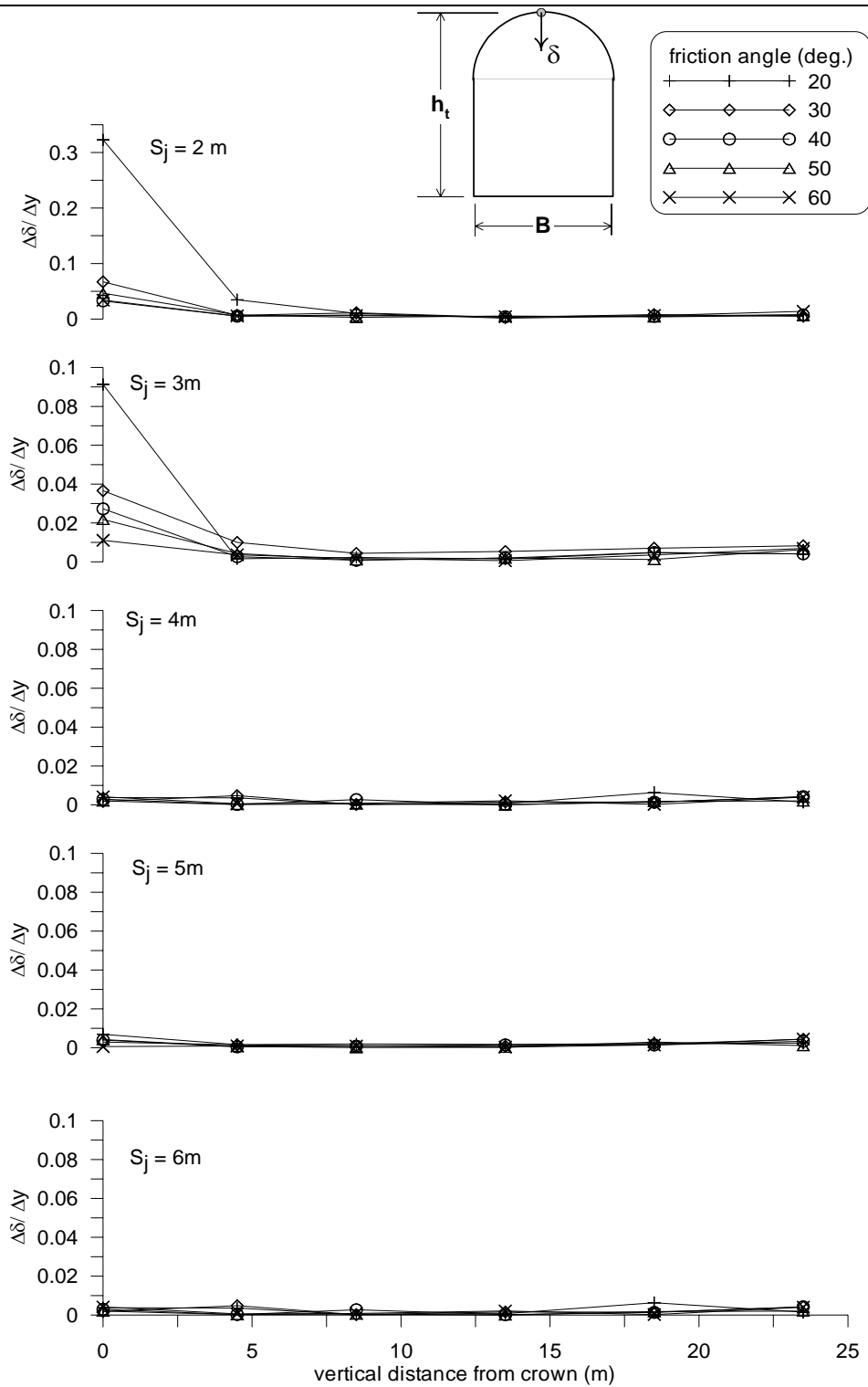


Figure 7.10. Vertical displacement difference ($\Delta\delta/\Delta y$) profile above an underground opening of span $B = 15m$, for different values of joint spacing (S_j) and friction along joints (ϕ).

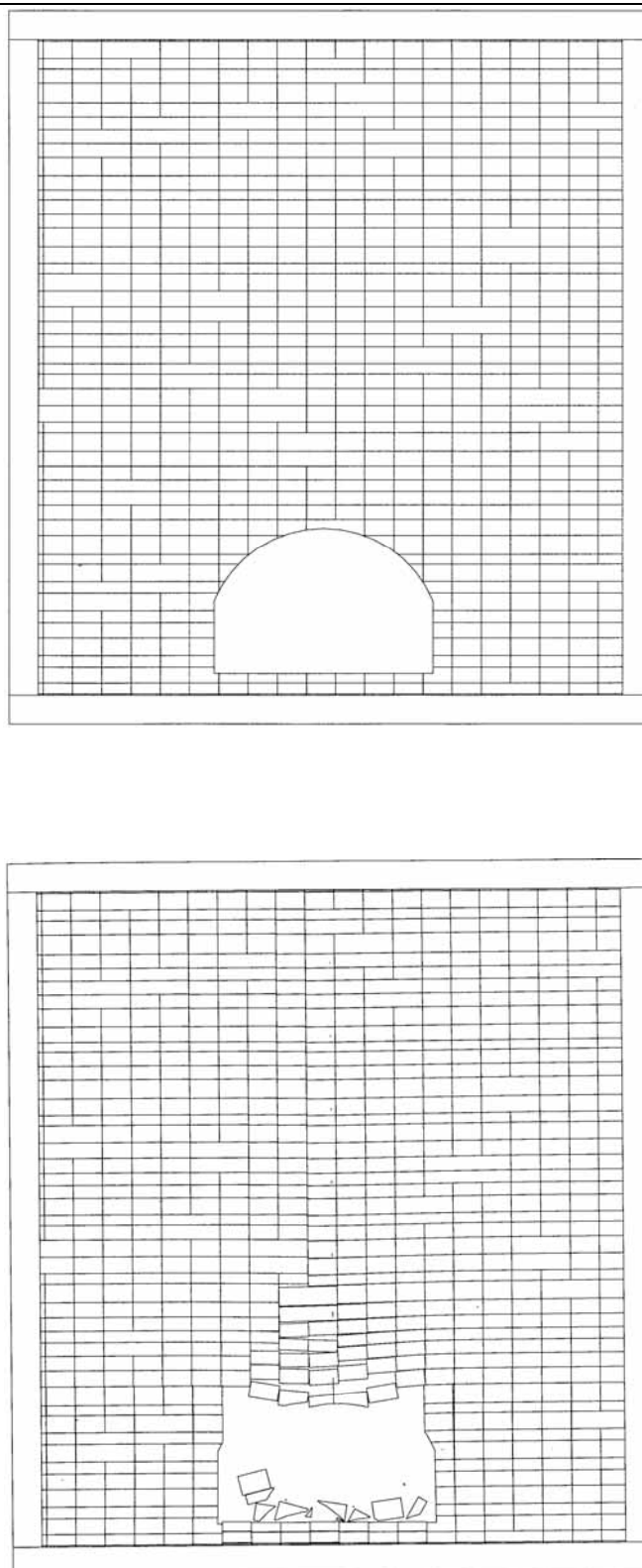


Figure 7.11. DDA graphic output for tunnel of span $B = 15m$, vertical joint spacing of $S_j = 2m$ and friction angle of $\phi = 20^\circ$: a) initial configuration (top); b) deformed configuration (bottom).

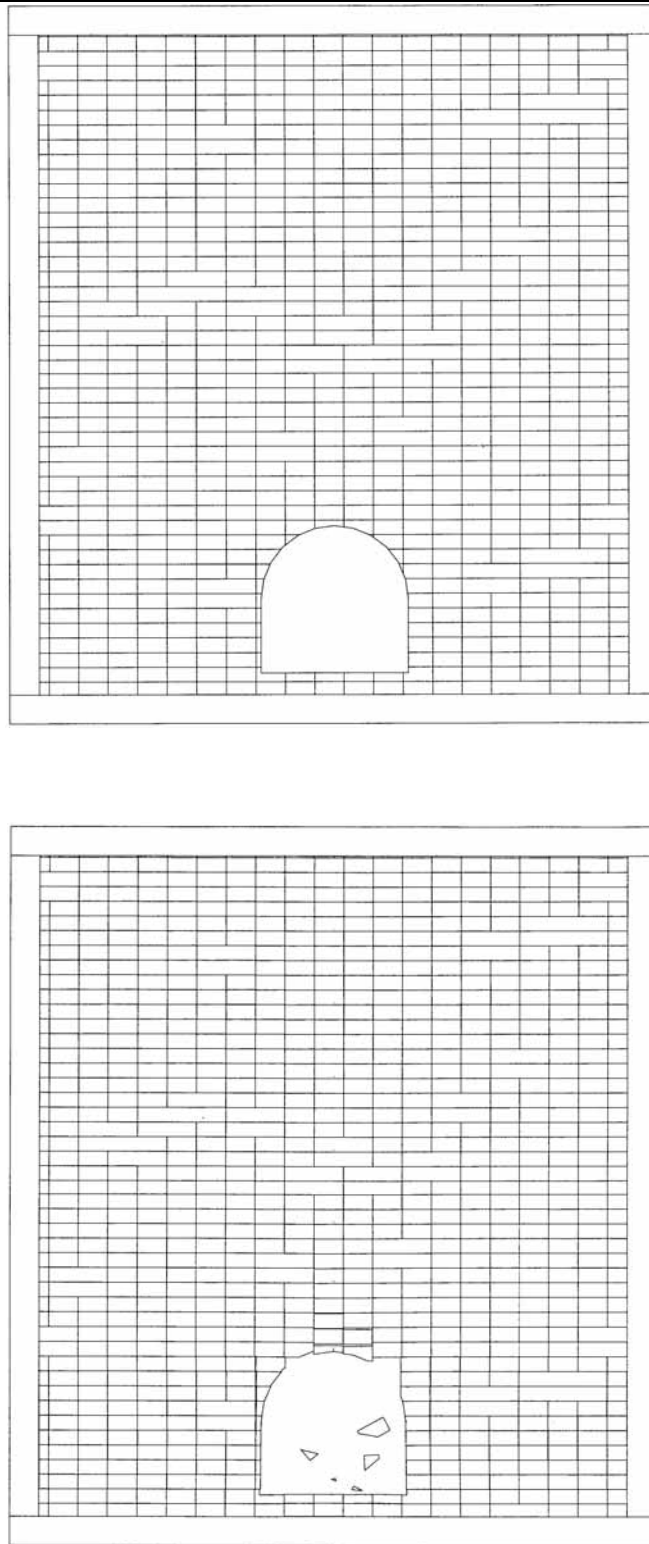


Figure 7.12. DDA graphic output for tunnel of span $B = 10m$, vertical joint spacing $S_j = 2$ and friction angle of $\phi = 20^\circ$ m: a) initial configuration (top); b) deformed configuration (bottom).

		Friction angle (°)				
		20	30	40	50	60
Joint spacing (m)	2	< 0.85	< 0.85	< 0.45	< 0.45	< 0.45
	3	< 0.85	< 0.85	< 0.45	< 0.45	< 0.45
	4	Stable	Stable	Stable	Stable	Stable
	5	Stable	Stable	Stable	Stable	Stable
	6	Stable	Stable	Stable	Stable	Stable

Table 7.5. Normalized height of loosening zone ($h_r = h/h_t$) above an underground opening, for a horseshoe tunnel of width $B = 15m$ and height $h_t = 10m$.

7.2.4. Rock mass response as a function of excavation span

In the previous sections the response of a rock mass with varying joint spacing around underground excavations of two different spans ($B = 10m$ and $15m$) was studied and described. The relation between joint spacing and span, however, was not explored. In this section two issues are addressed:

1. The joint spacing/ span size ratio (S_j/B) vs. vertical displacement δ .
2. The S_j/B ratio and the height of the loosened zone $h_r = h/h_t$ above an underground opening.

Figure 7.13 shows the normalized vertical displacement δ/B as a function of vertical distance from crown for $S_j/B = 0.2$, for both $B = 10m$ and $B = 15m$. Each of the five plots corresponds to a different value of joint friction angle. Plotting the displacement ratio $\delta_{B=15}/\delta_{B=10}$ (Figure 7.14) shows that for all modeled friction values the ratio is greater than unity and in most cases approaches 2. Similar analysis was performed for $S_j/B = 0.3$ and $S_j/B = 0.4$, for both $B = 10m$ and $B = 15m$. The displacement ratios are presented in Figure 7.14. The plot clearly shows that an increase of S_j/B ratio leads to convergence of the displacement ratio ($\delta_{B=15}/\delta_{B=10}$) to one.

The height of the loosening zone shows similar trends. When $S_j/B > 0.3$ the rock mass attains stable arching, regardless of the actual displacement (refer to Tables 7.4 and 7.5). For values of $S_j/B \leq 0.2$ the height of the loosening zone generally does not depend on friction angle or span, and is $h_r < 0.45$, with the exception of $h_r < 0.85$ for $\phi \leq 30^\circ$ and $B = 15m$.

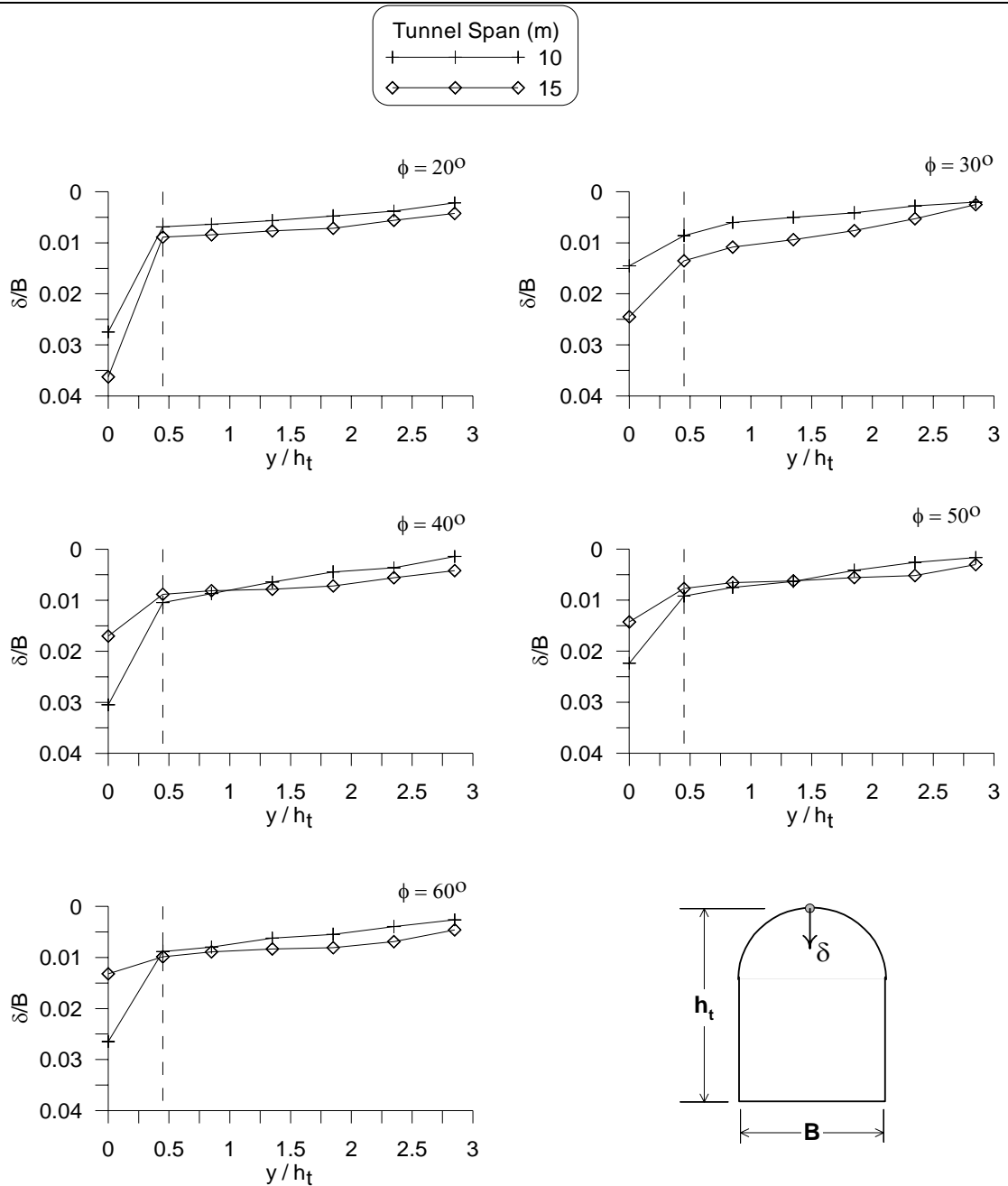


Figure 7.13. Normalized displacement δ/B for normalized joint spacing of $S_j/B = 0.2$.

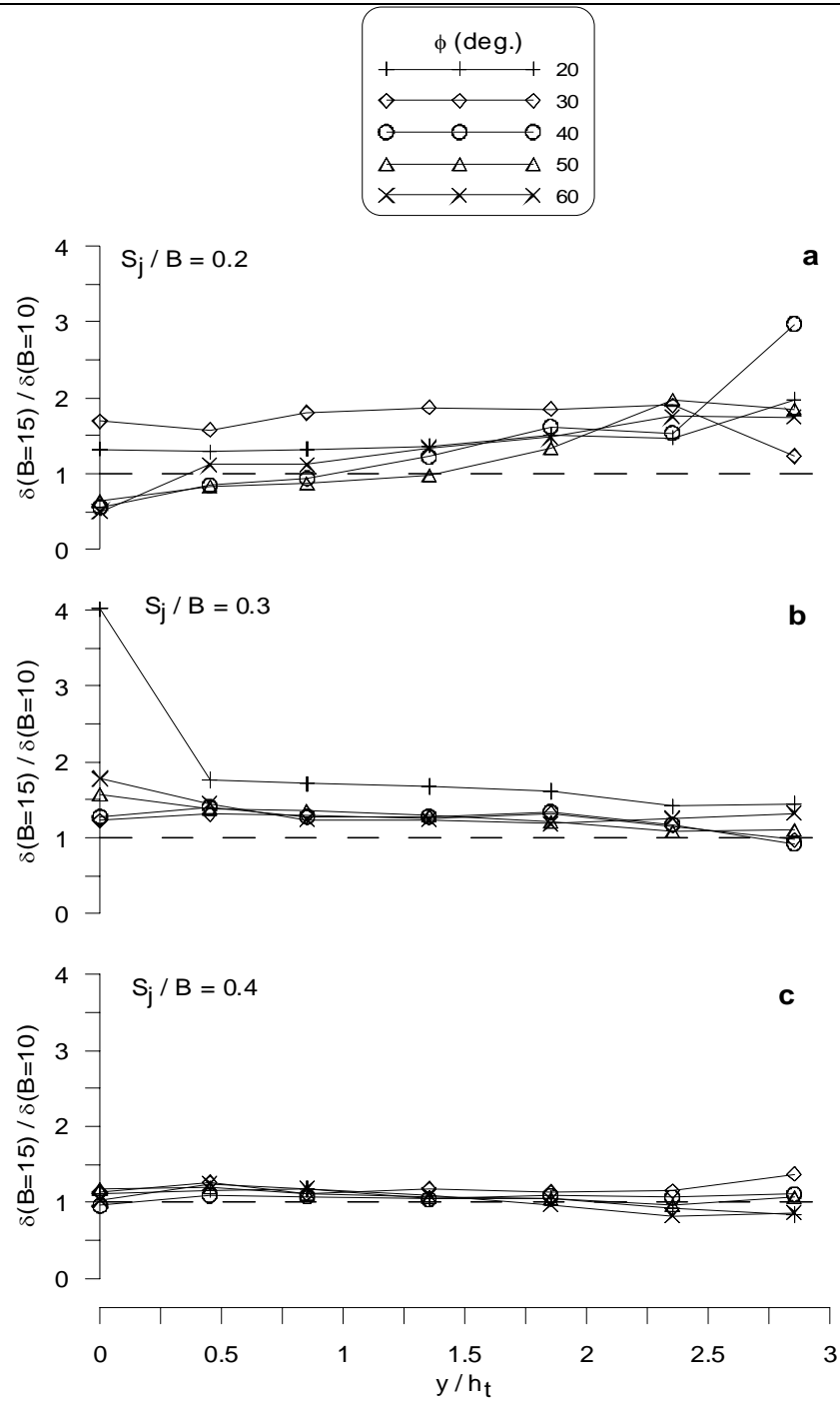


Figure 7.14. Vertical displacement ratio $\delta_{B=15}/\delta_{B=10}$: a) normalized joint spacing of $S_j/B = 0.2$; b) normalized joint spacing of $S_j/B = 0.3$; and c) normalized joint spacing of $S_j/B = 0.4$

7.3. Discussion

From the described above it can be concluded that for the modeled geometries the key factor controlling the stability of underground openings excavated in horizontally layered and vertically jointed rock mass is the spacing of vertical joints. The effect of friction along joints is secondary, and is evident only when vertical joint spacing is lower than a certain threshold. For underground openings with span of $B = 10m$ the threshold is $S_j \leq 2m$ ($S_j/B \leq 1/5$), whereas for openings with span of $B = 15m$ the threshold is $S_j \leq 3m$ ($S_j/B \leq 1/5$). These thresholds are functions of three factors: 1) joint spacing; 2) friction along joints; and 3) span opening.

When joint spacing is sufficiently large, the moments acting within each single block are equilibrated, consequently leading to stable arching. This mechanism is self-regulating and is independent of friction along joints. However, when joint spacing is below the threshold value ($S_j/B \leq 1/5$) the stability is determined by the interaction between joint spacing and friction along joints. For an underground opening of span $B = 10m$ and joint spacing of $S_j = 1.5m$ shear resistance along joints is not sufficient to preclude vertical displacements near the excavation crown, indicating that the arching mechanism is not fully developed. Stable arching is only met at $h > 0.45h_t$. For joint spacing of $S_j = 2m$ and friction angle of $\phi \leq 50^\circ$ stable arching is met at $h > 0.45h_t$, as well. However, when the friction along joints is $\phi = 60^\circ$ the shear resistance is sufficient to induce rotation of blocks and stable arching begins at the crown.

For an underground opening of span $B = 15m$ and joint spacing of $S_j \leq 3m$ the shear resistance is not sufficient to induce block rotations and stable arching at the crown. Stable arching is met at $h > 0.85h_t$ for $\phi \leq 30^\circ$ and $h > 0.45h_t$ for $\phi > 30^\circ$. When $S_j/B < 0.3$ the

height of the loosening zone is $h < 0.85h_t$, and in most cases is $h < 0.45h_t$. When $S_j/B > 0.3$ stable arching begins at the crown. These findings are summarized in Table 7.6.

S_j/B	h_r	Exceptions
≤ 0.2	$< 0.45h_t$	1. Stable arching for $B = 10m$ and $\phi = 60^\circ$ 2. $< 0.85h_t$ for $B = 15m$ and $\phi \leq 30^\circ$
0.3	0	Stable arching
0.4	0	Stable arching

Table 7.6. Normalized height of the loosening zone ($h_r = h/h_t$) above an underground opening for different values of joint spacing and opening span (S_j/B).

Given the modeled rock mass structure these estimates are clearly conservative. The synthetic rock mass is designed such that resistance to downward displacement is provided by shear resistance along joints, and that no cantilever beams are found within the rock mass. Cantilever beams are expected in a natural rock mass, where joint geometry is characterized by a certain statistical distribution. The presence of cantilever beams provides further resistance to downward displacement. This effect is discussed in section 7.2.2: a simple linear perturbation of joint spacing and bridge leads to reduction of vertical displacements and induces stable arching. In a similar configuration with uniformly distributed joints arching is achieved only at $h > 0.45h_t$. Given the uncertainties associated with rock mass geometry and its extrapolation, the extent of cantilever action cannot be easily quantified.

In this research the crushing strength of the rock was ignored, mainly since DDA is currently not capable of modeling stress concentrations. Crushing occurs mainly in deep excavations, in which the lateral compressive stresses are high. These stresses usually preclude rock mass loosening. Crushing also occurs in weak rocks. In excavations at shallow to moderate depths and competent rock, crushing failures are less common.

In terms of span B the height of the loosening zone is $h_r < 0.56B$ when $S_j/B \leq 0.2$. According to Terzaghi (1946) for tunnels excavated in a blocky rock mass (consists of chemically intact or almost intact rock fragments, which are entirely separated from each other and imperfectly interlocked) the expected overbreak ranges from $0.25B$ to $1.1(B+h_t)$, depending on the degree of jointing. However, a quantitative description of the degree of jointing is not given.

Rose (1982) revised Terzaghi's classification and described the degree of jointing in terms of Rock Quality Designation of RQD (Deere et al 1967). According to Rose for a moderately blocky rock mass ($RQD = 75-85$) the expected over break ranges from $0.25B$ to $0.2(B+h_t)$, whereas for a very blocky rock mass ($RQD = 30-75$) the expected over break is $(0.2 \text{ to } 0.6)(B+h_t)$. This reduction was achieved by ignoring the level of water table, which according to Brekke (1968) has little effect on rock load. The drawbacks of this revision are: 1) the friction along joints is neglected; 2) correlation with RQD .

RQD provides a quantitative estimate of rock mass quality from drill cores and is defined as the percentage of intact rock pieces longer than 10cm in the total length of the core. RQD is a directionally dependent parameter and its value may change considerably depending on the borehole orientation. In a horizontally layered and vertically jointed rock mass the RQD will be determined by the spacing between beds rather than the spacing of joints. Furthermore, RQD is not sensitive for spacing greater than 10cm. For example, a drill core of say 3m comprised of intact rock pieces each 10cm long will yield the same estimate as a similar drill core comprised of 3 pieces each 1m long. Therefore, correlation with RQD is problematic, especially for rock masses comprised of horizontal layers with vertical joints.

Comparison of the results of this research results with Terzaghi's prediction shows that the latter is conservative. Whereas Terzaghi's classification scheme lacks a consistent treatment of discontinuities, this research provides a systematic treatment of both joint

spacing and friction. Both joint spacing and friction angle along joints are easy to obtain parameters, either in the field or in laboratory. Therefore, a prediction based on these parameters is straightforward and explicit.

Chapter 8 – Conclusions

The purpose of this research was to study the stability of underground openings excavated in horizontally layered and vertically jointed rock masses using the Discontinuous Deformation Analysis (DDA) method. The objectives set forth in Chapter 1 of this thesis were: 1) validation of the numeric Discontinuous Deformation Analysis (DDA) using physical models and case studies; 2) investigation of the fractured beam kinematics; 3) development of simplified design charts and tables for assessment of rock loads in underground openings as function of joint spacing and joint friction angle.

DDA was validated using two different physical models: 1) shaking table model of a single block on an incline performed by Wartman (1999) at University of California at Berkeley; and 2) centrifuge model of a multi jointed single beam performed by Dr. M. Talesnick at the Technion. The case study of Tel Beer-Sheva, originally investigated by Hatzor and Benary (1998), was used to compare DDA and the classic Voussoir beam model, and to study the kinematics of single and multi-layered fractured beams. Finally, the general stability of underground openings excavated in a horizontally layered and vertically jointed rock mass was studied, with particular reference to: 1) vertical joint spacing; 2) joint friction angle; and 3) the relation between joint spacing and opening span.

8.1. DDA Limitations

In determining the applicability of DDA to a certain problem the assumptions and limitations of the method should be recognized. With respect to stability analysis of underground openings the following DDA limitations must be pointed out:

1. Two-dimensional formulation.
2. First order displacement approximation.

The reduction of three-dimensional field configurations to two-dimensional models and the extrapolation from two-dimensional models to three-dimensional engineering conditions is a known problem in rock engineering (Jing, 2003), and is beyond the scope of this thesis. At present the main limitations of three-dimensional modeling of a discontinuous rock mass are: the lack of maturity of three-dimensional models, and the requirement for excessive computing power when modeling full-scale problems with a large number of discrete blocks. A two-dimensional formulation provides computationally effective approximation to three-dimensional engineering situations, it also facilitates large simulations and elaborate sensitivity analysis.

DDA's first order displacement approximation results in constant strain elements. Thus, stress concentrations within the blocks are not modeled, nor is material damage. This limitation is acute when modeling highly stressed rock masses, such as in deep excavations, or when modeling deformation in weak rock. However, these particular conditions are not relevant to the cases investigated here. The reported results are applicable to moderately shallow excavations, where the ambient stresses are low, and rock is relatively strong. In such environments deformation is primarily achieved through rock block displacements rather than by material damage.

8.2. DDA Accuracy

The accuracy of the DDA solution is determined by four control parameters:

1. Maximum time step size ($g1$).
2. Penetration control parameter ($g2$).
3. Contact spring stiffness ($g0$).
4. Dynamic control parameter ($k01$).

The control parameters $g1$ and $g2$ are interrelated; suitable guidelines for individual and independent choice of each are not presented here. Throughout this research these parameters were chosen to be of the same magnitude, for simplicity. It was found that given sufficiently small $g1$ and $g2$, the accuracy of DDA is controlled by the value of the contact stiffness (the penalty). The proper combination of these three control parameters insures proper conditioning of the global stiffness matrix (i.e. diagonal dominance) and in turn assures convergence of the solution. The influence of the dynamic control parameter $k01$ is discussed in section 8.3.

8.3. DDA Validation

When DDA solution is compared with analytical solutions for the block on an incline problem the relative numeric error is found to be below 1.5%, indicating that block contact algorithm in DDA is an accurate replication of the analytical model for frictional sliding. When compared with a shaking table model for a block on an incline (Wartman, 1999) the DDA solution is found to be conservative. The solution accuracy is improved by reducing the dynamic control parameter, thus accounting for: 1) strain rate dependencies shown by the particular interface used in this model; 2) difference between the numerical and physical

behavior at contact points during shaking; 3) lack of a physically sound energy dissipation algorithm in DDA. It was found that a reduction of the inter time step velocity by 2% (setting $k01 = 0.98$) improves both the ultimate accuracy and the kinematics of the DDA solution.

The main source of DDA numeric error is the initial perturbation of contact forces associated with initial gravitational loading (Yeung, 1991; Doolin and Sitar, 2002). The implicit time marching scheme of DDA (Newmark, 1959) dissipates this initial perturbation through algorithmic damping, as the computation evolves with time. The magnitude of initial perturbation, and consequently the numeric error, is inversely proportional to the contact stiffness value. High contact stiffness results in lower initial perturbation and faster convergence rate. An alternative strategy for enhancement of convergence is by introduction of “kinetic damping”, namely reduction of inter time step transferred velocity. This strategy is recommended when the mechanical system modeled is expected to attain equilibrium position, or when the mode of failure is independent of system geometry, such as in block sliding models. However, it should be remembered that “dynamic damping” is a numerical manipulation, which is not related to a specific physical energy dissipation mechanism.

Validation of DDA using the block on an incline models, both analytical and physical, is of prime importance to problems of slope stability, and as general benchmark tests for DDA accuracy. However, they are of a limited applicability to underground openings, which requires validation under more complex block contact conditions. During block sliding the relative position of contacts is changed with time, but the contacts between the blocks, and consequently contact forces and stresses within the blocks, are unchanged. This is not the case for jointed beams spanning an underground opening. During beam deformation some of the original contacts are expected to disappear while new contacts are expected to form, leading to changes of contact forces between blocks and consequently of stresses within the blocks.

Centrifuge modeling of a multi-jointed rock beam comprised of six individual blocks, showed that stable arching was achieved mainly through rotation of the external blocks. DDA simulation of this particular model shows that stable arching is achieved through rotation of stresses within the blocks, rather than by physical rotation of the external blocks. The displacements predicted by DDA are found to be excessive, whereas the lateral forces measured at the abutment are found to conform. The discrepancy between DDA and the centrifuge models results from the geometrical Constraints of the DDA model. Whereas in the centrifuge model the frictional interfaces allow block rotation, in the given DDA model the infinitesimal thickness of the joints inhibits significant block rotation.

DDA analysis of a multi jointed rock beam, comprised of 32 individual blocks, shows that given sufficient rotational freedom the deformation mode found in the centrifuge model is replicated by DDA. The excessive rotations of the external blocks induce stable arching. It is found that the transition from shear along abutments to block rotation and stable arching is a function of the available shear resistance along joints. Given sufficient shear resistance, the external blocks undergo rotation, which is found to be significantly larger when compared to blocks found in the center of the beam. Otherwise, the external blocks shear along abutments, and the magnitude of block rotations are found to be similar across the beam, indicating that stable arching is not achieved.

Back analysis of an ancient roof failure in an underground water reservoir excavated in horizontally layered and densely fractured rock mass, show that DDA successfully predicts the anticipated failure. Back analysis of the ancient failure using the classic Voussoir model shows that for the given rock mass this model was unconservative. The DDA model of the particular excavation roof shows that within the layered roof the vertical loads transferred are vertically from the upper stack to the lower members. The underlying assumption in the Voussoir model, of complete detachment of the lower beam, is not satisfied in this case,

resulting in unconservative prediction regarding roof stability. It is found that in layered rock masses the transition from unstable deformation to stable arching was marked by the homogenization of vertical displacements within the rock mass, and that this transition is a function of both transverse joint spacing and shear resistance along joints.

A DDA model of a multi-block system requires careful conditioning of the numeric control parameters, since high contact stiffness impedes on solution convergence. Throughout this research, it is found that contact stiffness is not associated with joint normal or tangential stiffness, but rather is a numeric parameter. It is found that most accurate results are obtained when contact stiffness lies between 10^2 MN/m to 10^3 MN/m, and the amplification factor g_0/E , where E is the block elastic modulus, is ranging from 0.05 to 1. When the contact stiffness exceeds 10^3 MN/m the convergence of the solution rapidly deteriorates. Doolin and Sitar (2003) reported that for the block on an incline problem the DDA solution converges for amplification factors ranging from 0.1 to 100, and that the relative numeric error decreases for higher penalty values. Given that the initial perturbation is inversely proportional to the contact stiffness, the contact stiffness should be chosen such that both accuracy and convergence are not compromised. For multi-block systems it is recommended that contact stiffness should not exceed block material elastic modulus and that with increasing number of blocks it should be decreased, until the solution converges.

8.4. Stability of Underground Openings in Horizontally Stratified and Vertically Jointed Rock

The stability of underground openings excavated in a horizontally layered and vertically jointed rock mass is studied using two different geometric configurations: 1) excavation span $B = 10m$; and 2) excavation span $B = 15m$, for different values of transverse joint spacing and friction angle along joints. A total number of 50 individual simulations is presented. It is

found that the height of the loosening zone above an underground excavation is determined mainly by the ratio between joint spacing and excavation span (S_j/B). When $S_j/B \leq 0.2$ the height of the loosening zone is found to be smaller than $0.5B$, with the exception of $B = 15m$ and $\phi \leq 30^\circ$ where the height of the loosening zone extends to $0.85B$. When $S_j/B \geq 0.3$ the rock mass above the excavation attains stable arching, reducing the loosening to unstable wedges formed by the intersections of preexisting joints and the excavation perimeter.

The height of the loosening zone is inversely proportional to joint density. When the number of blocks per beam (reciprocal to S_j/B) is greater than five ($S_j/B \leq 0.2$) the beam tends to deform by inter-block shear, while rotation is minimal. Consequently, the driving moment generated by the vertical couple, including the vertical surcharge, is not equilibrated by resisting moment generated by the lateral thrust, thus leading to progressive failure. When the number of blocks per beam is equal or less than three ($S_j/B \geq 0.3$), increased rotation generates an effective lateral couple within each block, and the beam attains stable arching, after initial deflection. For $S_j/B = 0.3$ the expected deflection of the excavation crown is $\delta \approx 0.01B$, whereas for $S_j/B = 0.4$ the expected deflection of the excavation crown is $\delta \approx 0.0075B$.

These results are obtained for a synthetic rock mass constructed such that the number of cantilever beams within it is minimal, achieved using constant joint spacing and long traces. The reported displacements are therefore assumed to be conservative when compared to naturally occurring rock masses. Introduction of simple variation algorithm on to the joint generation routine reduces the displacements. This reduction is expected to attain maximum effect for smaller values of joint spacing, since joint variability increases the nominal length of the individual blocks and the “interlocking” within the rock mass.

Terzaghi's rock load classification predicts that for a blocky rock mass the over break height above the excavation ranges from $0.25B$ to $1.1(B+h_t)$, depending on the degree of jointing. However, the degree of jointing is not quantified, and guidelines for assessing the

degree of jointing are not provided. Rose's revision (1982) limits the over break from $0.25B$ to $0.6(B+h_j)$, correlating the degree of jointing to RQD. The correlation between RQD and joint spacing is ambiguous and can be misleading. In this research the expected over break is correlated with joint spacing. It is found that the expected over break ranges from $0.45B$ to $0.85B$ for $S_j/B \leq 0.2$, depending on the joint friction angle.

Terzaghi's classification scheme lacks a consistent treatment of discontinuities. This research provides a systematic treatment of both joint spacing and friction, which are readily attainable parameters, either in the field or in laboratory. Therefore, a prediction based on these parameters is straightforward and explicit.

8.5. Recommendations for Future Research

With reference to the main goal of this research, stability of underground openings in a horizontally layered and vertically jointed rock mass, future research should address the following issues and their effect on the stability of underground openings excavated in such a rock mass:

1. The influence of block length to thickness ratio.
2. Different mechanical lithologies.
3. The effect of in-situ stresses, with special reference to deep excavations.
4. The effect of cohesion and tensile strength along bedding planes and joints.
5. Interaction of the rock mass and active support.

In this research the bedding planes are modeled as horizontal and the transverse joints as vertical. This geometry is naturally occurring, however not exclusive. Other common rock masses exhibit non-horizontal layering and inclined transverse joints. Previous research (e.g.

Lee et al., 2003) addressed the issue of joint inclination, without special reference to joint spacing and shear resistance along joints. Future research should address the effect of joint spacing and shear resistance along joints and bedding planes for different rock mass geometries.

Future validation of DDA should focus on comparison between DDA models and full scale engineering cases in complex geologic settings where rock mass deformation was monitored and documented at complex geological settings. Successful comparison should bring DDA's potential to fulfillment, and transform it into an attractive analysis tool for the practicing engineer.

Appendix – Classic Voussoir Solution

The following is based on the original formulation of Evans (1941), modified and corrected by Beer and Meek (1982). Configuration of the Voussoir beam and the notations are given in Figure A1.

The basic assumptions of the analysis are:

1. The ground above the roof is completely distressed in the direction normal to bedding.
2. The rock mass has parted along smooth bedding plane breaks forming a series of beams.
3. The beam consists of no-tension material and the distribution of compressive stress at the center and the abutments are linear.

The lateral couple formed by beam deflection equilibrates the overturning gravitational-reaction couple

$$(A1) \quad \frac{W}{2} \cdot \frac{S}{4} = ZT$$

where W is the weight of the beam, S is the beams span, T is the axial thrust and Z is the lever arm.

The structure presented in Fig. A1a is statically indeterminate since the lever arm Z is not known. Assuming a parabolic reaction arch of length L and thickness $n \cdot t$ Eq (A1) can be written as

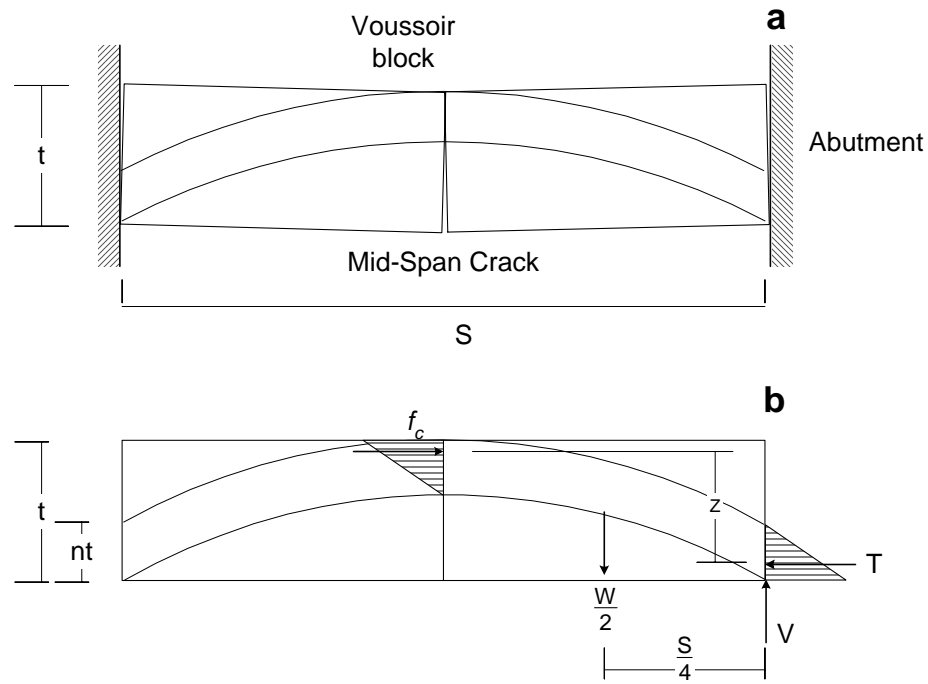


Figure A1. a) Voussoir beam conceptual model; b) Voussoir beam notation.

$$(A2) \quad \frac{\gamma S^2}{8} = \frac{f_c n Z}{2}$$

where γ is beam unit weight.

The initial moment arm Z_0 is given by

$$(A3) \quad Z_0 = t \left(1 - \frac{2}{3}n\right)$$

The length of the reaction arch L is given by

$$(A4) \quad L = S + \frac{8Z_0^2}{3S}$$

When the beam deforms the compression arch will shorten by

$$(A5) \quad \Delta L = \frac{f_{av}}{E} L$$

where E is the beam elastic modulus and f_{av} is the average stress along the compression arch, given by

$$(A6) \quad f_{av} = \frac{f_c}{2} \left(\frac{2}{3} + \frac{n}{2} \right)$$

The new moment arm will be

$$(A7) \quad Z = \sqrt{\frac{3S}{8} \left(\frac{8Z_0^2}{3S} - \Delta L \right)}$$

Shortening of the arch changes the internal load distribution in the beam. The new thinness of the compressive arch is given by

$$(A8) \quad n = \frac{2}{3} \left(1 - \frac{Z}{T} \right)$$

As previously mentioned the structure is statically undetermined, therefore a complete explicit solution of the final deformation and state of loading in the beam is not available.

An iterative solution technique, based on the relaxation method was introduced by Brady and Brown (1985). The relaxation starts from an assumption of load/depth ratio n , from which the initial moment arm can be calculated (Eq. A3). The various beam load and deformation parameters can be calculated directly:

$$(i) \quad f_c = \frac{\gamma S^2}{4nz}$$

$$(ii) \quad f_{av} = \frac{f_c}{2} \left(\frac{2}{3} + \frac{n}{2} \right)$$

$$(iii) \quad L = S + \frac{8Z^2}{3S}$$

$$(iv) \quad \Delta L = \frac{f_{av}}{E} L$$

$$(v) \quad Z = \sqrt{\frac{3S}{8} \left(\frac{8Z_c^2}{3S} - \Delta L \right)}$$
 where Z_c is the value of Z from

the previous computational cycle.

$$(vi) \quad n = \frac{2}{3} \left(1 - \frac{Z}{t} \right)$$

The solution procedure involves sequential calculation of Eq. (i) to (v). Each cycle of computation produces a new value of n , which is then introduced in to Eq. (i) to restart the solution cycle. Iterations of the solution sequence are continued until stable values of f_c and n are obtained. Stable solution for n is attained for minimum value of f_c .

The factor of safety with respect to crushing at abutments ant at mid-span is given by

$$(A9) \quad F.S._{crushing} = \frac{UCS}{f_c}$$

where UCS is unconfined compressive strength. Factor of safety with respect to vertical sliding along abutments and joints is given by

$$(A10) \quad F.S._{shear} = \frac{T \tan \phi}{V} = \frac{f_c n}{\gamma S} \tan \phi$$

where ϕ is friction angle.

References

- Amadei, B., Lin, C., Dwyer, J. 1996. Recent extensions to the DDA method. In: Reza Salami, M., Banks, D. eds. *Proceedings of the First International Forum on Discontinuous Deformation Analysis (DDA) and Simulations of Discontinuous Media*, Berkley, California. TSI Press, Albuquerque. pp 1-30.
- Barton, N., Lien, R., Lunde, J. 1974. Engineering classification of rock masses for the design of tunnel support. *Rock. Mech. Rock. Eng.* 6: 189-236.
- Beer, G. and Meek, J.L. 1982. Design curves for roofs and hanging walls in bedded rock based on voussoir beam and plate solutions. *Trans. Inst. Min. Metal.* 91, A18-22.
- Benari, R. 1996. *Stability of underground openings in jointed chalky rock - a case study from Tel Beer-Sheva*. M. Sc. Thesis, Department of Geological and Environmental Sciences. Ben Gurion University of the Negev. (in Hebrew)
- Bieniawski, Z. T. 1973. Engineering classification of jointed rock masses. *Trans. S. Afr. Inst. Civ. Eng.* 15: 335-344.
- Brady, B. H. and Brown, E. T. 1985. *Rock mechanics for underground mining*. 1st ed., George Allen and Unwin, London. 527 pp.
- Brekke, T. L. 1968. Blocky and seamy rock mass in tunneling. *Bull. Assoc. Eng. Geologist.* 5 (1).
- Bucky, P. B. 1931. Use of models for the study of mining problems. *Am. Inst. Min. Met. Eng. Tech. Pub.* 425, 28pp.
- Bucky, P. B. and Taborelli, R. V. 1938. Effects of immediate roof thickness in longwall mining as determined by barodynamic experiments. *Trans. Inst. Min. Metal.* 130: 314
- Chen, G. Miki, S. and Ohnishi, Y. (1996) Practical improvements to DDA. In: Reza Salami, M. & Banks, M. (eds.). *Proceedings of the Firth International Forum on Discontinuous Deformation Analysis (DDA) and Simulation of Discontinuous Media*. 97-110. TSI Press: Albuquerque.
- Chugh, A. K. 1977. Stability analysis of jointed beam. *Int. J. Numer. Ana. Methods Geomech.* 1: 323-341.
- Cundall, P. A. (1971). A computer model for simulating progressive, large scale movements in blocky rock system. *Symposium of International Society of Rock Mechanics*, Nancy, France. pp 11-18.

- Deere, D. U., Hendron, A. J., Patton, F. D., and Cording, E. J. 1967. Design of surface and near-surface construction. In: C. Fairhurst (ed.) *Failure and Breakage of Rock*. Society of Mining Engineers of AIME, New York.
- Desai, C. S., Zamman M. M., Lightner, J. G., Siriwardane, H. J. 1984. Thin layer element for interfaces and joints. *Int. J. Numer. Anal. Methods Geomech.* 8:19–43.
- Diederichs, M. S. and Kaiser, P. K. 1999a. Stability of large excavations in laminated hard rock masses: the voussoir analogue revisited. *Int. J. Rock. Mech. Min, Sci.* 36: 97-117.
- Diederichs, M. S. and Kaiser, P. K. 1999b. Authors' reply to *Discussion* by A.L. Sofianos *Int. J. Rock. Mech. Min, Sci.* 36 (7):995-997
- Doolin, D and Sitar, N. (2002) Displacement accuracy of Discontinuous Deformation Analysis applied to sliding block. *Journal of Engineering Mechanics*, ASCE. 128(11): 1158-1168.
- Economopoulus, J. N., Sofianos, A. I., Koronakis, N. J. 1994. Voussoir beam response of bedded limestone roofs in Greek underground mining excavations. *Proceedings of the International Congress on Tunneling and Ground Conditions*, Nasr City, Cairo, Egypt. pp 223-229.
- Evans, W. H. 1941. The strength of undermined strata. *Trans. Inst. Min. Metal.* 50: 475-500.
- Fayol, M. 1885. Sur les mouvements de terrain provoques par l'exploitation des mines. *Bull. Soc. Indust.* 14:818.
- Ghaboussi, J., Wilson, E. L., Isenberg, J. 1973. Finite element for rock joints and interfaces. *J. Soil Mech. Div. ASCE* 99, SM10:833–848.
- Goodman, R. E. 1989. *Introduction to rock mechanics*. 2nded. John Wiley & Sons. 562 pp.
- Goodman, R. E. and Seed H. B. (1965) Earthquake induced displacements in sand embankments. *J. Soil Mech. and Foundations Div. ASCE.* 92(SM2): 125 – 146.
- Goodman, R. E. and Shi, G-H. 1985. *Block theory and its application to rock engineering*. Prentice – Hall, New Jersey. 338p.
- Goodman, R. E., Taylor, R. L., Brekke, T. L. 1968. A model for the mechanics of jointed rock. *Journal of the Soil Mechanics Division*, ASCE. 94 (SM3): 637-659.
- Hatzor, Y. H. and Benary, R. 1988. The stability of a laminated voussoir beams: back analysis of a historic roof collapse using DDA. *Int. J. Rock. Mech. Min, Sci.* 35(2): 165-181.

- Hatzor, Y. H. and Feintuch, A. (2001) The validity of dynamic block displacement prediction using DDA. *Int. J. of Rock Mech. and Min. Sci.* 38: 599 – 606.
- Heyman, J. 1982. *The masonry arch*. Prentice Hall. 133 pp.
- Hsiung, S-M. 2003. Discontinuous Deformation Analysis (DDA) with nth order polynomial displacement functions. in: Elsworth, D., Tinucci, J. P., Heasley, K. A. (ed.). *Proceedings of the 38th US Rock Mechanics Symposium*.
- Jing L, Ma Y, Fang Z. 2001. Modeling of fluid flow and solid deformation for fractured rocks with discontinuous deformation analysis (DDA) method. *Int. J. Rock Mech. Min. Sci.* 38(3):343–55.
- Ke. T-C. and Bray, J. D. 1995. Modeling of particulate media using discontinuous deformation analysis. *J. Engrg. Mechanics*. ASCE. 121(11): 1234 – 1243.
- Kim, J., Bray, J. D., Reimer, M. F., Seed. R. B. (1999) *Dynamic interface friction properties of geosynthetics*. Unpublished report, University of California at Berkeley, Department of Civil Engineering.
- Koo, C. Y. and Chern, J.C. 1996. The development of DDA with third order displacement functions. In: Reza Salami, M., Banks, D. eds. *Proceedings of the First International Forum on Discontinuous Deformation Analysis (DDA) and Simulations of Discontinuous Media*. Berkley, California. TSI Press, Albuquerque . 342-349.
- Lauferr, H. 1958. Gebirgsklassifizierung fur den Stollenbau. *Geologie und Bawesen*. Vol. 24, No 1: 46-51.
- Lee, D-H., Choo, S-K., Hong, C-S., Park, Y-J, Kim, G-J. 2003. A parametric study of the discontinuity in rock mass and its influence on tunnel behavior. *Proceedings of the 10th ISRM Congress*. South African Institute of Mining and Metallurgy. 745 – 748.
- Lemos, J. V., Hart, R. D., Cundall, P. A. 1985. A generalized distinct element program for modeling jointed rock mass. In: Stefanson, O. ed. *Proceedings of International Symposium on Fundamentals of Rock Joints*. 335-343.
- MacLaughlin, M. (1997) *Discontinuous Deformation Analysis of the kinematics of rock slopes*. Ph.D. thesis, Department of Civil Engineering, University of California, Berkley.
- Mauldon, M. 1998. Estimating mean fracture trace length and density from observations in convex window. *Rock. Mech. Rock. Eng.* 31(4): 201-216.
- McBride, A. and Scheele, F. (2001) Investigation of discontinuous deformation analysis using physical laboratory models. In: Bicanic, N. (ed.). *Proc. of the Fourth International Conference on Discontinuous Deformation Analysis*. 73-82.

- Newmark, N. M. (1959) A method of computation for structural dynamics. *J. of the Eng. Mech. Div. ASCE* . 85(EM3)
- Nomikos, P.P., Sofianos, A. I., and Tsoutrelis, C. E. 2002. Symmetric wedge in the roof of a tunnel excavated in an inclined stress field *Int. J. Rock. Mech. Min. Sci.*39 (1): 59-67
- O’Sullivan, C. and Bray, J. D. (2001) A comparative evaluation of two approaches to discrete element modeling to particulate media. In: Bicanic, N. (ed.). *Proceedings of the Fourth International Conference on Discontinuous Deformation Analysis*. Glasgow, Scotland. 97-110.
- Obert, L. and Duvall, W. I. 1976. *Rock mechanics and the design of structures in rock*. 1st ed. John Wiley. 650 pp.
- Pacher, F., Rabcewicz, L. and Golser, J. 1974. *Zum der seitigen Stand der Gebirgsklassifizierung in Stollen-und Tunnelbau*. Proc. XXII Geomech. colloq., Salzburg, 51-58.
- Passaris, E. K. S., Ran, J. Q., Mottahed, P. 1993. Stability of the jointed roof in stratified rock. *Int. J. Rock. Mech. Min, Sci. Geomech. Abstr.* 30(7): 857-860.
- Pender, M. J. 1985. Prefailure joint dilatancy and the behavior of a beam with vertical joints. *Rock. Mech. Rock. Eng.* 18: 253-266.
- Polishook, B. and Flexer, A. 1998. Assessment of chalk rock mass in excavation. *Bull. Eng. Geol. Env.* 57: 145-150.
- Polishook, B. 1995. *Geological and geomechanical properties of chalk and their influence on underground structures*. Ph.D. Thesis. Tel Aviv University. (in Hebrew).
- Priest, S. D. 1993. *Discontinuity analysis for rock engineering*. Chapman and Hall. 47 pp.
- Ran, J. Q., Passaris, E. K. S., Mottahed, P. 1994. Shear sliding failure of the jointed roof in laminated rock mass. *Rock. Mech. Rock. Eng.* 27(4): 235-251.
- Riedmüller, G. and Schubert, W. 1999. Critical comments on quantitative rock mass classifications. *Felsbau*. 17(3): 164-167.
- Rose, D. 1982. Revising Terzaghi’s tunnel rock load coefficients. In: Goodman, R. E. and Hueze, F. (eds.). *Proceedings of the 23rd Symposium on rock Mechanics*. Berkeley, California. Society of Mining Engineers, AIMMP. 951-960.
- Sepehr, K., and Stimpson, B. 1988. Roof deflections and sag in jointed horizontally bedded strata – a numerical study. *Rock. Mech. Rock. Eng.* 21: 207-218.

- Sheorey, P.R. 1994. A theory for in situ stresses in isotropic and transversely isotropic rock. *Int. J. Rock Mech. Min. Sci. & Geomech. Abstr.* 31(1), 23-34.
- Shi, G-H. 1988. *Discontinuous Deformation Analysis – a new numerical method for the statics and dynamics of block system*. Ph. D. Thesis, Department of Civil Engineering, University of California, Berkley. 378p.
- Shi, G-H. 1993. *Block System Modeling by Discontinuous Deformation Analysis*. Topics in Engineering Vol. 11, Computational Mechanics Publications. 209p.
- Shi, G-H. and Goodman, R. E. 1989. The key block of unrolled joint traces in developed maps of tunnel walls. *Int. J. Numer. Ana. Methods Geomech.* 13: 131-158.
- Shingi, M. Ohno, H. Otsuka, Y. and Ma, G. (1997) Viscosity coefficient of the rock fall simulation. In. Ohnishi, Y (ed.). *Second International Conference on Analysis of Discontinuous Deformation*. Kyoto, Japan 201-210.
- Sofianos , A. I. 1996. Analysis and design of underground hard rock voussoir beam roof. *Int. J. Rock. Mech. Min. Sci.* 33(2): 153-166.
- Sofianos, A. I. 1999. Discussion of the paper by M.S. Diederichs and P.K. Kaiser "Stability of large excavations in laminated hard rock masses: the voussoir analogue revisited. *Int. J. Rock. Mech. Min. Sci.* 36(7): 991-993.
- Sofianos, A. I., Kapenis, A. P., Rogakis, C. 1998. Voussoir beam analysis of underground marble quarry. In: Rosmanith, H. P. ed. *Mechanics of jointed and Faulted rocks*. Balkema. 515-520.
- Sofianos, A. I. and Kapenis, A. P. 1998. Numerical evaluation of the response in bending of an underground hard rock voussoir beam roof. *Int. J. Rock. Mech. Min, Sci.* 35(8): 1071-1086.
- Sterling, R. L. 1980. The ultimate load behavior of laterally constrained rock beams. In: Summers, D. A. ed. *The state of the art in rock mechanics, Proc. 21st US Symp. Rock Mech. University of Rolla, Missouri.* 533-542.
- Talesnick, M.L. and Hatzor, Y. H. (in press). Determination of interface parameters between rock blocks in centrifuge models. *Int. J. Rock. Mech. Min. Sci.*
- Taylor, R. N. 1995. *Geotechnical centrifuge technology*. Blackie Academic and Professional, Glasgow. pp 296.
- Terzaghi, K. 1946 Rock defects and loads on tunnel support. In: Proctor, R. V., White, T., eds. *Rock tunneling with steel supports*. Commercial School and Stamping Co, Youngstown. pp 15-99.
- Timoshenko, S. and Goodier, J. N. 1951. *Theory of Elasticity*. Engineering Societies Monographs. McGraw-Hill. 1951.

- Tsesarsky, M. and Hatzor, Y. H. 2000. Stability of large span, shallow underground openings in soft discontinuous chalk. *Proceedings of the Eurock 2000 Symposium*, Aachen, Germany. 427-432.
- Wang, C-Y., Chuang C-C. and Sheng, J. 1996. Time integration theories for the DDA method with Finite Element meshes. In: Reza Salami, M. & Banks, M. (eds.). *Proceedings of the Firth International Forum on Discontinuous Deformation Analysis (DDA) and Simulation of Discontinuous Media*. 97-110. Berkeley, California. TSI Press: Albuquerque.
- Wartman, J. 1999. *Physical model studies of seismically induced deformation of in slopes*. Ph. D. Thesis, Department of Civil Engineering, University of California, Berkley.
- Wartman, J., Bray, J. D. and Seed, R. B. 2003. Inclined plane studies of the Newmark sliding block procedure. *Journal of Geotechnical and Geoenvironmental Engineering, ASCE*. 129 (8): 673-684.
- Wright, F. D. 1972. Arching action in cracked roof beams. *Proceedings of the 5th Int. Strata Control. Conf.* 29: 1-9.
- Wright, F. D. 1974. *Design of roof bolt patterns for jointed roof*. Bureau of Mines, N.T.I.S. U. S. Department of Commerce.
- Wu, H. and Pollard, D. D. 1995. An experimental study of relation between joint spacing and layer thickness. *J. Struc. Geol.* 6: 887-905.
- Yeung, M. R. 1991. *Application of Shi's Discontinuous Deformation Analysis to the study of rock behavior*. Ph. D. Thesis, Department of Civil Engineering, University of California, Berkley. 341p.
- Zhang, L. and Einstein, H. H. 1998. Estimating the mean trace length of rock discontinuities. *Rock. Mech. Rock. Eng.* 31(4): 217-235.
- Zienkiewicz, O. C., Best, B., Dullage, C., Stagg, K. 1970. Analysis of nonlinear problems in rock mechanics with particular reference to jointed rock systems. *Proceedings of the Second International. Congress on Rock Mechanics*, Belgrade, Yugoslavia.